Contact force and torque estimation for collaborative manipulators based on an adaptive Kalman filter with variable time period

by

Feng Cao

A thesis submitted in partial fulfilment for the

degree of Doctor of Philosophy

College of Engineering

Department of Mechanical Engineering

University of Canterbury

Christchurch, New Zealand

November 2021

ABSTRACT

Contact force and torque sensing approaches enable manipulators to cooperate with humans and to interact appropriately with unexpected collisions. In this thesis, various moving averages are investigated and Weighted Moving Averages and Hull Moving Average are employed to generate a mode-switching moving average to support force sensing. The proposed moving averages with variable time period were used to reduce the effects of measured motor current noise and thus provide improved confidence in joint output torque estimation. The time period of the filter adapts continuously to achieve an optimal trade-off between response time and precision of estimation in real-time. An adaptive Kalman filter that consists of the proposed moving averages and the conventional Kalman filter is proposed. Calibration routines for the adaptive Kalman filter interpret the measured motor current noise and errors in the speed data from the individual joints into. The combination of the proposed adaptive Kalman filter with variable time period and its calibration method facilitates force and torque estimation without direct measurement via force/torque sensors.

Contact force/torque sensing and response time assessments from the proposed approach are performed on both the single Universal Robot 5 manipulator and the collaborative UR5 arrangement (dual-arm robot) with differing unexpected end effector loads. The combined force and torque sensing method leads to a reduction of the estimation errors and response time in comparison with the pioneering method (55.2% and 20.8 %, respectively), and the positive performance of the proposed approach is further improved as the payload rises. The proposed method can potentially be applied to any robotic manipulators as long as the motor information (current, joint position, and joint velocities) are available. Consequently the cost of implementation will be significantly lower than methods that require load cells.

ACKNOWLEDGEMENTS

I would like to express my great attitude to the people who have helped me to accomplish this endeavour, in so many different ways.

Greatest attitude to my parents and my partner, who selflessly supported me to chase my dream in New Zealand across four years, with their hope, patience, and continuous encouragement. Although it seemed uncertain and difficult once, their love was always accompanying me.

Special thanks and admiration to my supervisor Assoc. Prof. Paul Docherty, who has provided the most dedicated guidance for me with his competence, work ethic, and experience. I could always feel his sense of responsibility, confidence, and kindness whenever we were working together. He has offered more help than what should be expected from a supervisor.

Many thanks to Prof. XiaoQi Chen, who has offered me this opportunity to study in University of Canterbury and introduced me to this research. His professional guidance and financial support facilitate accomplishment of this work and his great foresight has offered me a huge advantage in my career.

Many thanks also to all the friends and staff in UC, who have helped me or had fun with me. To Rodney Elliott, the technical officer of Mechatronics Engineering, he assisted me to perform all the physical experiments on the UR5 manipulators. To Prof. Dan Zhao, who shared his valuable experience in career development and that inspired me greatly. To Dr. Hae Güey, who introduced me into control area in my first year of PhD candidate, and we had so much fun by fishing and hunting. To Dr. Tao Cai, who is the most professional researcher at publishing papers around me, he helped me a lot to finish the response letter of my first journal paper. To Dr. Ming Bai, Dr. Khalid Salah, and Dr. Hammad Mohsin, they were like my big brothers, always had a good talk with me. To Dr. Cong Zhou, who encouraged me to pursue a higher goal in my last year of PhD candidate. At last, to my friends: Dr. Chunming Jiang, Dr. Honey Gupta, and Jewel Zhu, I treasure the fun with you. Thanks also to the researchers outside UC but helped me ever: Prof. Yanzheng Zhao and Dr. Jihao Liu in Shanghai Jiao Tong University.

PUBLICATIONS

This thesis is an original work by Feng Cao. It includes material reported in the following publications:

Cao F, Docherty P D, Ni S, et al. Contact force and torque sensing for serial manipulator based on an adaptive Kalman filter with variable time period. Robotics and Computer-Integrated Manufacturing, 2021, 72: 102210. [Online]. Available: https://www.sciencedirect.com/science/article/pii/S0736584521000934 (Ranked 3rd/29 in robotics and 3rd /378 in mathematics)

Cao, F., Docherty, P.D. & Chen, X. Contact force estimation for serial manipulator based on weighted moving average with variable span and standard Kalman filter with automatic tuning. Int J Adv Manuf Technol (2021). [Online].

Available: https://link.springer.com/article/10.1007/s00170-021-08036-9 (Ranked 21st/50 in engineering-manufacturing and 92nd/596 in mechanical engineering)

F. Cao, Y. Li, G. Zhang, J. Wang, X. Chen and Y. Zhao, "Novel humanoid dual-arm grinding robot," *2016 12th* IEEE/ASME International Conference on Mechatronic and Embedded Systems and Applications (MESA), 2016, pp. 1-6, doi: 10.1109/MESA.2016.7587185.

Available: https://ieeexplore.ieee.org/abstract/document/7587185

Deputy Vice-Chancellor's Office
Postgraduate Office

UNIVERSITY OF CANTERBURY
Te Whare Wānanga o Waitaha
CHRISTCHURCH NEW ZEALAND

Co-Authorship Form

This form is to accompany the submission of any thesis that contains research reported in co-authored work that has been published, accepted for publication, or submitted for publication. A copy of this form should be included for each co-authored work that is included in the thesis. Completed forms should be included at the front (after the thesis abstract) of each copy of the thesis submitted for examination and library deposit.

Please indicate the chapter/section/pages of this thesis that are extracted from co-authored work and provide details of the publication or submission from the extract comes:

Ch: 4,5
Cao, F., Docherty, P.D. & Chen, X. Contact force estimation for serial manipulator based on weighted moving average with variable span and standard Kalman filter with automatic tuning. Int J Adv Manuf Technol (2021). [Online].
Available: https://link.springer.com/article/10.1007/s00170-021-08036-9 (Ranked 21st/50 in engineering-manufacturing and 92nd/596 in mechanical engineering)

Ch: 4,6
Cao F, Docherty P D, Ni S, et al. Contact force and torque sensing for serial manipulator based on an adaptive Kalman filter with variable time period. Robotics and Computer-Integrated Manufacturing, 2021, 72: 102210. [Online].
Available: https://www.sciencedirect.com/science/article/pii/S0736584521000934 (Ranked 3rd/29 in robotics and 3rd /378 in mathematics)

Please detail the nature and extent (%) of contribution by the candidate:
In both cases, 95%

The candidate undertook the conception, modelling, experiment, analysis and drafting. The senior supervisor provided statistical and editorial advice. However, the statistical analysis was undertaken by the candidate.

Certification by Co-authors:
If there is more than one co-author then a single co-author can sign on behalf of all
The undersigned certifys that:

- The above statement correctly reflects the nature and extent of the PhD candidate's contribution to this co-authored work
- In cases where the candidate was the lead author of the co-authored work he or she wrote the text

Name: *Paul Docherty* Signature:  Date: *30 Nov 2021*

TABLE OF CONTENTS

NOMENCLATURE

o_i	coordinate frame of link i
$\boldsymbol{A}_i(\boldsymbol{q}_j)$	homogeneous transformation matrix of frame o_i with respect to frame o_0
$\boldsymbol{o}_i^j$	position of the coordinate frame o_i with respect to coordinate frame o_j
$\boldsymbol{T}_j^i$	the position and orientation of frame o_j with respect to frame o_i
$\boldsymbol{R}_i^j$	orientation of the coordinate frame o_i with respect to coordinate frame o_j
Trans_{z,d_i}	basic transformation of $\boldsymbol{A}_i(\boldsymbol{q}_j)$
$\mathrm{Rot}_{z,\theta_i}$	basic transformation of $\boldsymbol{A}_i(\boldsymbol{q}_j)$
$\mathrm{Trans}_{x,a_{i-1}}$	basic transformation of $\boldsymbol{A}_i(\boldsymbol{q}_j)$
$\mathrm{Rot}_{x,\alpha_{i-1}}$	basic transformation of $\boldsymbol{A}_i(\boldsymbol{q}_j)$
a_{i-1}	link length, deg
d_i	link offset, mm
X_i	X axis of frame o_i
Y_i	Y axis of frame o_i
Z_i	Z axis of frame o_i
l	distance of two manipulators, mm
$\mathbf{Z}_i^j$	Z axis of coordinate frame o_i expressed in frame o_j
$\boldsymbol{J}_i$	Jacobian of the i-th UR5
$\boldsymbol{J}_{w\_i}$	angular velocity part of the Jacobian
$\boldsymbol{J}_{v\_1}$	velocity part of the Jacobian
$\dot{\boldsymbol{o}}_6^0(\boldsymbol{q}_1)$	linear velocity of the frame o_i with respect to frame o_j
$\boldsymbol{J}_{\boldsymbol{v}\_\boldsymbol{j}_i}$	the first i columns of $\boldsymbol{J}_{v\_j}$
$\boldsymbol{J}_{\boldsymbol{\omega}\_\boldsymbol{j}_i}$	the first i columns of $\boldsymbol{J}_{\boldsymbol{\omega}\_j}$
q_j^i	joint position of the i-th joint of the j-th UR5, rad
$\dot{q}_j^i$	joint velocity of the i-th joint of the j-th UR5, rad/s
$\ddot{q}_j^i$	joint acceleration of the i-th joint of the j-th UR5, rad/s^2
$\boldsymbol{M}(\boldsymbol{q})$	inertia matrix of the dual-arm robot
$\boldsymbol{M}_i(\boldsymbol{q})$	inertia matrix of the i-th UR5
m_i	mass of the i-th link, kg
$\boldsymbol{q}_{j\_i}$	joint speed of the first i joints of the j-th UR5
$\boldsymbol{I}_i$	inertia tensor of the i-th link

c_{kj}	the k,j-th element of $\boldsymbol{C}(\boldsymbol{q},\dot{\boldsymbol{q}})$
c_{ijk}	Christoffel symbols of the first kind
m_{ki}	the k,j-th element of $\boldsymbol{M}_i(\boldsymbol{q}_i)$
$\boldsymbol{gra}$	vector giving the direction of gravity in the inertial frame
$\boldsymbol{g}_i(\boldsymbol{q}_i)$	gravity of the i-th UR5
$\boldsymbol{g}_i^j(\boldsymbol{q}_i)$	the j-th element of $\boldsymbol{g}_i(\boldsymbol{q}_i)$
$\boldsymbol{r}_{ci}$	coordinates of the centre of mass of link i
P_i	potential energy of the i-th UR5
$\boldsymbol{f}_i$	The external wrench exerted on the i-th UR5
$\boldsymbol{f}$	The external wrench exerted on the dual-arm robot
$\boldsymbol{f}_{\text{ext}}$	combined external wrench
$\boldsymbol{I}_i$	centroid of link i
$\boldsymbol{S}_1$	dynamic matrix of the external wrench on the i-th UR5
$\boldsymbol{e}_{f\_1}$	uncertainty of the external wrench on the i-th UR5
$\boldsymbol{e}_f$	uncertainty of the external wrench on the dual-arm robot
$\boldsymbol{e}_{p\_1}$	uncertainty of the systematic dynamics of the i-th UR5
$\boldsymbol{e}_p$	uncertainty of the systematic dynamics of the dual-arm robot
$\boldsymbol{q}_i$	joint position of the i-th UR5
$\boldsymbol{q}$	joint position of the dual-arm robot
$\dot{\boldsymbol{q}}_i$	speed of the i-th UR5
$\dot{\boldsymbol{q}}$	joint speed of dual-arm robot
$\ddot{\boldsymbol{q}}_i$	acceleration of the i-th UR5
$\ddot{\boldsymbol{q}}$	acceleration of the dual-arm robot
$\boldsymbol{C}_i(\boldsymbol{q}_i,\dot{\boldsymbol{q}}_i)$	The Coriolis and centrifugal matrix of the i-th UR5
$\boldsymbol{C}_1(\boldsymbol{q},\dot{\boldsymbol{q}})$	The Coriolis and centrifugal matrix of the dual-arm robot
$\boldsymbol{G}_i(\boldsymbol{q}_i)$	gravity of the i-th UR5
$\boldsymbol{G}(\boldsymbol{q})$	gravity of the dual-arm robot
$\boldsymbol{p}_i$	generalized momentum of the i-th UR5
$\boldsymbol{p}$	generalized momentum of the dual-arm robot
$\boldsymbol{P}_i$	covariance matrix of the i-th step
$\boldsymbol{x}_i$	state vector of the i-th UR5
$\boldsymbol{x}$	state vector of the dual-arm robot

$\boldsymbol{A}_i$	state matrix of the i-th UR5
$\boldsymbol{A}$	state matrix of the dual-arm robot
$\boldsymbol{B}_i$	input matrix of the i-th UR5
$\boldsymbol{B}$	input matrix of the dual-arm robot
$\boldsymbol{C}_i$	output matrix of the i-th UR5
$\boldsymbol{C}$	output matrix of the dual-arm robot
$\boldsymbol{w}_i$	covariance matrix of the predicted state noise of the i-th UR5
$\boldsymbol{w}$	covariance matrix of the predicted state noise of the dual-arm robot
t_s	time gap between two samples, s
$\boldsymbol{Z}_i$	measurement noise of the i-th UR5
$\boldsymbol{Z}$	measurement noise of the dual-arm robot
$\boldsymbol{k}_i$	motor torque constant of the i-th UR5
$\boldsymbol{r}_i$	gearbox ratio of the i-th UR5
D_{1_elb}	composite term of the elbow joint motor of the first UR5, Nm/A
k_{1_elb}	motor torque constant of the elbow joint motor of the first UR5, Nm/A
r_{1_elb}	gearbox ratio of the elbow joint motor of the first UR5
i_{gra}	current related to the joint torque resulting from the gravity, A
i_{fri}	current corresponding to the joint friction, A
i_{dri}^{+}	motor currents with the joint moving clockwise, A
i_{dri}^{-}	motor currents with the joint moving counterclockwise, A
$\boldsymbol{f}_{C\_i}$	Column friction of the i-th UR5, Nm
$f_{C\_i}^{j}$	Column friction of the j-th joint of the i-th UR5, Nm
$\boldsymbol{f}_{\dot{q}\_i}$	viscous friction coefficient of the i-th UR5
$f_{\dot{q}\_i}^{j}$	viscous friction coefficient of the j-th joint of the i-th UR5, Nms/rad
$\widehat{\dot{\boldsymbol{q}}}$	measured mean speed of the dual-arm robot
$\overline{\dot{\boldsymbol{q}}}$	target speed of the dual-arm robot
$\dot{\boldsymbol{q}}_{\mathrm{thr}}^{i}$	threshold velocity for the i-th joint of the manipulator
d	time step
t	number of the samples
i_d	current sample at step time d, A
i_d^{opt}	filtered current at step time d, A
$W(d,t)$	Weighted Moving Average

$H(d,t)$	Hull Moving Average

Greek Symbols

θ_i	link angle, rad
α_{i-1}	joint twist, rad
$\boldsymbol{\omega}_i^j$	angular velocity of the i-th link rotates about Z_i in o_j
$\boldsymbol{\tau}_{\mathrm{fri}}$	joint friction of the dual-arm robot
$\boldsymbol{\tau}_{\mathrm{fri\_}i}$	Joint friction of the i-th UR5
$\boldsymbol{\tau}_{\mathrm{dri}}$	joint driving torques of the dual-arm robot
$\boldsymbol{\tau}_{\mathrm{dri\_}i}$	joint driving torques of the i-th UR5
$\boldsymbol{\tau}_{\mathrm{ext}}$	joint torques caused by the external wrench exerted on the dual-arm robot
$\boldsymbol{\tau}_{\boldsymbol{ext\_1}}$	joint torques caused by the external wrench exerted on the i-th UR5
$\boldsymbol{\sigma}_{f\_1}^2$	diagonal matrix reflecting uncertainty of the external wrench on the i-th UR5
$\boldsymbol{\sigma}_f^2$	diagonal matrix reflecting uncertainty of the external wrench on the dual-arm robot
$\boldsymbol{\tau}_{\mathrm{int\_}i}$	joint torques on the i-th UR5 resulting from the internal force between the two arms
$\boldsymbol{\tau}_{\mathrm{int}}$	joint torques resulting from the internal force between the two arms
$\boldsymbol{\sigma}_{\mathrm{mea\_}i}^2$	diagonal matrix reflecting the measurement noise of the i-th UR5
$\boldsymbol{\sigma}_{\mathrm{mea}}^2$	diagonal matrix reflecting the measurement noise of the dual-arm robot
$\boldsymbol{\sigma}_{\mathrm{pro\_}i}^2$	covariance matrix of the predicted state noise of the i-th UR5
$\boldsymbol{\sigma}_{\mathrm{pro}}^2$	covariance matrix of the predicted state noise of the dual-arm robot
$\boldsymbol{\sigma}_{\mathrm{Dyn\_}i}^2$	diagonal matrix reflecting uncertainty of the dynamics of the i-th UR5
$\boldsymbol{\sigma}_{\mathrm{Dyn}}^2$	diagonal matrix reflecting uncertainty of the dynamics of the dual-arm robot
$\widehat{\boldsymbol{\tau}_{\mathrm{dri\_}i}}$	calculated joint driving torques of the i-th UR5
$\overline{\boldsymbol{\tau}_{\mathrm{dri\_}i}}$	ideal joint output torques of the i-th UR5
$\delta_{s\_i}^j$	empirical parameter of the j-th joint of the i-th UR5
$\boldsymbol{\sigma}_{\dot{q}}^{\mathrm{elbow}}$	standard deviation of the elbow joint
δ	parameter used to decide whether the span varies or not, A

ABBREVIATIONS

AKF	Adaptive Kalman Filter
CFTE	Contact Force/Torque Estimation
CKF	Conventional Kalman Filter
DH	Denavit-Hartenberg
EMA	Exponential Moving Average
HMA	Hull Moving Average
KF	Kalman Filter
MSMA	Mode-switching Moving Average
RMSE	Root-mean-squared Errors
SD	Standard Deviation
SKF	Standard Kalman Filter
SKFNW	Weighted Moving Average with No Variable Span
SKFW	Weighted Moving Average with Variable Span
SMA	Simple Moving Average
TCP	Tool Centre Position
UR5	Universal Robot 5
WMA	Weighted Moving Average
WMAWFT	Weighted Moving Average with Fixed Time Period
WMAWVT	Weighted Moving Average with Variable Time Period

LIST OF TABLES

LIST OF FIGURES

1. INTRODUCTION

With the development of artificial intelligence, advanced manufacturing, and new sensor technology, research expanding the capabilities of robots is becoming more prevalent. The robotic ability to integrate with human resources will be important for ongoing improvement in efficiency, and commercial competition. In industry, robots of human size are expected to replace human workers without major redesigns of the workplace [1]. In high-risk environments, such as nuclear, deep-sea, or aerospace, robots are expected to undertake welding, assembly, rescue tasks and similar. (Fig. 1)

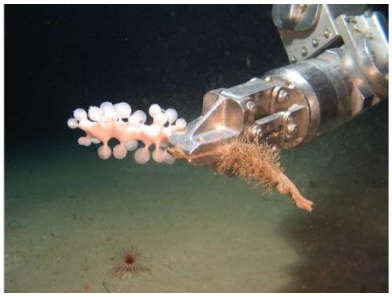

(a) Collecting marine samples [2]

(b) Welding [3]

(c) Assembling [4]

(d) Palletizing [5]

Fig. 1.1. Robotic manipulators.

Recently, the focus of some robotic research has been shifting from single-arm manipulators to cooperative dual-arm manipulators [6]-[10]. The very early dual-arm system, originally used for handling radioactive goods, was developed in the 1940's [11]. The system worked in pairs and the operator controlled one robot with each hand. In recent years, the challenge inherent in the dual-arm manipulation has caught researchers' attention, which in return led to various dual-arm robots. The most common examples are SDA 10 [12], PR2 [13], Baxter [14], and Yumi (Fig. 1.2).

(a) SDA 10

(b) PR2

(c) Baxter

(d) Yumi

Fig. 1.2. Dual-arm robots.

Compared to their single-arm counterpart, the dual-arm robots demonstrate the following advantages:

a. The traditional single-arm robot failed in grinding precision because of its poor rigidity [15], usually lower than 1N/μm. In contrast, the dual-arm robot can enhance the rigidity dramatically with two arms holding the workpiece in a 'loop' structure.

b. Humans typically perform complex or precise tasks with two arms. A robot with two arms facilitates the transfer of human grinding skills and knowledge to the robot [16]. For example, the gear clearance and friction between the joints lead to the low kinematic accuracy of the robot, and its repeatability of positioning is usually 0.02mm-0.08mm [17]. Although the repeated positioning precision of the robot is better than that of the craftsmen, trained humans can perform machining tasks with higher precision than robots. It is mainly because humans are able to integrate the information of position and the feedback of force, which will offset the position error. In other words, a dual-arm robot can potentially work in a dexterous human-like manner if it has sufficient positional feedback.

c. Dual-arm robots are expected to work in environments originally intended for humans. In other words, the dual-arm robots carry the potential of replacing human workers without redesigning the workspace.

d. Dual-arm systems occupy less space and have lower cost, as compared to two single arm units that provide equivalent tasks [18].

1.1. Background on external wrench estimation for manipulators

Robotic manipulators play an important role in various manufacturing tasks. However, robotic control strategies can fail to take environmental and operator interaction into account. Thus, the robots can cause hazardous or unexpected situations. Therefore, force-control techniques are widely applied in cooperating manipulators [19]-[21], assembly [22], haptics [23], grinding [24]-[31], physical human-robot interaction [31]-[33], exoskeleton robots [34], [35] , and collision detection [36].

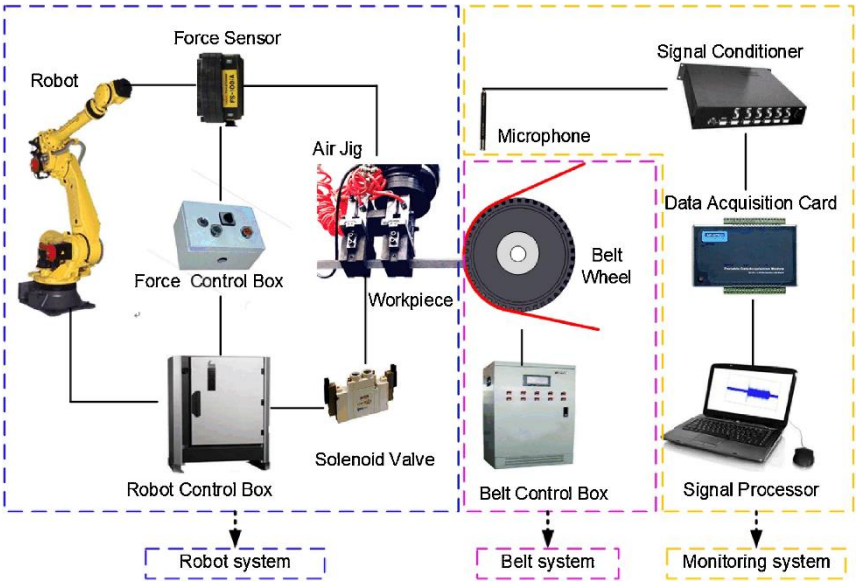

Fig. 1.3. A grinding system based on the manipulator with force sensor [24].

Fig. 1.4. Exoskeleton robots [37].

The dual-arm robotic systems possess pronounced advantages in employing human bimanual working skills compared with their single-arm counterparts [38]. Dual-arm configuration can facilitate more complicated and challenging tasks,

such as farming [39], underwater operations [40], and surgery [41]. In order to achieve successful cooperation between the two interactive rigid manipulators, force-based coordinated control must be implemented in the robotic system to achieve successful motion performance. Furthermore, dual-arm manufacturing missions, like assembly [42] and grinding [43], require contact force between the end effectors and the environment to be regulated within a certain range.

Fig. 1.5. A dual-arm polishing robot developed by the author [44].

Fig. 1.6. Collaborative robots from JAKA making coffee [45].

Furthermore, manipulators based on force control play an important role in on-orbit missions, such as spacecraft capture [46], [47], non-cooperative target grasping[48], [49], assembly and repair [50], [51], multi-arm cooperation[52], and experimental research[53]-[55]. With the detection techniques of the external wrench, the force-control manipulators can regulate the contact force and torque within a certain range and thus perform more challenging tasks compared to their

position-controlled counterparts. However, the common methods to measure the contact information for the ground-based robotic manipulators, which utilize the 6-axis force/torque sensors or torque sensors that are mounted between the link side and the motor side of the robot, may result in extra cost or poor performance if employed in on-orbit missions. For example, the severe environment such as extreme cold and vacuum can affect the performance of these exposed sensors. Furthermore, the sensors are prone to damage since the end effector of the manipulator often performs rigid-contact missions with the environment. Finally, the difficulty in transporting and maintaining these sensors in outer space makes implementation significantly more expensive than on the earth. Consequently, research of sensorless external wrench estimation has been conducted and various contact force and torque estimation methods have been proposed.

Fig. 1.7. The international space station's Canadarm2 [56].

1.2. Motivation of sensorless contact force/torque estimation

The force-control techniques require information regarding the force exerted and torque exerted on the robot in order to regulate the robotic motion within appropriate bounds. Historically, the most common method to measure the contact force and torque is to utilize 6-axis force/torque sensors which are mounted on the end of the robotic manipulator (as shown in Fig. 1.8), or torque sensors that are mounted between the link side and the motor side of the robot (as shown in Fig. 1.9). More recently, various force/torque sensors for manipulators were developed [57]-[61]. Techniques like deep-learning were employed to calibrate these sensors [62]. With these sensitive sensors, hybrid force/position control [63] and impedance control [64] are well developed and have been introduced into various areas. However, the extension of these sensors is limited due to their cost. Furthermore, the sensors may become worn or damaged as the end effector usually

conducts rigid contact with the environment [65]. Finally, both the varying temperature and humidity, and the narrow bandwidth caused by the sensors inevitable susceptibility to measurement noise affect the performance of these sensors, and resultant motion control.

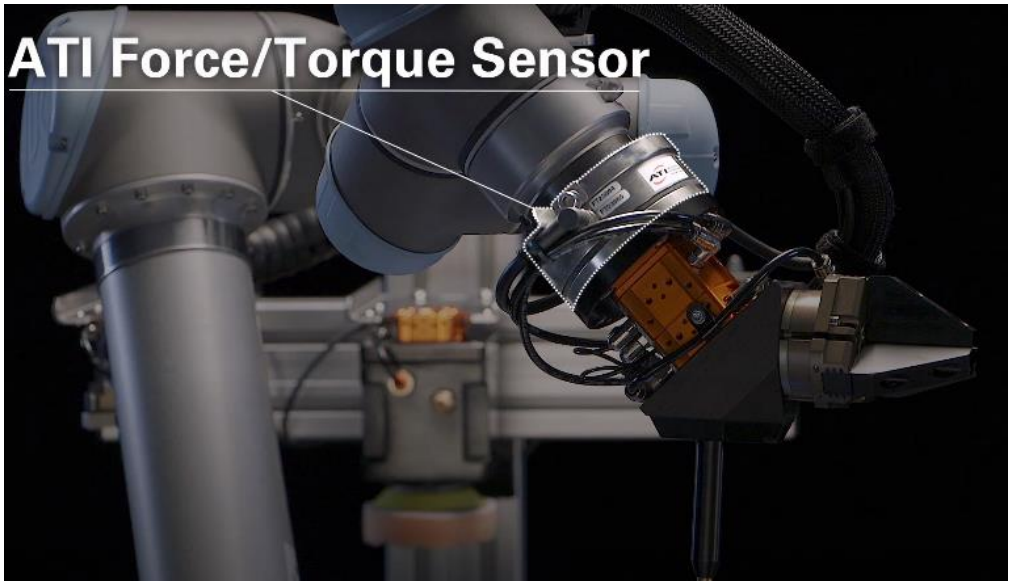

Fig. 1.8. ATI force/torque sensor mounted on the end of UR5 [66].

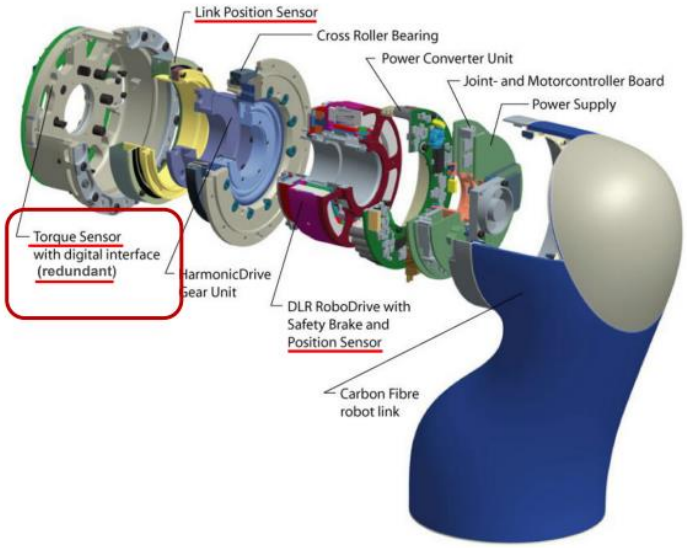

Fig. 1.9. Torque sensor mounted between the link side and motor side [67].

To enable sensorless force/torque contact estimation, various observers for estimating an external wrench have been proposed. An early disturbance observer developed by Kiyoshi et al. [68] has been widely used as a basis for force/torque sensing research and development. When the manipulator unexpectedly interacts with the environment, sensorless force/torque contact estimation methods detect the external wrench as a disturbance by comparing the actual motor output to the motor output estimated by a nominal model. Further disturbance observer force/torque sensing research is presented

in [69], [70]. More recently, Chen et al. improved the disturbance observer and applied it to nonlinear robotic systems [71], [72]. The nonlinear disturbance observer has also been extensively used [73], [74]. In order to utilize the disturbance observer, a real-time inverse inertia matrix of the robot must be continuously calculated leading to notable computational burden.

Due to the development of compliant elements in robotics, various flexible robotic systems, such as rehabilitation robots, have been proposed and thus the safety and back-drivability of physical Human-Robot Interaction systems have been improved. In particular, the exerted force/torque on the manipulator can be estimated with kinematic measurement. In these methods, sensorless torque estimation of the stiff and sensitive joint is implemented by understanding the structural elasticity of the robotic joints with harmonic drive transmission in [75]-[77] and only motor-side and link-side position measurements are required. However, this method is difficult to conduct since a prior model of the harmonic drive is required and it is very complicated to develop and validate. Furthermore, compliant elements ultimately have high implementation costs. Thus, there is a preference for direct force measurement. Other sensorless external wrench sensing approaches, such as time delay estimation and virtual springs, can be found in [78] and [22], respectively.

1.3. Thesis objectives and research question

In order to realize sensorless external wrench estimation, a dynamic model of the robotic system with low computational burden must be built. More specifically, large repetitive inversion calculation of dynamic equations is to be avoided. Furthermore, designing an adaptive Kalman filter that employs the information of dynamic uncertainty is required. Moreover, calibration of the adaptive Kalman filter using the potential knowledge of the systematic dynamics is conducted. Finally, the proposed adaptive Kalman filter and the calibrating methods needs to be validated on the both the single-arm and dual-arm systems.

1.4. Organization of thesis

The thesis is structured as follows:

Chapter 1 presents background of external wrench estimation for manipulator, motivation and objective of the sensorless contact force/torque estimation.

Chapter 2 presents kinematic models of robotic systems. Relevant Jacobians of the systems are calculated. With the kinematic models and Jacobians, the dynamic models of both the single-arm and the dual-arm systems are built based on the generalized momentum principals. The system dynamics is then discretized.

Chapter 3 gives details of how to identify the system dynamics without extra force/torque sensors. First, the joint driving torques are modelled. Secondly the joint frictions are determined. Thirdly, the covariance matrix of the predicted state noise is calculated based on the joint driving torques. At last, the covariance matrix of the measurement noise is determined using the joint velocity errors.

Chapter 4 proposes two kinds of pre-filters, the Weighted Moving Average (WMA) with variable time period and the Mode-switching Moving Average (MSMA) with time period. With these pre-filters, two different adaptive Kalman filters are designed. Calibration of the Adaptive Kalman filter (AKF), and its pre-filters are presented.

Chapter 5 presents CFTE experiments with an AKF based on the WMA with variable time period. The experimental tests are conducted on the single-arm robot and the results are also shown in this chapter. Effects of the proposed AKF are discussed.

Chapter 6 presents experiments of validating an adaptive Kalman filters based on the proposed MSMA with variable span. The proposed CFTE method is tested on the single-arm robot. The results are also shown in this chapter and effects of the proposed AKF are discussed.

Chapter 7 presents experiments of validating the adaptive Kalman filters based on the MSMA with variable span on the dual-arm robot. The CFTE results are shown and effects of the proposed AKF are discussed.

Chapter 8 presents experiments of validating two adaptive Kalman filters on the dual-arm robot. The results are also shown in this chapter and effects of the proposed AKF are discussed.

Chapter 9 concludes and reiterates the novel contributions of this thesis.

Chapter 10 considers potential avenues for future work.

2. KINEMATIC AND DYNAMIC MODELS OF THE ROBOTIC SYSTEMS

In this thesis, the Universal Robot 5 (as shown in Fig. 2.1) is employed to validate the proposed contact force and torque estimation (CFTE) method. In order to conduct experimental tests on both the single-arm and the dual-arm robotic systems, kinematics of both systems are analysed and kinematic models are built based on the Denavit-Hartenberg convention in section 2.2. With the kinematic models, Jacobians of the robots are deducted in section 2.3. Based on the manipulator Kinematics and Jacobians, dynamics of the robotic systems are expressed by the Euler-Lagrange equations in section 2.4 and then modified into the format of the generalized momentum. The generalized-momentum-based model is discretized as state space equations in section 2.6, which can be applied to the conventional Kalman filter.

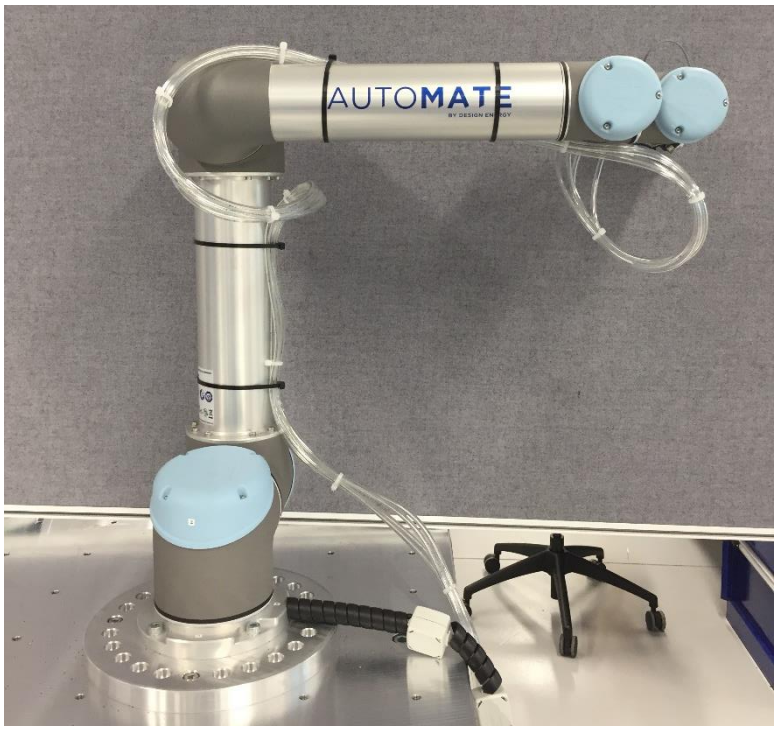

Fig. 2.1. Universal Robot 5

2.1. Background and motivation

Generally, the Euler-Lagrange equations are employed to model a serial manipulator [1], [80]. However, inversion of the dynamics must be calculated in real time which causes extra calculation burden. Consequently, De Luca et al. [81] - [83] present a novel method, in which the robot dynamics are expressed in the format of the generalized momentum. This approach is originally proposed for collision detection and hybrid force/position control, but recent researchers have exploited its further application to lead-through programming [84]. With the motor current and Moore-Penrose generalized inverse matrix, the exerted force/torque on the end of the manipulator is estimated and applied to a combined control mode by Yuan et al.[85]. Similarly, Yen et al. [86] monitor the motor current and transform it to joint torques, which is then used

to estimate the external wrench. Another collision detection method that depends on virtual power indices is proposed in [87]. At a fundamental level, [85] - [89] all have characteristics of De Luca's generalized momentum dynamic model due to the model's independence from joint acceleration measurements and inversion of the manipulator inertia matrix. However, the research arising from De Luca's model is limited to collision detection or low-precision force/torque control since the noise in the measured current can trigger false positive collision recognition or insufficient force estimation precision.

2.2. Kinematics of the robotic system

Typically, industrial manipulators consist of adjacent links connected by joints. These connections include rotate, prismatic, ball, and spherical joints. In this research, only rotation joints are considered as the UR5 has six rotating joints. Each joint has one degree of freedom and can rotate like a hinge. With the above assumption, rotation of each joint can be represented by a single angle. Before building dynamic models of the robot, system kinematics must be explored.

For the serial manipulator, every connection between two links has one rotational joint. Thus, the UR5 with 6 joints has 7 links (Fig. *2.2*). The joints are numbered from 1 to 6. The links are numbered from 0 to 6, from the base being 0 to the end effector 6. Under this assumption, link $i-1$ and link i are connected by the joint i. Joint i is technically considered rigidly connected to link i. Therefore, link i moves as joint i rotates. In this model, link 0 is fixed to a rigid platform in the laboratory and represented by the manipulator base (Fig. 2.2). q_i describes the angle of rotation of joint i.

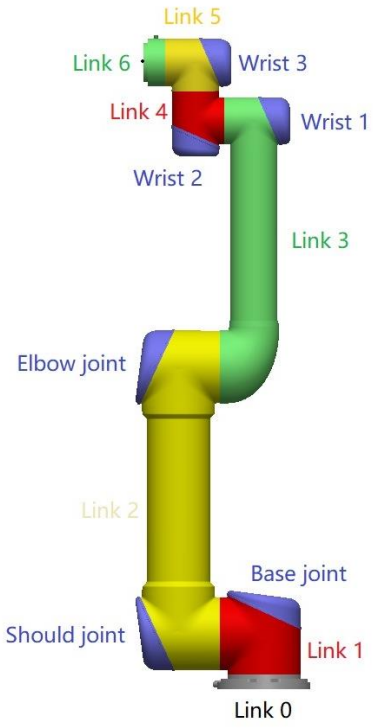

Fig. 2.2. Sketch of the UR5

To explore the kinematic relationship between each link, link i is represented by a coordinate frame o_i, which is fixed to link i. It is worth noting the coordinates of each part of link i stay constant during motion of the manipulator since it is expressed in the coordinated frame o_i. The base coordinate frame is express by o_0 and attached to the manipulator base. To describe the transformation of position and orientation of frame o_i with respect to frame o_{i-1}, the homogeneous transformation matrix $\boldsymbol{A}_i$ is introduced. The characteristics of the UR5 are all constant except for joint angle, thus $\boldsymbol{A}_i$ is a function of $\boldsymbol{q}_i$ and expressed as $\boldsymbol{A}_i(\boldsymbol{q}_i)$ and obtained by:

$$\boldsymbol{A}_i = \begin{bmatrix} \boldsymbol{R}_i^{i-1} & \boldsymbol{o}_i^{i-1} \\ 0 & 1 \end{bmatrix} \tag{2-1}$$

The position and orientation of the coordinate frame o_i with respect to coordinate frame o_{i-1} are expressed by $\boldsymbol{o}_i^{i-1} \in \boldsymbol{\mathcal{R}}^{3\times1}$ and $\boldsymbol{R}_i^{i-1} \in \boldsymbol{\mathcal{R}}^{3\times3}$ respectively. With this definition, the position and orientation of frame o_j with respect to frame o_i is presented by $\boldsymbol{T}_j^i$ and calculated by:

$$\boldsymbol{T}_j^i = \boldsymbol{A}_{i+1}\boldsymbol{A}_{i+2}\cdots\boldsymbol{A}_{j-1}\boldsymbol{A}_j \tag{2-2}$$

2.2.1. Kinematics of the single-arm system

In order to identify $\boldsymbol{R}_i^{i-1}$ and o_i^{i-1}, the Denavit-Hartenberg (DH) convention is employed to describe kinematics of the UR5 manipulator. Since the dynamic models are described in the format of generalized momentum, inversion of the

kinematics is not required. Hence, only the forward kinematics are discussed. The purpose of researching the forward kinematics is to find the relationship between individual manipulator joints and the orientation and position of the tool centre point. To be more specific, the orientation and position of the tool centre point are calculated by considering all joint variables. In this convention, the homogeneous transformation $\boldsymbol{A}_i$ is calculated by 4 basic transformations:

$$\boldsymbol{A}_i = \mathrm{Trans}_{z,d_i} \cdot \mathrm{Rot}_{z,\theta_i} \cdot \mathrm{Trans}_{x,a_{i-1}} \cdot \mathrm{Rot}_{x,\alpha_{i-1}} \tag{2-3}$$

The four transformations are obtained by:

$$\mathrm{Trans}_{z,d_i} = \begin{bmatrix} 1 & 0 & 0 & 0 \\ 0 & 1 & 0 & 0 \\ 0 & 0 & 1 & d_i \\ 0 & 0 & 0 & 1 \end{bmatrix} \tag{2-4}$$

$$\mathrm{Rot}_{z,\theta_i} = \begin{bmatrix} \cos\theta_i & -\sin\theta_i & 0 & 0 \\ \sin\theta_i & \cos\theta_i & 0 & 0 \\ 0 & 0 & 1 & 0 \\ 0 & 0 & 0 & 1 \end{bmatrix} \tag{2-5}$$

$$\mathrm{Trans}_{x,a_{i-1}} = \begin{bmatrix} 1 & 0 & 0 & a_{i-1} \\ 0 & 1 & 0 & 0 \\ 0 & 0 & 1 & 0 \\ 0 & 0 & 0 & 1 \end{bmatrix} \tag{2-6}$$

$$\mathrm{Rot}_{z,\alpha_{i-1}} = \begin{bmatrix} 1 & 0 & 0 & 0 \\ 0 & \cos\alpha_{i-1} & -\sin\alpha_{i-1} & 0 \\ 0 & \sin\alpha_{i-1} & \cos\alpha_{i-1} & 0 \\ 0 & 0 & 0 & 1 \end{bmatrix} \tag{2-7}$$

where four quantities of θ_i, a_{i-1}, d_i, α_{i-1} represent the parameters related to the link *i* and joint *i* and represent joint angle, link length, link offset, and link twist, respectively. In this research, Z_i is assigned along the axis of joint i. For the UR5, the axes of adjacent joints are perpendicular or parallel to each other. Under the former condition, there must be a unique line segment perpendicular to both Z_i and Z_{i+1}, which connects both axes and has the minimum length. X_{i+1} is defined along this line and the point where X_{i+1} intersects Z_{i+1} defines o_{i+1}. For the UR5, Z_i and Z_{i+1} are all coplanar and the positive direction of X_i is from Z_i to Z_{i+1}. With Z_{i+1} and X_{i+1}, Y_{i+1} is chosen according to the right-handed rule and the frame $\boldsymbol{o}_{i+1}$ is then determined. Under the latter condition, there are innumerable normals between Z_i and Z_{i+1}. In this case, any point along Z_{i+1} can be regarded as o_{i+1} as long as it can simplify the transformation equations. X_{i+1} is then determined along the line from o_{i+1} to Z_i or, it can be set as the opposite of this direction. Similarly, Y_{i+1} is determined in this right-handed frame. For the sixth frame, o_6 is placed in the center of the surface of link 6 (as shown in Fig. 2.2). X_6 is parallel to X_5. Consequently, the DH coordinate frame assignment for the UR5 manipulator is shown in Fig. 2.3(b). The corresponding physical UR5 with individual joints at position 0 is displayed in Fig. 2.3(a).

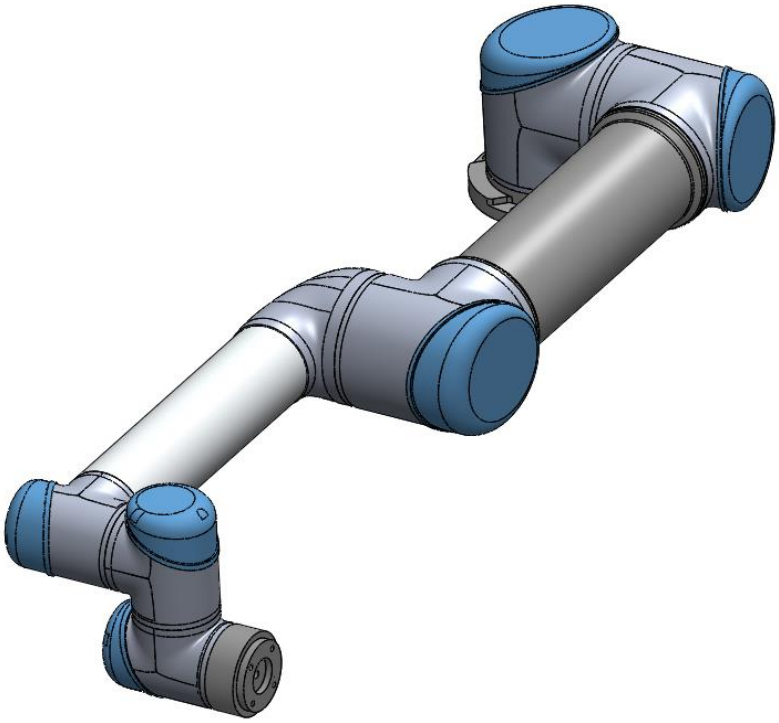

(a) UR5 manipulator.

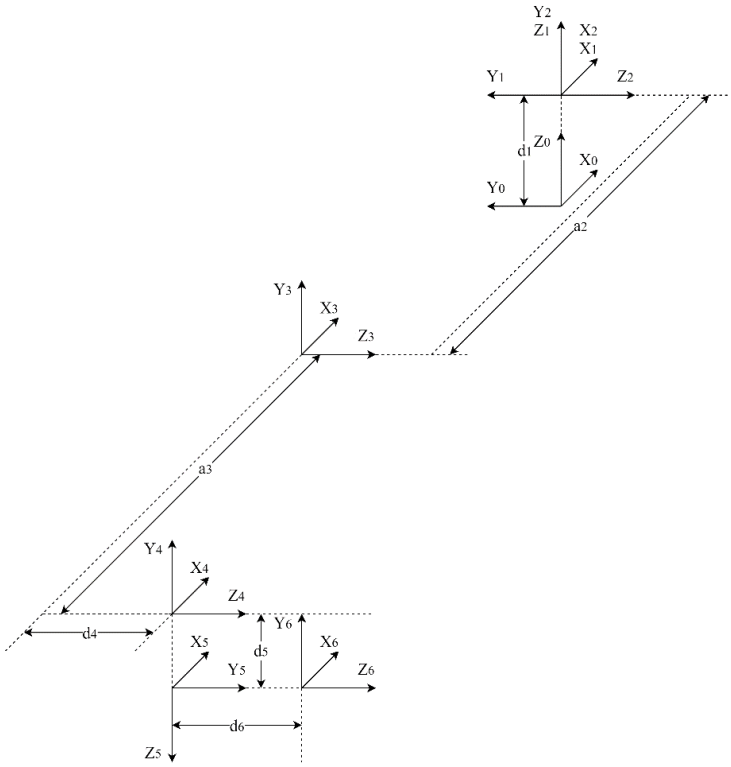

(b) DH coordinate frame assignment for the UR5 manipulator.

Fig. 2.3. The UR5 manipulator and the related DH coordinate frame.

With the set-up coordinate frames, DH transformation from frame o_{i-1} to frame o_i is conducted and the four DH parameters of each transformation can be obtained by the following 4 steps:

1. The frame o_{i-1} rotates about axis X_{i-1} for the angle of α_{i-1} and thus Z_{i-1} is parallel to Z_i.
2. The frame o_{i-1} moves along X_{i-1} for the distance of a_{i-1} and thus Z_{i-1} and Z_i are collinear.
3. The frame o_{i-1} rotates about axis Z_i for the angle of θ_i and thus X_{i-1} is parallel to X_i.
4. The frame o_{i-1} moves along Z_i for the distance of d_i and thus X_{i-1} and X_i are collinear.

The above four steps correspond to the four basic transformations in Eq. 2-3 successively. Therefore, the physical and mathematic transformations from frame o_{i-1} to frame o_i are obtained and the related parameters in individual DH transformations are summarized in Table 2-1.

Table 2-1 The DH parameters of UR5

Parameters / Joint	θ_i [rad]	a_{i-1} [m]	d_i [m]	α_{i-1} [rad]
1	0	0	0.089159	0
2	0	0	0	π/2
3	0	-0.425	0	0
4	0	-0.39225	0.10915	0
5	0	0	0.09465	π/2
6	0	0	0.0823	-π/2

Following Eq. 2-2 to Eq. 2-7, the position and orientation of frame o_6 with respect to frame o_0 is presented by $\boldsymbol{T}_6^0$ and calculated by:

$$\boldsymbol{T}_6^0 = \boldsymbol{A}_1\boldsymbol{A}_2\boldsymbol{A}_3\boldsymbol{A}_4\boldsymbol{A}_5\boldsymbol{A}_6 \qquad 2\text{-}8$$

2.2.2. Kinematics of the dual-arm system

In contrast to the single-arm model, internal force and torque between the two manipulators arises when dual-arm actions are performed. In order to test the proposed CFTE method on the dual-arm robot, with consideration of internal interaction, a kinematic model must first be defined. The first step is decoupling two robots according to Eq. 2-8, with $o_{02} = o_0 + [l \quad 0 \quad 0]^T$. Then, an extension spring is fixed to the end effectors of the two manipulators. The effects of this spring on the two arms are regarded as the internal force. Therefore, the position and orientation of the TCP of each manipulator with respect to the other one must be determined.

Similar to the single-arm model, the kinematic model of the dual-arm system are defined using the DH convention. One UR5 is deemed as the master and the other is regarded as the slave one (Fig. 2.4). DH coordinate frame assignment for the dual-arm system is displayed in Fig. 2.4. The base of the master manipulator is decided as the base frame and described as o_0. The six joints of the master manipulator are numbered from 1 to 6 and the counterpart joints of the slave one are numbered from 7 to 12. Each frame assignment for individual joints is determined according to the method mention in

section 2.2.1.

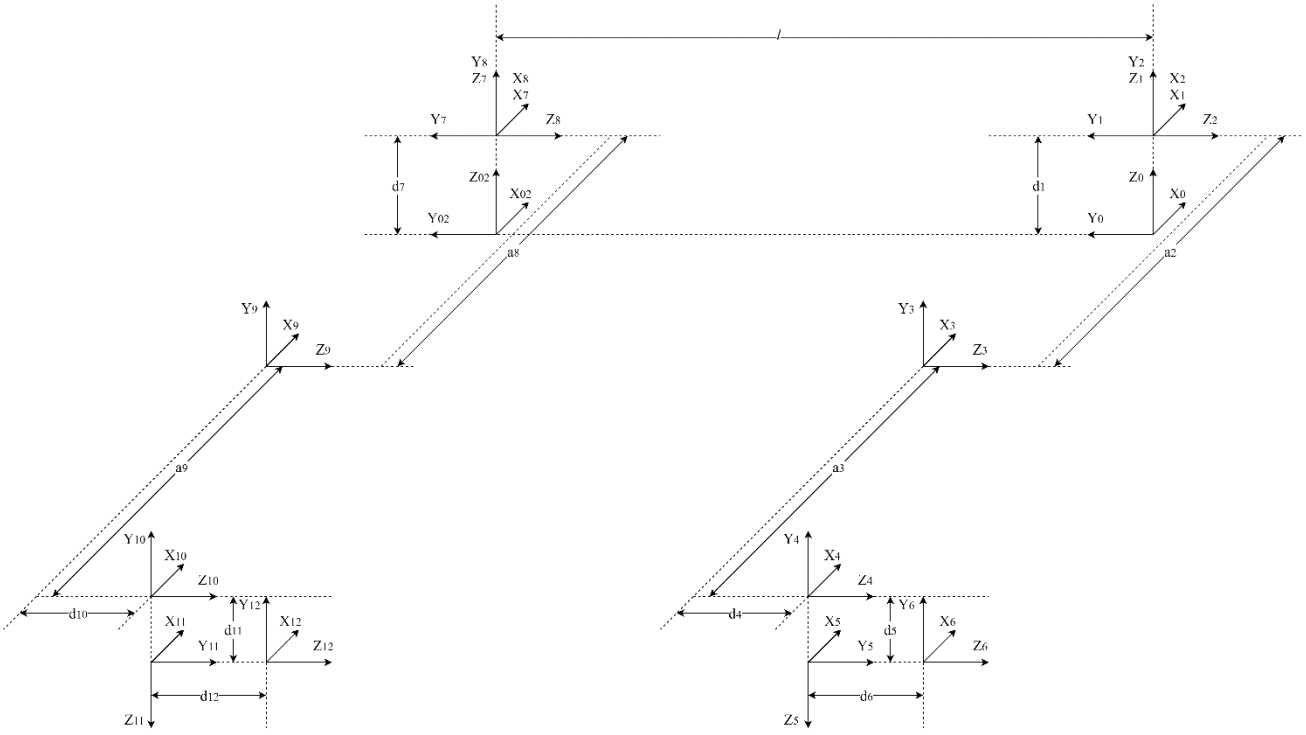

Fig. 2.4. DH coordinate frame assignment for the dual-arm system

The position and orientation of frame o_6 with respect to base frame o_0 is presented by $\boldsymbol{T}_6^0$ and calculated by:

$$\boldsymbol{T}_6^0 = \boldsymbol{A}_1\boldsymbol{A}_2\boldsymbol{A}_3\boldsymbol{A}_4\boldsymbol{A}_5\boldsymbol{A}_6 \tag{2-9}$$

The position and orientation of frame o_{12} with respect to base frame o_{02} is calculated by:

$$\boldsymbol{T}_{12}^{02} = \boldsymbol{A}_7\boldsymbol{A}_8\boldsymbol{A}_9\boldsymbol{A}_{10}\boldsymbol{A}_{11}\boldsymbol{A}_{12} \tag{2-10}$$

It is to be noted that in Chapter 5, the position of frame o_{12} with respect to frame o_6 is required to calculate the internal force between the two manipulators, the effect of which is simulated by an extension spring. Therefore, transformation from o_0 to o_{02} is calculated by:

$$\boldsymbol{A}_{02}^0 = \begin{bmatrix} 1 & 0 & 0 & 0 \\ 0 & 1 & 0 & l \\ 0 & 0 & 1 & 0 \\ 0 & 0 & 0 & 1 \end{bmatrix} \tag{2-11}$$

where l is the distance of two UR5 bases. The position of frame o_{12} with respect to frame o_0 is obtained by:

$$\boldsymbol{T}_{12}^0 = \boldsymbol{A}_{02}^0\boldsymbol{A}_7\boldsymbol{A}_8\boldsymbol{A}_9\boldsymbol{A}_{10}\boldsymbol{A}_{11}\boldsymbol{A}_{12} \tag{2-12}$$

For the purpose of simplification, term $\boldsymbol{B}$ is introduced to show the displacement between the end effectors and obtained by:

$$\boldsymbol{B} = \boldsymbol{T}_{12}^0 - \boldsymbol{T}_6^0 \tag{2-13}$$

Consequently, the position of frame o_{12} with respect to frame o_6 is expressed in the base frame o_0 by

$[\boldsymbol{B}(1,4) \quad \boldsymbol{B}(2,4) \quad \boldsymbol{B}(3,4)]^T$ and $\boldsymbol{B}(i,j)$ represents the element which is located at the i-th row and j-th column of $\boldsymbol{B}$. The four characteristic parameters of the kinematics of the right manipulator can be found in Table 2-1 and those of the left one are displayed in Table 2-2.

Table 2-2 The DH parameters of slave UR5

Parameters / Joint	θ_i [rad]	a_{i-1} [m]	d_i [m]	α_{i-1} [rad]
7	0	0	0.089159	0
8	0	0	0	π/2
9	0	-0.425	0	0
10	0	-0.39225	0.10915	0
11	0	0	0.09465	π/2
12	0	0	0.0823	-π/2

2.3. Jacobian of the robotic systems

In section 2.2, a model for the forward kinematics is defined to enable calculation of the positions and orientations of the end effector using joint angles. To further analyse the relationships between joints and end effectors, equations relating individual joint velocities to the end effectors velocities are derived. These equations are the Jacobian of the robot position as matrices. The Jacobian can be mathematically deemed the derivative of a scalar function which is expressed in the format of the vector and it is necessary for the manipulation of the manipulators. In particular, it works in the same way of transforming forces and torques exerted on the end effectors to the corresponding torques on the joints as that of velocity transformation. In the following sections, in order to display how to determine the Jacobian of the manipulator, the position of the end effector is defined in the middle of the surface of the sixth link (Link 6 in Fig. 2.2) as an example.

2.3.1. Angular velocity

The Eq. 2-8 can be described as:

$$\boldsymbol{T}_6^0(\boldsymbol{q}_1) = \begin{bmatrix} \boldsymbol{R}_6^0(\boldsymbol{q}_1) & \boldsymbol{o}_6^0(\boldsymbol{q}_1) \\ 0 & 1 \end{bmatrix} \tag{2-14}$$

where $\boldsymbol{q}_1 = [q_1^1 \quad q_1^2 \quad q_1^3 \quad q_1^4 \quad q_1^5 \quad q_1^6]^T$ and q_1^i is velocity of the i-th joint of the master manipulator (Fig. 2.4). When the joints rotate, the orientation $\boldsymbol{R}_6^0(\boldsymbol{q}_1)$ and position $\boldsymbol{o}_6^0(\boldsymbol{q}_1)$ of the end effector are functions of joint position.

According to the definition in section 2.2.1. , the i-th link rotates about Z_i and its angular velocity in frame o_0 can be expressed by:

$$\boldsymbol{\omega}_i^0 = \dot{q}_1^i \, \mathbf{Z}_i^0 \tag{2-15}$$

$\dot{q}_1^i$ denotes the speed of the i-th joint of the first UR5. $\mathbf{Z}_i^0$ is the Z axis of coordinate frame o_i and it is expressed in coordinate frame o_0. Therefore, the angular velocity of the end effector, which is expressed in coordinate frame o_0, is

calculated by:

$$\boldsymbol{\omega}_6^0 = \sum_{i=1}^{6} \dot{q}_1^i \, \mathbf{Z}_i^0 \tag{2-16}$$

Therefore, the part of the manipulator Jacobian related to angular velocity is expressed as:

$$\boldsymbol{J}_{w\_1} = [\mathbf{Z}_1^0 \quad \mathbf{Z}_2^0 \quad \mathbf{Z}_3^0 \quad \mathbf{Z}_4^0 \quad \mathbf{Z}_5^0 \quad \mathbf{Z}_6^0] \tag{2-17}$$

2.3.2. Linear velocity

According to Eq. 2-14, $\boldsymbol{o}_6^0(\boldsymbol{q}_1)$ is the position of the end effector. Therefore, the linear velocity of the end effector can be calculated by the derivate of position with respect to time:

$$\dot{\boldsymbol{o}}_6^0(\boldsymbol{q}_1) = \sum_{i=1}^{6} \dot{q}_1^i \cdot \partial \boldsymbol{o}_6^0 / \partial q_1^i \tag{2-18}$$

The UR5 consists of 6 rotating joints, and the velocity of the end effector expressed in frame o_0 is calculated:

$$\dot{\boldsymbol{o}}_6^0(\boldsymbol{q}_1) = \sum_{i=1}^{6} \dot{q}_1^i \, \mathbf{Z}_i^0 \times (\boldsymbol{o}_6^0 - \boldsymbol{o}_i^0) \tag{2-19}$$

Therefore, the part of the manipulator Jacobian related to linear velocity is expressed as:

$$\boldsymbol{J}_{v\_1} = [\mathbf{Z}_1^0 \times (\boldsymbol{o}_6^0 - \boldsymbol{o}_1^0) \quad \ldots \quad \mathbf{Z}_6^0 \times (\boldsymbol{o}_6^0 - \boldsymbol{o}_6^0)] \tag{2-20}$$

2.3.3. Combination of the angular and linear velocity

With the conclusions captured in the past two sections, the Jacobian of the first manipulator is expressed as:

$$\boldsymbol{J}_1 = \begin{bmatrix} \boldsymbol{J}_{v\_1} \\ \boldsymbol{J}_{w\_1} \end{bmatrix} \tag{2-21}$$

The velocity of the end effector can be calculated using a simplified way:

$$\boldsymbol{v}_6^0 = \boldsymbol{J}_1 \dot{\boldsymbol{q}}_1 \tag{2-22}$$

where $\dot{\boldsymbol{q}}_1 = [\dot{q}_1^1 \quad \dot{q}_1^2 \quad \dot{q}_1^3 \quad \dot{q}_1^4 \quad \dot{q}_1^5 \quad \dot{q}_1^6]^T$ is the joint velocity of the master UR5.

It should be noticed that, the end effector may be attached in an alternative geometry from the assumptions of the above kinematic model. Consequently, the linear velocity of the end effector changes as its position expressed in frame o_6 varies. Nevertheless, the angular velocity of the end effector stays the same despite of its varying position in frame o_6. Therefore, the manipulator Jacobian is determined according to the way the end effector is attached. Precise details will be presented in relevant chapters.

2.4. Dynamics of the robotic system based on the Euler-Lagrange equations

In this section, dynamics of the robotic system is expressed by the Euler-Lagrange equations, by which the evolution of

the robotic system is displayed subject to holonomic constraints. Each term in the equations is detailed. Derivation of these equations can be found in [90].

2.4.1. Dynamic model of the single-arm robot

For the single master UR5, the rigid dynamic model can be expressed as:

$$\boldsymbol{M}_1(\boldsymbol{q}_1)\ddot{\boldsymbol{q}}_1 + \boldsymbol{C}_1(\boldsymbol{q}_1, \dot{\boldsymbol{q}}_1)\dot{\boldsymbol{q}}_1 + \boldsymbol{G}(\boldsymbol{q}_1) + \boldsymbol{\tau}_{\text{fri\_1}} + \boldsymbol{\tau}_{\text{ext\_1}} + \boldsymbol{\tau}_{\text{dri\_1}} = 0 \tag{2-23}$$

The details of the terms in the above equation can be obtained by:

a. $\boldsymbol{q}_1 = [q_1^1 \quad q_1^2 \quad q_1^3 \quad q_1^4 \quad q_1^5 \quad q_1^6]^T$ is the joint position of the first UR5 and q_1^i denotes the position of the i-th joint. $\dot{\boldsymbol{q}}_1 = [\dot{q}_1^1 \quad \dot{q}_1^2 \quad \dot{q}_1^3 \quad \dot{q}_1^4 \quad \dot{q}_1^5 \quad \dot{q}_1^6]^T$ is the joint velocity of the first UR5 and $\dot{q}_1^i$ denotes the speed of the i-th joint. $\ddot{\boldsymbol{q}}_1 = [\ddot{q}_1^1 \quad \ddot{q}_1^2 \quad \ddot{q}_1^3 \quad \ddot{q}_1^4 \quad \ddot{q}_1^5 \quad \ddot{q}_1^6]^T$ is the joint acceleration of the first UR5 and $\ddot{q}_1^i$ denotes the acceleration of the i-th joint.

b. $\boldsymbol{M}_1(\boldsymbol{q}_1) \in \mathcal{R}^{n\times n}$ is the inertia matrix of the master UR5 and described as:

$$\begin{aligned}\boldsymbol{M}_1(\boldsymbol{q}_1) = \Bigg[\sum_{i=1}^{n} \Big\{ & m_i [\boldsymbol{J}_{v\_1_i}(\boldsymbol{q}_{1\_i}) \quad 0_{3\times(n-i)}]^T [\boldsymbol{J}_{v\_1_i}(\boldsymbol{q}_{1\_i}) \quad 0_{3\times(n-i)}] \\ & + [\boldsymbol{J}_{\omega\_1_i}(\boldsymbol{q}_{1\_i}) \quad 0_{3\times(n-i)}]^T \boldsymbol{R}_i(\boldsymbol{q}_{1\_i}) \boldsymbol{I}_i \boldsymbol{R}_i(\boldsymbol{q}_{1\_i})^T [\boldsymbol{J}_{\omega\_1_i}(\boldsymbol{q}_{1\_i}) \quad 0_{3\times(n-i)}] \Big\} \Bigg]\end{aligned} \tag{2-24}$$

where $\boldsymbol{q}_{1\_i} = [q_1^1 \quad \dots \quad q_1^i]^T$, m_i is the mass of the i-th link, and $\boldsymbol{R}_i$ is the orientation transformation between the body-attached-frame of the i-th link and the inertial frame. In this research, $\boldsymbol{R}_i = \boldsymbol{R}_i^0$. $\boldsymbol{I}_i \in \mathcal{R}^{3\times3}$ is the inertia tensor of the i-th link of $\boldsymbol{R}_i$ are provided in section 2.4.2. $\boldsymbol{J}_{\boldsymbol{v\_1}_i}$ and $\boldsymbol{J}_{\boldsymbol{\omega\_1}_i}$ are the first i columns of $\boldsymbol{J}_{v\_1}$ and $\boldsymbol{J}_{\boldsymbol{\omega}\_1}$ respectively.

c. $\boldsymbol{C}(\boldsymbol{q}_1, \dot{\boldsymbol{q}}_1) \in \mathcal{R}^{n\times n}$ is the Coriolis and centrifugal matrix of the UR5 and its k,j-th element is described as:

$$c_{kj} = \sum_{i=1}^{n} c_{ijk}(\boldsymbol{q}_1)\dot{q}_1^i = \sum_{i=1}^{n} \frac{1}{2}\left\{\frac{\partial m_{kj}}{\partial q_1^i} + \frac{\partial m_{ki}}{\partial q_1^j} - \frac{\partial m_{ij}}{\partial q_1^k}\right\}\dot{q}_1^i \tag{2-25}$$

where m_{kj} is the k,j-th element of $\boldsymbol{M}_1(\boldsymbol{q}_1)$.

d. $\boldsymbol{G}_1(\boldsymbol{q}_1) \in \mathcal{R}^n$ is the gravity of the first UR5 and expressed as:

$$\boldsymbol{G}_1(\boldsymbol{q}_1) = \boldsymbol{gra} \cdot \boldsymbol{g}_1(\boldsymbol{q}_1) \tag{2-26}$$

where $\boldsymbol{g}_1(\boldsymbol{q}_1) = [g_1^1(\boldsymbol{q}) \quad g_1^2(\boldsymbol{q}) \quad g_1^3(\boldsymbol{q}) \quad g_1^4(\boldsymbol{q}) \quad g_1^5(\boldsymbol{q}) \quad g_1^6(\boldsymbol{q})]^T$ and $\boldsymbol{gra}$ is vector giving the direction of gravity in the inertial frame. $g_1^i(\boldsymbol{q}) = \partial P_1/\partial q_i$. The function $P_1 = \sum_{i=1}^{n} m_i \cdot \boldsymbol{gra}^T \cdot \boldsymbol{r}_{ci}$ provides the potential energy of the first UR5. $\boldsymbol{r}_{ci}$ is the coordinates of the centre of mass of link i, which can be found in section 2.4.2.

e. $\boldsymbol{\tau}_{\text{fri\_1}} \in \mathcal{R}^n$ is the joint friction of the first UR5.

f. $\boldsymbol{\tau}_{\text{dri\_1}} \in \mathcal{R}^n$ is the joint driving torques of the first UR5.

g. $\boldsymbol{\tau}_{\text{ext\_1}} \in \boldsymbol{\mathcal{R}}^n$ is the joint torques caused by the external wrench exerted on the single-arm system $\boldsymbol{f}_1 \in \boldsymbol{\mathcal{R}}^m$. It is worth noting that $m \leq n$ is possible since the external wrench in $n - m$ directions could be null vectors. $\boldsymbol{\tau}_{\text{ext\_1}}$ is related to $\boldsymbol{f}_1$ by the first manipulator Jacobian matrix:

$$\boldsymbol{\tau}_{\text{ext\_1}} = \boldsymbol{J}_1^T \cdot \boldsymbol{f}_1 \tag{2-27}$$

2.4.2. Inertial parameters of the UR5

The position of the mass centre of link *i* is expressed in the *i*-th coordinate frame in [91]. It is to be noticed that the modified DH coordinate frame is employed in this research. Therefore, the centres of mass are different from [91], in which the standard DH coordinate frame is used. The mass of each link [91] and the modified position of the mass centre are displayed in Table 2-3.

Table 2-3 Dynamic parameters of the UR5

Parameters / Link	Mass [kg]	Centre of Mass [m]
1	3.7	[0, -0.00193, 0.02561]
2	8.393	[-0.2125, 0, 0.11336]
3	2.33	[-0.24225, 0, 0.0265]
4	1.219	[0, -0.01634, -0.0018]
5	1.219	[0, 0.01634, -0.0018]
6	0.1879	[0, 0, -0.001159]

The inertial tensor of link *i*, which is involved in Eq. 2-24, is expressed in the coordinate whose origin is located at the centroid of link i and can be obtained from [91]:

$$\boldsymbol{I}_1 = \begin{bmatrix} 0.0084 & 0 & 0 \\ 0 & 0.0084 & 0 \\ 0 & 0 & 0.0064 \end{bmatrix} \tag{2-28}$$

$$\boldsymbol{I}_2 = \begin{bmatrix} 0.0078 & 0 & 0 \\ 0 & 0.2100 & 0 \\ 0 & 0 & 0.2100 \end{bmatrix} \tag{2-29}$$

$$\boldsymbol{I}_3 = \begin{bmatrix} 0.0016 & 0 & 0 \\ 0 & 0.0462 & 0 \\ 0 & 0 & 0.0462 \end{bmatrix} \tag{2-30}$$

$$\boldsymbol{I}_4 = \begin{bmatrix} 0.0016 & 0 & 0 \\ 0 & 0.0009 & 0 \\ 0 & 0 & 0.0016 \end{bmatrix} \tag{2-31}$$

$$\boldsymbol{I}_5 = \begin{bmatrix} 0.0016 & 0 & 0 \\ 0 & 0.0009 & 0 \\ 0 & 0 & 0.0016 \end{bmatrix} \tag{2-32}$$

$$\boldsymbol{I}_6 = \begin{bmatrix} 0.0001 & 0 & 0 \\ 0 & 0.0001 & 0 \\ 0 & 0 & 0.0001 \end{bmatrix} \tag{2-33}$$

2.4.3. Model of the external wrench

The external wrench is modeled as:

$$\dot{\boldsymbol{f}}_1 = \boldsymbol{S}_1 \boldsymbol{f}_1 + \boldsymbol{e}_{f\_1} \tag{2-34}$$

where $\boldsymbol{S}_1 \in \boldsymbol{\mathcal{R}}^{m\times m}$ is the dynamic matrix of the contact force and torque on the single-arm system. Normally, the term $\boldsymbol{S}_1$ is defined according to the nature of the contact force/torque and it can be divided into constant contact, high-order contact, and harmonic contact. In this work, the payload on the UR5 can be regarded as constant, though there is sudden force and torque on the manipulator within a very short period. Furthermore, *a-priori* information of the external force is not available in most actual cases. Therefore, $\boldsymbol{S}_1$ usually defaults to 0 and $\dot{\boldsymbol{f}}_1 = \boldsymbol{e}_{f\_1}$ [95]. The common choice for $\boldsymbol{e}_{f\_1}$ are positive gains and larger diagonal elements of $\boldsymbol{\sigma}_{f\_1}^2$ are preferred in order to decrease the effect of contact force/torque change and reduce response time. However, the diagonal elements must be limited to a certain magnitude as large diagonal elements can increase the effect of the estimation noise. The problem is mitigated in the proposed approach with the introduction of the MSMA based on variable time period. Thus, during the same response period (with the same $\boldsymbol{\sigma}_{f\_1}^2$), the effect of noise is lower than that caused by the CKF.

2.4.4. Dynamic model of the dual-arm system

With the dynamics of the master UR5, the model of the slave UR5 can be obtained in the same way. Consequently, the rigid body dynamics of coordinated robotic system consisting of two UR5 is expressed as:

$$\underbrace{\begin{bmatrix}\boldsymbol{M}_1(\boldsymbol{q}_1) & 0_{n\times n}\\ 0_{n\times n} & \boldsymbol{M}_2(\boldsymbol{q}_2)\end{bmatrix}}_{\boldsymbol{M}(\boldsymbol{q})}\underbrace{\begin{bmatrix}\ddot{\boldsymbol{q}}_1\\ \ddot{\boldsymbol{q}}_2\end{bmatrix}}_{\ddot{\boldsymbol{q}}} + \underbrace{\begin{bmatrix}\boldsymbol{C}_1(\boldsymbol{q}_1,\dot{\boldsymbol{q}}_1) & 0_{n\times n}\\ 0_{n\times n} & \boldsymbol{C}_2(\boldsymbol{q}_2,\dot{\boldsymbol{q}}_2)\end{bmatrix}}_{\boldsymbol{C}_1(\boldsymbol{q},\dot{\boldsymbol{q}})}\underbrace{\begin{bmatrix}\dot{\boldsymbol{q}}_1\\ \dot{\boldsymbol{q}}_2\end{bmatrix}}_{\dot{\boldsymbol{q}}} + \underbrace{\begin{bmatrix}\boldsymbol{G}_1(\boldsymbol{q}_1)\\ \boldsymbol{G}_2(\boldsymbol{q}_2)\end{bmatrix}}_{\boldsymbol{G}(\boldsymbol{q})} + \underbrace{\begin{bmatrix}\boldsymbol{\tau}_{\text{fri\_1}}\\ \boldsymbol{\tau}_{\text{fri\_2}}\end{bmatrix}}_{\boldsymbol{\tau}_{\text{fri}}}$$
$$+ \underbrace{\begin{bmatrix}\boldsymbol{\tau}_{\text{ext\_1}}\\ \boldsymbol{\tau}_{\text{ext\_2}}\end{bmatrix}}_{\boldsymbol{\tau}_{\text{ext}}} + \underbrace{\begin{bmatrix}\boldsymbol{\tau}_{\text{int\_1}}\\ \boldsymbol{\tau}_{\text{int\_2}}\end{bmatrix}}_{\boldsymbol{\tau}_{\text{int}}} + \underbrace{\begin{bmatrix}\boldsymbol{\tau}_{\text{dri\_1}}\\ \boldsymbol{\tau}_{\text{dri\_2}}\end{bmatrix}}_{\boldsymbol{\tau}_{\text{dri}}} = 0 \tag{2-35}$$

$\boldsymbol{M}_i(\boldsymbol{q}_i) \in \mathcal{R}^{n\times n}$ is the inertia matrix of the i-th UR5. $\boldsymbol{q}_i \in \boldsymbol{\mathcal{R}}^n$, $\dot{\boldsymbol{q}}_i \in \boldsymbol{\mathcal{R}}^n$, and $\ddot{\boldsymbol{q}}_i \in \boldsymbol{\mathcal{R}}^n$ represent the joint position, speed, and acceleration of the i-th UR5. $\boldsymbol{C}_i(\boldsymbol{q}_i,\dot{\boldsymbol{q}}_i) \in \boldsymbol{\mathcal{R}}^{n\times n}$ denotes the Coriolis and centrifugal matrix of the i-th UR5. The gravity of the i-th UR5 is expressed as $\boldsymbol{G}_i(\boldsymbol{q}_i) \in \boldsymbol{\mathcal{R}}^{n\times n}$. $\boldsymbol{\tau}_{\text{fri\_}i} \in \boldsymbol{\mathcal{R}}^n$ is the joint friction of the i-th UR5. $\boldsymbol{\tau}_{\text{int\_}i}$ is the joint torques exerted on the i-th UR5, which result from the internal force between the two arms. $\boldsymbol{\tau}_{\text{dri\_}i} \in \boldsymbol{\mathcal{R}}^n$ is the joint driving torques of the i-th UR5. $\boldsymbol{\tau}_{\text{ext\_}i} \in \boldsymbol{\mathcal{R}}^n$ is the joint torques resulting from the external wrench $\boldsymbol{f} \in \boldsymbol{\mathcal{R}}^m$ (m is the dimension of the external wrench), which is exerted on both arms by:

$$\boldsymbol{f} = \boldsymbol{f}_1 + \boldsymbol{f}_2 \tag{2-36}$$

$\boldsymbol{f}_i$ is related to $\boldsymbol{\tau}_{\text{ext\_}i}$ by the Jacobians $\boldsymbol{J}_i(\boldsymbol{q}_i) \in \boldsymbol{\mathcal{R}}^{m\times n}$ of the i-th UR5 joint via the equation:

$$\boldsymbol{\tau}_{\text{ext\_}i} = \boldsymbol{J}_i^T(\boldsymbol{q}_i)\boldsymbol{f}_i \tag{2-37}$$

$\boldsymbol{\tau}_{\text{int\_1}}$ and $\boldsymbol{\tau}_{\text{int\_2}}$ are the joint torques resulting from the internal force/torque between the two arms.

To mitigate unnecessary complication when validating the proposed method on the dual-arm system, two UR5 robots

were instructed to perform mirrored movements in Section 7.1.1. and Section 8.1.1. Thus, the tool centre point was located in the middle of the end effectors of the two robots. Therefore, many elements in the dynamic model can be regarded as null and estimation results based on Eq. 2-35 can be assumed correct. However, it must be noted that this is a special condition. This work is mainly focused on designing an adaptive Kalman filter, calibrating it and validating it on different systems. Hence, a simplified model and setup are employed in the experiments. Hence, while deriving the dynamic model that incorporates the constraint equations is possible, it was extraneous to the goals of this thesis. Reformulating the model to incorporate the constraint may form the next logical step in this research stream.

2.5. Dynamics of the robotic system in the format of the generalized momentum

Typically, the acceleration is not measured directly, but is obtained by numerical differentiation of the measured position. However, unavoidable measurement noise amplification occurs during this process. Furthermore, numerical differentiation can cause extra computational burden since real-time information of the acceleration is required in the CFTE. Consequently, the generalized momentum model proposed by De Luca *et al.* is employed in this research.

2.5.1. Modified dynamic model of the single-arm robot

In order to use the generalized-momentum-based model, the generalized momentum $\boldsymbol{p}_1$ of the first UR5 is defined as:

$$\boldsymbol{p}_1 = \boldsymbol{M}_1(\boldsymbol{q}_1)\dot{\boldsymbol{q}}_1 \tag{2-38}$$

The derivate of $\boldsymbol{p}_1$ with respect to time is consequently obtained:

$$\dot{\boldsymbol{p}}_1 = \dot{\boldsymbol{M}}_1(\boldsymbol{q}_1)\dot{\boldsymbol{q}}_1 + \boldsymbol{M}_1(\boldsymbol{q}_1)\ddot{\boldsymbol{q}}_1 \tag{2-39}$$

According to the conclusion in 0, the property of anti-symmetry of $\dot{\boldsymbol{M}}_1(\boldsymbol{q}_1) - \boldsymbol{2C}_1(\boldsymbol{q}_1, \dot{\boldsymbol{q}}_1)$ is utilized and expressed as:

$$\dot{\boldsymbol{M}}_1(\boldsymbol{q}_1) - \boldsymbol{2C}_1(\boldsymbol{q}_1, \dot{\boldsymbol{q}}_1) = -\left(\dot{\boldsymbol{M}}_1(\boldsymbol{q}_1) - \boldsymbol{2C}_1(\boldsymbol{q}_1, \dot{\boldsymbol{q}}_1)\right)^T \tag{2-40}$$

and Eq. 2-23 can then be expressed as:

$$\dot{\boldsymbol{p}}_1 = \boldsymbol{C}_1(\boldsymbol{q}_1, \dot{\boldsymbol{q}}_1)^T\dot{\boldsymbol{q}}_1 - \boldsymbol{G}_1(\boldsymbol{q}_1) - \boldsymbol{\tau}_{\text{fri\_1}} - \boldsymbol{\tau}_{\text{ext\_1}} - \boldsymbol{\tau}_{\text{dri\_1}} \tag{2-41}$$

In order to simplify the above equation, the term $\boldsymbol{\tau}_{\text{inp\_1}}$ is defined as:

$$\boldsymbol{\tau}_{\text{inp\_1}} = \boldsymbol{C}_1(\boldsymbol{q}_1, \dot{\boldsymbol{q}}_1)^T\dot{\boldsymbol{q}}_1 - \boldsymbol{G}_1(\boldsymbol{q}_1) - \boldsymbol{\tau}_{\text{fri\_1}} - \boldsymbol{\tau}_{\text{dri\_1}} \tag{2-42}$$

It should be noticed that, although dynamic properties of the UR5 achieved from the manufacturer are assumed to be precise in this research, uncertainty in $\boldsymbol{\tau}_{\text{inp\_1}}$ cannot be avoided due to measurement noise. The magnitude of the noise in the measured motor current is much larger than the noise in the measured motor position and velocity, and can thus be ignored. So it is reasonable to consider the uncertainty in $\boldsymbol{\tau}_{\text{fri\_1}}$ and $\boldsymbol{\tau}_{\text{dri\_1}}$ as the dominant noise in $\boldsymbol{\tau}_{\text{inp\_1}}$. The noise is

expressed as $\boldsymbol{e}_{p\_1}$. With $\boldsymbol{e}_{p\_1} \sim N(0, \boldsymbol{\sigma}^2_{\text{Dyn\_1}})$, $\boldsymbol{\sigma}^2_{\text{Dyn\_1}}$ is assumed as a diagonal matrix reflecting that errors in the individual joints are independent and $\boldsymbol{\sigma}^2_{\text{Dyn\_1}} \in \boldsymbol{\mathcal{R}}^{n\times n}$. Therefore, Eq. 2-42 can be modified as:

$$\boldsymbol{\tau}_{\text{inp\_1}} = \boldsymbol{C}_1(\boldsymbol{q}_1, \dot{\boldsymbol{q}}_1)^T \dot{\boldsymbol{q}}_1 - \boldsymbol{G}_1(\boldsymbol{q}_1) - \boldsymbol{\tau}_{\text{fri\_1}} - \boldsymbol{\tau}_{\text{dri\_1}} + \boldsymbol{e}_{p\_1} \tag{2-43}$$

and Eq. 2-41 is then described as:

$$\dot{\boldsymbol{p}}_1 = \boldsymbol{\tau}_{\text{inp\_1}} - \boldsymbol{J}_1^T(\boldsymbol{q}_1)\boldsymbol{f}_1 \tag{2-44}$$

2.5.2. Modified dynamic model of the dual-arm robot

Similar to the modification in the above section, the generalized momentum $\boldsymbol{p}$ of the dual-arm system is defined as $\boldsymbol{p} = \boldsymbol{M}(\boldsymbol{q})\dot{\boldsymbol{q}}$ and thus Eq. 2-35 is described as:

$$\dot{\boldsymbol{p}} = \boldsymbol{\tau}_{\text{inp}} - \boldsymbol{J}^T(\boldsymbol{q}_1, \boldsymbol{q}_2)\boldsymbol{f}_{\text{ext}} \tag{2-45}$$

The combined external wrench $\boldsymbol{f}_{\text{ext}} \in \boldsymbol{\mathcal{R}}^{2m}$, the combined Jacobian matrix $\boldsymbol{J}(\boldsymbol{q}_1, \boldsymbol{q}_2) \in \boldsymbol{\mathcal{R}}^{2m\times 2n}$, the combined input term $\boldsymbol{\tau}_{\text{inp}} \in \boldsymbol{\mathcal{R}}^{2n}$, and the combined uncertainty of the systematic dynamics $\boldsymbol{e}_p \in \boldsymbol{\mathcal{R}}^{2n}$ are defined as:

$$\boldsymbol{f}_{\text{ext}} = \begin{bmatrix} \boldsymbol{f}_1 \\ \boldsymbol{f}_2 \end{bmatrix} \tag{2-46}$$

$$\boldsymbol{J}(\boldsymbol{q}_1, \boldsymbol{q}_2) = \begin{bmatrix} \boldsymbol{J}_1(\boldsymbol{q}_1) & 0_{m\times n} \\ 0_{m\times n} & \boldsymbol{J}_2(\boldsymbol{q}_2) \end{bmatrix} \tag{2-47}$$

$$\boldsymbol{\tau}_{\text{inp}} = \boldsymbol{C}(\boldsymbol{q}, \dot{\boldsymbol{q}})^T \dot{\boldsymbol{q}} - \boldsymbol{G}(\boldsymbol{q}) - \boldsymbol{\tau}_{\text{fri}} - \boldsymbol{\tau}_{\text{dri}} + \boldsymbol{e}_p \tag{2-48}$$

$$\boldsymbol{e}_p = \begin{bmatrix} \boldsymbol{e}_{p\_1} \\ \boldsymbol{e}_{p\_2} \end{bmatrix} \tag{2-49}$$

2.6. Discretized model of the robot

In order to apply the conventional Kalman filter, the dynamics of both the single-arm and dual-arm systems must be expressed in the discretized form. Furthermore, the dynamic terms, such as the inertial matrices and the manipulator Jacobians, are transient. Therefore, discretization of the linear time-varying robotic system is performed and state space models of the robots are obtained to enable application of the conventional Kalman filter.

2.6.1. Discretized model of the single-arm robot

The state model of the first robotic manipulator is described as:

$$\begin{aligned} \dot{\boldsymbol{x}}_1 &= \boldsymbol{A}_1\boldsymbol{x}_1 + \boldsymbol{B}_1\boldsymbol{u}_1 + \boldsymbol{w}_1 \\ \boldsymbol{y}_1 &= \boldsymbol{C}_1\boldsymbol{x}_1 + \boldsymbol{Z}_1 \end{aligned} \tag{2-50}$$

The state space vector of the single-arm dynamics is defined as:

$$\boldsymbol{x}_1 = \begin{bmatrix} \boldsymbol{p}_1 \\ \boldsymbol{f}_1 \end{bmatrix} \in \mathcal{R}^{n+m} \tag{2-51}$$

The State matrix is defined as:

$$\boldsymbol{A}_1 = \begin{bmatrix} 0_{n\times n} & -\boldsymbol{J}_1^T \\ 0_{m\times n} & \boldsymbol{S}_1 \end{bmatrix} \tag{2-52}$$

The input matrix is defined as:

$$\boldsymbol{B}_1 = \begin{bmatrix} \boldsymbol{I}_n \\ 0_{n\times m} \end{bmatrix} \tag{2-53}$$

The output matrix is defined as:

$$\boldsymbol{C}_1 = [\boldsymbol{I}_n, 0_{n\times m}] \tag{2-54}$$

The covariance matrix of the predicted state noise is defined as:

$$\boldsymbol{w}_1 = \begin{bmatrix} \boldsymbol{e}_{p\_1} \\ \boldsymbol{e}_{f\_1} \end{bmatrix} \in \boldsymbol{\mathcal{R}}^{n+m} \tag{2-55}$$

The input vector is defined as:

$$\boldsymbol{u}_1 = \boldsymbol{\tau}_{\text{inp\_1}} \tag{2-56}$$

The measurement noise is defined as $\boldsymbol{Z}_1 \sim N\left(0, \boldsymbol{\sigma}^2_{\text{mea\_1}}\right)$. Details of calculating $\boldsymbol{\sigma}^2_{\text{mea\_1}} \in \boldsymbol{\mathcal{R}}^{n\times n}$ can be found in the next chapter. With all the terms identified, the discretized state space dynamics is then obtained:

$$\begin{aligned} \boldsymbol{x}_{k+1\_1} &= \boldsymbol{A}_{k+1\_1}\boldsymbol{x}_{k\_1} + \boldsymbol{B}_{k+1\_1}\boldsymbol{u}_{k+1\_1} + \boldsymbol{w}_{k+1\_1} \\ \boldsymbol{y}_{k+1\_1} &= \boldsymbol{C}_{k+1\_1}\boldsymbol{x}_{k+1\_1} + \boldsymbol{z}_{k+1\_1} \end{aligned} \tag{2-57}$$

where k and $k+1$ represent the time steps of the discretized model. Following [97], the discretized state matrices are expressed as:

$$\begin{aligned} \begin{bmatrix} \boldsymbol{A}_{k+1\_1} & \boldsymbol{B}_{k+1\_1} \\ 0_{n\times(n+m)} & \boldsymbol{I}_n \end{bmatrix} &= \exp\left(\begin{bmatrix} \boldsymbol{A}_1 & \boldsymbol{B}_1 \\ 0_{n\times(n+m)} & 0_{n\times n} \end{bmatrix} t_s\right) \\ \boldsymbol{C}_{k+1\_1} &= \boldsymbol{C} \end{aligned} \tag{2-58}$$

According to Eq. 2-52, $\boldsymbol{A}_1$ is time-varying due to the continuously varying Jacobian matrix $-\boldsymbol{J}_1^T$. The same conclusion can be applied to the dual-arm case.

The covariance matrix of the noise caused by measurement is described as:

$$\boldsymbol{\sigma}^2_{k+1\_1} = \boldsymbol{\sigma}^2_{\text{mea\_1}}/t_s \tag{2-59}$$

where t_s is the sampling time. According to the conclusion in [98], the discretized predicted state noise matrix $\boldsymbol{Q}_{k+1}$ is calculated by:

$$\begin{aligned} \begin{bmatrix} \boldsymbol{M}^{11}_{k+1\_1} & \boldsymbol{M}^{12}_{k+1\_1} \\ 0_{(n+m)\times(n+m)} & \boldsymbol{M}^{22}_{k+1\_1} \end{bmatrix} &= \exp\left(\begin{bmatrix} \boldsymbol{A}_1 & \boldsymbol{\sigma}^2_{\text{pro\_1}} \\ 0_{(n+m)\times(n+m)} & -\boldsymbol{A}_1 \end{bmatrix} t_s\right) \\ \boldsymbol{Q}_{k+1} &= \left(\boldsymbol{M}^{22}_{k+1\_1}\right)^T \boldsymbol{M}^{12}_{k+1\_1} \end{aligned} \tag{2-60}$$

where the covariance matrix of the predicted state noise is expressed as:

$$\boldsymbol{\sigma}^2_{\text{pro\_1}} = \begin{bmatrix} \boldsymbol{\sigma}^2_{\text{Dyn\_1}} & 0_{m\times n} \\ 0_{n\times m} & \boldsymbol{\sigma}^2_{f\_1} \end{bmatrix} \tag{2-61}$$

2.6.2. Discretization of the dual-arm system

Discretization of the dual-arm robotic systems is similar to that of the single one. The state model is described as:

$$\begin{aligned} \dot{\boldsymbol{x}} &= \boldsymbol{A}\boldsymbol{x} + \boldsymbol{B}\boldsymbol{u} + \boldsymbol{w} \\ \boldsymbol{y} &= \boldsymbol{C}\boldsymbol{x} + \boldsymbol{Z} \end{aligned} \tag{2-62}$$

The state space vector of the dual-arm dynamics is defined as:

$$\boldsymbol{x} = \begin{bmatrix} \boldsymbol{p} \\ \boldsymbol{f} \end{bmatrix} \in \mathcal{R}^{2n+2m} \tag{2-63}$$

and $\boldsymbol{A} = \begin{bmatrix} 0_{2n\times 2n} & -\boldsymbol{J}_1^T \\ 0_{2m\times 2n} & \boldsymbol{S} \end{bmatrix}$, $\boldsymbol{B} = \begin{bmatrix} \boldsymbol{I}_{2n} \\ 0_{2n\times 2m} \end{bmatrix}$, and $\boldsymbol{C} = [\boldsymbol{I}_{2n}, 0_{2n\times 2m}]$ are state matrices. $\boldsymbol{S} = \begin{bmatrix} \boldsymbol{S}_1 & 0_{m\times m} \\ 0_{m\times m} & \boldsymbol{S}_2 \end{bmatrix}$ and $\boldsymbol{S}_i$ are the dynamic matrix of external force and torque exerted on the i-th UR5. $\boldsymbol{w} = \begin{bmatrix} \boldsymbol{e_p} \\ \boldsymbol{e_f} \end{bmatrix} \in \mathcal{R}^{2n+2m}$ is the covariance matrix of the predicted state noise. $\boldsymbol{e}_p = \begin{bmatrix} \boldsymbol{e}_{p\_1} \\ \boldsymbol{e}_{p\_2} \end{bmatrix} \in \boldsymbol{\mathcal{R}}^{2n}$ and $\boldsymbol{e}_f = \begin{bmatrix} \boldsymbol{e}_{f\_1} \\ \boldsymbol{e}_{f\_2} \end{bmatrix} \in \boldsymbol{\mathcal{R}}^{2m}$. $\boldsymbol{u} = \boldsymbol{\tau}_{\text{inp}}$ denotes the input of the state model and $\boldsymbol{\tau}_{\text{inp}} = \begin{bmatrix} \boldsymbol{\tau}_{\text{inp\_1}} \\ \boldsymbol{\tau}_{\text{inp\_2}} \end{bmatrix}$. The measurement noise is $\boldsymbol{Z}\sim N(0, \boldsymbol{\sigma}^2_{\text{mea}})$ with $\boldsymbol{\sigma}^2_{\text{mea}} = \begin{bmatrix} \boldsymbol{\sigma}^2_{\text{mea\_1}} & 0_{n\times n} \\ 0_{n\times n} & \boldsymbol{\sigma}^2_{\text{mea\_2}} \end{bmatrix} \in \mathcal{R}^{2n\times 2n}$. The discretized state space dynamics is then obtained:

$$\begin{aligned} \boldsymbol{x}_{k+1} &= \boldsymbol{A}_{k+1}\boldsymbol{x}_k + \boldsymbol{B}_{k+1}\boldsymbol{u}_{k+1} + \boldsymbol{w}_{k+1} \\ \boldsymbol{y}_{k+1} &= \boldsymbol{C}_{k+1}\boldsymbol{x}_{k+1} + \boldsymbol{z}_{k+1} \end{aligned}$$

where k and $k+1$ represent the time steps of the discretized model. The discretized state matrices are expressed as:

$$\begin{aligned} \begin{bmatrix} \boldsymbol{A}_{k+1} & \boldsymbol{B}_{k+1} \\ 0_{2n\times(2n+2m)} & \boldsymbol{I}_{2n} \end{bmatrix} &= \exp\left(\begin{bmatrix} \boldsymbol{A} & \boldsymbol{B} \\ 0_{2n\times(2n+2m)} & 0_{2n\times 2n} \end{bmatrix} t_s\right) \\ \boldsymbol{C} &= \boldsymbol{C}_{k+1} \end{aligned}$$

The covariance matrix of the noise caused by measurement is described as:

$$\boldsymbol{\sigma}^2_{k+1} = \boldsymbol{\sigma}^2_{\text{mea}}/t_s$$

The discretized predicted state noise matrix $\boldsymbol{Q}_{k+1}$ is calculated by:

$$\begin{aligned} \begin{bmatrix} \boldsymbol{M}^{11}_{k+1} & \boldsymbol{M}^{12}_{k+1} \\ 0_{(2n+2m)\times(2n+2m)} & \boldsymbol{M}^{22}_{k+1} \end{bmatrix} &= \exp\left(\begin{bmatrix} \boldsymbol{A} & \boldsymbol{\sigma}^2_{\text{pro}} \\ 0_{(2n+2m)\times(2n+2m)} & -\boldsymbol{A} \end{bmatrix} t_s\right) \\ \boldsymbol{Q}_{k+1} &= (\boldsymbol{M}^{22}_{k+1})^T \boldsymbol{M}^{12}_{k+1} \end{aligned}$$

where the covariance matrix of the predicted state noise is expressed as $\boldsymbol{\sigma}^2_{\text{pro}} = \begin{bmatrix} \boldsymbol{\sigma}^2_{\text{Dyn}} & 0_{2m\times 2n} \\ 0_{2n\times 2m} & \boldsymbol{\sigma}^2_f \end{bmatrix}$.

3. SENSORLESS IDENTIFICATION OF THE DYNAMIC PARAMETERS

In order to capture a precise dynamic model of the robotic systems, identification of the unknown parameters in equation 2-23 and 2-35 must be performed. It may be noted that the physical cost of the proposed method is negligible as additional external sensors are avoided by observing the external contact and modelling the dynamics of the system. In this chapter, sensorless identification of motor constants, joint outputs, joint friction, and errors of the dynamics is conducted.

3.1. Background and motivation

Recently, a Kalman disturbance observer has been applied to sensorless contact force/torque estimation of the robots. Using the extended Kalman filter and a Lyapunov-based adaption law, Jung et al. designed an estimator and applied it to estimate the external wrench of a three-link manipulator [99]. Their proposed estimator was tolerant to model error and sensor noise. The estimator has been further improved and certain assumptions such as *a-priori* determination of underlying patterns that govern subject behavior has been deemed unnecessary [100]. In [95], a semiparametric dynamic model that combines parametric rigid-body dynamics and the nonparametric multilayer perception dynamics is proposed. With the composite model, the force/torque exerted is observed as a disturbance variable and estimated by the disturbance Kalman filter. Subsequently, the uncertainty in dynamics is neglected as unmodelled effects are accounted for by the nonparametric model. Thus, empirical parameters are needed when calibrating the Kalman filter. With an automatic covariance matrix tuning scheme presented in [96], the problem of the neglected dynamic uncertainty in [95] was overcome. The matrix tuning scheme abstracts uncertainty in the system dynamics to improve the estimation quality. However, the covariance matrix in [96] is limited by the errors of the friction model that are generally assumed constant. Furthermore, the scheme remain dependent on joint torque sensors when modelling the friction and the current measurement noise is ignored.

With the contact force/torque estimation method proposed in this thesis, the physical cost will decrease since the external sensors are totally avoided during the process of not only observing the external contact, but modelling the dynamics of the system. To the authors' knowledge, most of the present sensorless force/torque sensing methods depend on expensive experimental setups when building the friction model [92] - [96].

However, the low cost of the proposed approach does not imply inadequate model accuracy. In the proposed approach, the errors resulting from the sensorless-tuned friction model are combined with the noise in the measured current and analyzed. Therefore, all the uncertainties in $\boldsymbol{\tau}_{\mathrm{inp}}$ are considered and the assumption that dynamic errors are dominated by uncertainties in the friction model in [96] is not necessary. The benefit of the proposed method of friction modelling is its ease of implementation. More specifically, independent calculation of its errors is not required but already considered as part of errors in $\boldsymbol{\tau}_{\mathrm{inp}}$. Furthermore, the proposed calibration method can be applied to robotic manipulators in various

engineering scenarios as long as the motor current, joint position, and joint velocities are available.

In the following sections, identification experiments are only conducted on the elbow joint of the master UR5 are shown. Experiments on other joints or the slave UR5 are conducted in a similar manner.

3.2. Experiments and results of parameters identification

Typically, motor constants are accessible from the manufacturer. However, the true value may differ from the nominal characteristics of the motors. Therefore, experimental tests must be conducted to capture precise values. However, external force/torque sensors are also avoided during this process in order to decrease physical cost. In this brief, only the motor current $\boldsymbol{i}_1$, joint position $\boldsymbol{q}_1$, and joint velocity $\dot{\boldsymbol{q}}_1$ are measurable. The joint driving torque is calculated by Eq. 3-1:

$$\widehat{\boldsymbol{\tau}_{\mathrm{dri\_1}}} = \boldsymbol{k}_1 \circ \boldsymbol{r}_1 \circ \boldsymbol{i}_1 \tag{3-1}$$

where $\boldsymbol{k}_1$ and $\boldsymbol{r}_1$ denote the motor torque constant and gearbox ratio, respectively.

3.2.1. Identification of the elbow joint motor constant

In order to calculate the joint driving torques, $\boldsymbol{k}_1 \circ \boldsymbol{r}_1$ must be determined. However, separate identification of $\boldsymbol{k}_1$ and $\boldsymbol{r}_1$ are not necessary. Therefore, a composite term is introduced for simplification of the elbow joint motor parameter as:

$$D_{1\_\mathrm{elb}} = k_{1\_\mathrm{elb}} \cdot r_{1\_\mathrm{elb}} \tag{3-2}$$

The term D_{1_elb} is determined experimentally by moving the joints at a constant speed clockwise and counterclockwise while the other joints were held rigid (as shown in Fig. 3.1).

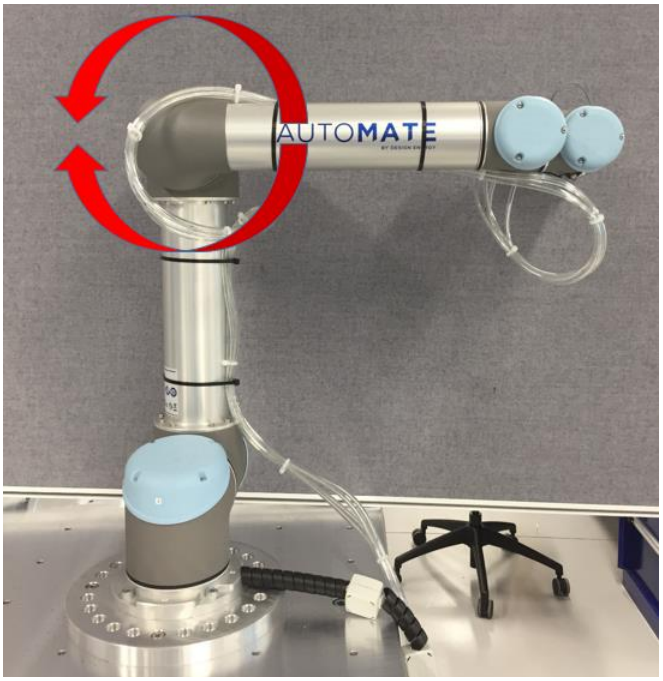

Fig. 3.1. Identification of the motor torque constant and friction.

When the elbow joint rotates clockwise and counterclockwise without the external wrench, the manipulator dynamics

described in terms of current can be expressed as:

$$\begin{aligned} i_{\text{gra}} + i_{\text{fri}} + i_{\text{dri}}^{+} = 0 \\ i_{\text{gra}} - i_{\text{fri}} + i_{\text{dri}}^{-} = 0 \end{aligned} \tag{3-3}$$

where i_{gra} is the current related to the elbow joint torque resulting from the gravity of Link 3, Link 4, Link 5, Link 6, Wrist 1, Wrist 2, and Wrist 3. i_{fri} denotes the current corresponding to the elbow joint friction. i_{dri}^{+} and i_{dri}^{-} indicate the motor currents with the elbow joint moving clockwise and counterclockwise respectively. With Eq. 3-3, i_{gra} is calculated by:

$$i_{\text{gra}} = (-i_{\text{dri}}^{+} - i_{\text{dri}}^{-})/2 \tag{3-4}$$

An accurate dynamic model is thus achieved and the term D_{1_elb} can be obtained by

$$D_{1\_\text{elb}} = G(\boldsymbol{q})/i_{\text{gra}} \tag{3-5}$$

$G(\boldsymbol{q})$ can be determined by the Eq. 2-26 and thus $D_{1\_\text{elb}} = 12.2\ \text{Nm/A}$. It should be noted that $G(\boldsymbol{q})$ is used in Eq. 3-5 is different from the $\boldsymbol{G}(\boldsymbol{q})$ in Eq. 2-23. In particular, it is a scalar rather than a vector. It represents the joint torque resulting from the gravity, for which the motor constant is calculated.

3.2.2. Identification of the elbow joint friction

To simplify the model, only Coulomb friction and viscous friction are considered. Joint friction stems from the relative motion between gears of the harmonic drive, bearings, oil seals and so forth. Therefore, all the frictional damping effects are regarded as a concomitantly:

$$\tau_{\text{fri\_1}}(\dot{q}_1^i) = f_{C\_1}^i + f_{\dot{q}\_1}^i \dot{q}_1^i \tag{3-6}$$

where $i = [1 \quad 2 \quad 3 \quad 4 \quad 5 \quad 6]^T$, $\boldsymbol{f}_{C\_1} = \begin{bmatrix} f_{C\_1}^1 & f_{C\_1}^2 & f_{C\_1}^3 & f_{C\_1}^4 & f_{C\_1}^5 & f_{C\_1}^6 \end{bmatrix}^T$ is the Column friction and $\boldsymbol{f}_{\dot{q}\_1} = \begin{bmatrix} f_{\dot{q}\_1}^1 & f_{\dot{q}\_1}^2 & f_{\dot{q}\_1}^3 & f_{\dot{q}\_1}^4 & f_{\dot{q}\_1}^5 & f_{\dot{q}\_1}^6 \end{bmatrix}$ is the viscous friction coefficient. For individual joints, the corresponding $f_{C\_1}^i$ and $f_{\dot{q}\_1}^i$ are constant. Consequently, the joint friction is a linear function of joint velocity. With Eq. 3-3 and Eq. 3-5, the friction of the elbow joint moving at different speeds is obtained by:

$$\boldsymbol{\tau}_{\text{fri}}(\dot{\boldsymbol{q}}) = D_{1\_\text{elb}}\,(-i_{\text{dri}}^{+} + i_{\text{dri}}^{-})/2 \tag{3-7}$$

Consequently, the unknown parameters $f_{C\_1}^3$ and $f_{\dot{q}\_1}^3$ in Eq. 3-6 can be identified *a-priori*, with $f_{C\_1}^3 = -1.365$ Nm and $f_{\dot{q}\_1}^3 = -0.753$ Nms/rad.

With the dynamic parameters identified, the accuracy of the UR5 can be analyzed and thus the system uncertainty is obtained. It should be noted that the model uncertainty is required to apply the Adaptive Kalman filter.

3.2.3. Identification of the predicted state noise

The term $\boldsymbol{\tau}_{\text{inp\_1}}$ in Eq. 2-44 contains the noise caused by the measurement of $\boldsymbol{q}$, $\dot{\boldsymbol{q}}$, and $\boldsymbol{i}$. In contrast to [96], where the

noise resulting from $\boldsymbol{q}$ and $\boldsymbol{i}$ were ignored, the proposed approach compiles and analyses the kinematic measurement noise. Initially, experiments without external wrench are performed. Since the joint acceleration is not directly measurable, the individual joints were set to move at a constant speed and the ideal joint output torques were calculated by:

$$\overline{\boldsymbol{\tau}_{\mathrm{dri\_1}}} = -\boldsymbol{C}_1(\boldsymbol{q}_1, \dot{\boldsymbol{q}}_1)\dot{\boldsymbol{q}}_1 - \boldsymbol{G}_1(\boldsymbol{q}_1) - \boldsymbol{\tau}_{\mathrm{fri\_1}} \qquad 3\text{-}8$$

The errors between the target driving torques $\overline{\boldsymbol{\tau}_{\mathrm{dri\_1}}}$ and the actual driving torques calculated from Eq. 3-1 are calculated. In a particular experiment, the elbow joint of the master UR5 moves at constant speed with no payload while the motor current is filtered by the pre-filter (WMA or MSMA) with a time period of t. Specification and justification of the pre-filters can be found in Section 4.4. The errors are calculated and displayed in Fig. 3.2.

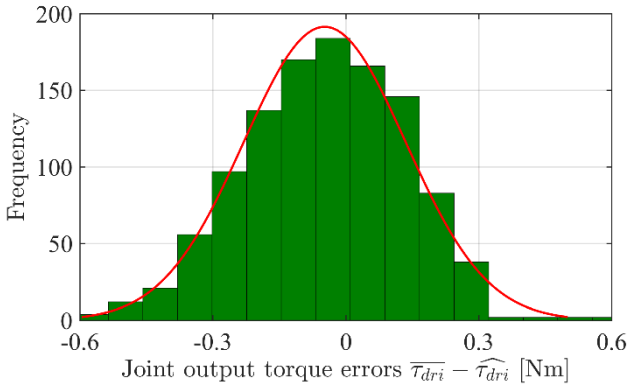

Fig. 3.2. Distribution of joint output errors. The elbow joint is employed as an example and moves without payload. The errors are computed with $\overline{\tau^3_{dri\_1}}$ obtained from Eq. 3-8 and $\widehat{\tau^3_{dri\_1}}$ obtained from Eq. 3-1. The red line (Histfit.m, Matlab R2020b) is fitted to the normal distribution, the variance of which is computed from the empirical standard deviation of the errors.

3.2.4. 1Identification of the measurement noise

In this research, accurate inertial and kinematic parameters of the manipulator are available from the manufactures, and thus the measurement noise in $\boldsymbol{M}(\boldsymbol{q})\dot{\boldsymbol{q}}$ is caused by only noise in the measurements of terms $\boldsymbol{q}$ and $\dot{\boldsymbol{q}}$. The errors in $\dot{\boldsymbol{q}}$ are the dominant part of the measurement noise since $\dot{\boldsymbol{q}}$ is derived from measurable $\boldsymbol{q}$ by numerical differentiation. Differentiation amplifies such errors. In order to extract the errors in $\dot{\boldsymbol{q}}$, each joint of the UR5 manipulator is commanded to move at constant speed, the empirical distribution of the errors between the target velocity $\overline{\dot{\boldsymbol{q}}}$ and the measured speed $\widehat{\dot{\boldsymbol{q}}}$ is shown in Fig. 3.3.

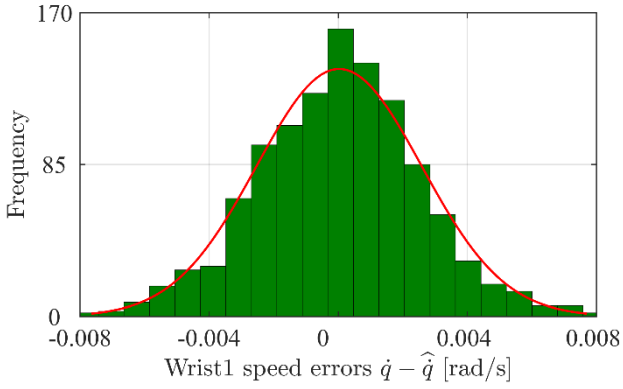

Fig. 3.3. Distribution of the measured joint speed errors. The elbow joint is employed as an example and moves at constant speed. The frequency of the errors is described as a histogram. The errors are computed with the target speed $\bar{\dot{\boldsymbol{q}}}$ and the measured mean speed $\hat{\dot{\boldsymbol{q}}}$. The red line is an added fitted line for the normal distribution, the variance of which is computed from the empirical standard deviation of the errors.

The standard deviation of the elbow joint $\boldsymbol{\sigma}_{\dot{q}}^{\text{elbow}}$ is observed to vary as the speed changes and the trend is depicted in Fig. 3.4. As shown in Fig. 3.4, $\boldsymbol{\sigma}_{\dot{q}}^{\text{elbow}}$ increases approximately linearly with the velocity from speed 0 to 0.13 rad/s and seems to stay approximately constant above that speed.

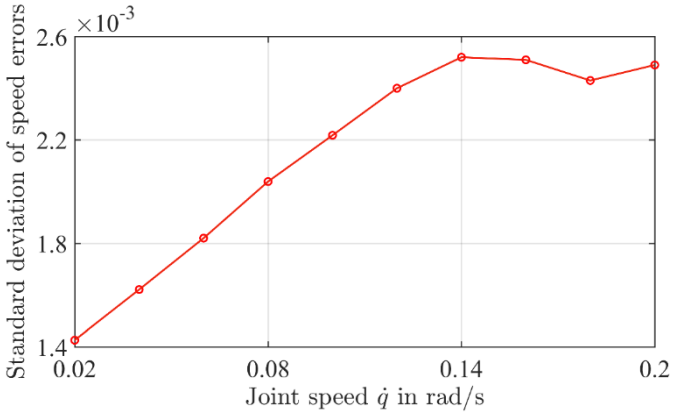

Fig. 3.4. The standard deviation of the elbow joint speed noise at different speeds.

According to Fig. 3.4, the variance of the measurement errors of the elbow joint velocity can be approximated via the following equations:

$$\left(\boldsymbol{\sigma}_{\dot{q}}^{i}\right)^2 = \begin{cases} (a\dot{\boldsymbol{q}}^i + b)^2, \left|\dot{\boldsymbol{q}}^i\right| \le \dot{\boldsymbol{q}}_{\text{thr}}^i \\ c^2, \left|\dot{\boldsymbol{q}}^i\right| > \dot{\boldsymbol{q}}_{\text{thr}}^i \end{cases} \tag{3-9}$$

where $\dot{\boldsymbol{q}}_{\text{thr}}^i$ is a threshold velocity for the i-th joint of the manipulator. a, b, and c are obtained by offline identification experiments related to Fig. 3.4. Similarly, the measurement error equations of the other 5 joints are determined.

The Anderson-Darling test allows an assumption of a Gaussian distribution in velocity error $\dot{\boldsymbol{q}} \sim N\left(\bar{\dot{\boldsymbol{q}}}, \boldsymbol{\sigma}_{\dot{q}}^2\right)$. The measurement noise in Eq. 2-62 can thus be expressed by:

$$\boldsymbol{Z} \sim N(0, \boldsymbol{\sigma}_{\text{mea}}^2) \quad \text{3-10}$$

where $\boldsymbol{\sigma}_{\text{mea}}^2 = \boldsymbol{M}(\boldsymbol{q})\boldsymbol{\sigma}_{\dot{q}}^2\boldsymbol{M}(\boldsymbol{q})$.

3.3. Discussion

3.3.1. Sensorless identification of motor constant and friction

Identification of the motor constant and joint friction in this research is conducted without any force/torque sensors, which can reduce cost. It is worth noting that the friction increases nonlinearly as the relative velocity of the contact surfaces increases from zero to some certain value. Beyond this threshold, friction increases linearly [102]. However, a simplified friction model is used, and each joint is assumed to be moving at speeds beyond particular threshold values. Therefore, the proposed estimation method is still successfully validated on the robotic systems in Chapter 5 to Chapter 8 using the simplified friction model.

However, in reality the joint velocity cannot be guaranteed in general cases and thus a generalized friction model will eventually become valuable. Therefore, a Stribeck friction model or neural network will be employed to model the friction in the future work. Furthermore, the friction is also affected by the loading and temperature. However, these concerns are beyond this research, and details of more friction models can be found in [102].

It is worth noting that the magnitude of i_{gra} in Eq. 3-5 varies through rotation. Therefore the phenomenon of singularity occurred while the i_{gra} fluctuated around 0. To demonstrate that, the elbow joint is used as an example. In this case, the elbow joint (the red square of Fig. 3.5 (b)) was commanded to move from -1.4 rad (around the position as shown in Fig. 3.5 (a)) to -0.2 rad (around the position as shown in Fig. 3.5 (b)) and the corresponding D_{1_elb} was calculated and displayed in Fig. 3.6. As shown in Fig. 4, the real magnitude of the term D_{1_elb} was approximately 12.7. When the joint moved from -1.4 to -0.5 rad, the estimated D_{1_elb} was 12.7 and kept stable. However, the value of D_{1_elb} increased to 50 when the elbow joint moved around the -0.2 rad, as the torque exerted by gravity on the elbow joint was close to 0 ($i_{\text{gra}} \approx 0$). Consequently, a singularity occurred. In order to avoid the singularity, the elbow joint should be commanded to move in regions proximal to $\pi/2$ or $-\pi/2$ rad when calculating D_{1_elb}.

(a) The position $-\pi/2$ around which singularity is avoided.

(b) The position 0 around which singularity occurred.

Fig. 3.5. Different identifying positions of the elbow joint.

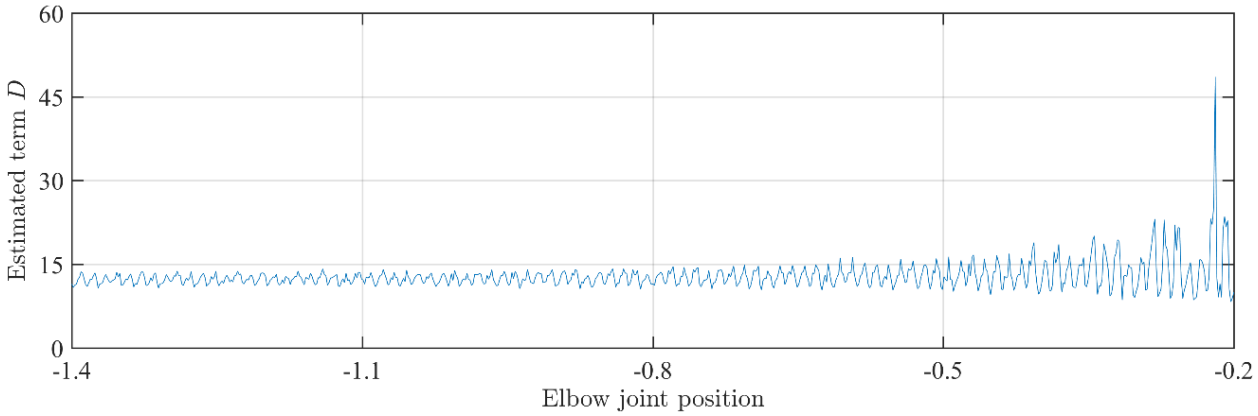

Fig. 3.6. Estimated term D_{1_elb} varies as the joint position changes.

Fig. 3.6 is used to show that when the joint moves near the singularity position (negligible gravity effect on the joint), an imprecise motor constant will be calculated. However there is a wide range of angles for which the motor constant can be precisely calculated (-1.4 to -0.5 rad).

3.3.2. Analysis of the predicted state noise

In the proposed approach, the errors resulting from the sensorless-tuned friction model are combined with the noise in the measured current. Therefore, uncertainties in $\boldsymbol{\tau}_{\text{inp\_1}}$ are considered and the assumption in [96] that dynamic errors are dominated by uncertainties in the friction model is not necessary. The benefit of the proposed method is its easy implementation. To be more specific, independent calculation of measurement errors are not required but incorporated as part of the errors in $\boldsymbol{\tau}_{\text{inp\_1}}$. Furthermore, the variance of the elbow joint model errors with time period t can be obtained

and thus $\boldsymbol{\sigma}^2_{\mathrm{Dyn\_1}}$ is determined.

In order to improve the performance of the proposed method, the P-Value of the elbow joint output errors is to be bigger than 0.05, under which situation the errors are more likely to follow Gaussian distribution. Although the errors show a normal distribution in Fig. 3.2, validation of this conclusion could be conducted. However, in the experiment results not shown, the errors vary as the time period t changes. Therefore, determination of the time period t will affect the distribution of the errors and further affect the CFTE results. More discussion of determining the timer period t can be found in section 4.4.2. and Anderson-Darling test within Minitab is used to analyze the errors.

3.3.3. Analysis of the measurement noise

Again, Anderson-Darling test is employed to analyze the measurement noise and the P-Value of the measurement errors of the elbow joint speed is required to be bigger than 0.05. In that case, it is reasonable to conclude that the measurement noise of the elbow joint speed follows Gaussian distribution. Furthermore, the variance of the elbow joint velocity errors can be obtained and thus $\boldsymbol{\sigma}^2_{\mathrm{mea}}$ is determined.

$\boldsymbol{\sigma}^2_{\mathrm{mea}}$ is a variable since calculation of $\boldsymbol{M}(\boldsymbol{q})$ is based on the pose of the manipulator. Eq. 3-9 is determined by offline experiment in the process of calibration, by which $\boldsymbol{\sigma}^2_{\dot{q}}$ is calculated in real time according to the time-varying joint speed. The covariance matrix of the measurement noise $\boldsymbol{\sigma}^2_{\mathrm{mea}}$ is then updated in each iterative step of the Kalman filter.

It is worth noting that the elbow joint velocity in SD identification experiments (Fig. 3.4) is limited to 0.2 rad/s due to the safety policy of the host institution.

4. DEVELOPMENT AND CALIBRATION OF THE ADAPTIVE KALMAN FILTER

In order to achieve faster estimation response as well as improved estimation accuracy, adaptive Kalman filters are implemented in the control algorithms. This chapter details the development and calibration of the proposed AKF.

4.1. Background and motivation

The Kalman filter is an effective method to realize real-time reduction of the measurement and estimation noise. The adaptive Kalman filter is the most popular in recent years. For example, the variational Bayesian based adaptive Kalman filter (AKF) and suboptimal AKF are proposed in [103], [104], and [105]. These methods perform well in spite of inaccuracies intrinsic within the measurement covariance matrices. For example, Paolo presents a model-based AKF that involves a structure-switching strategy, to realize the sensorless control of a piezo actuator [106] and monitoring of the health information with no physical sensors [107]. The cascaded extended AKF was utilized to estimate the immeasurable states of the piezo actuator [108]. In order to estimate the real-time state of the power system, an error-prediction AKF with step-varying processes [109] and a two-stage AKF [110] were utilized, respectively. The two-stage AKF can also be employed [111] as a disturbance estimator in automotive applications. In order to enhance filter accuracy, the Sage-Husa AKF can be employed to estimate the statistical characteristics of the noise [112]. The constrained adaptive robust integration Kalman filter is used to realize a reliable and precise navigation solution [113]. In this navigation solution, the raw observations from the heterogeneous sensors are corrected by the pseudo observations derived from state equality constraint. A computationally efficient version of the variational adaptive Kalman filter is proposed to solve the filtering problem of transfer alignment with an inaccurate measurement noise covariance matrix [114]. An unscented AKF is presented in [115] to track sudden changes in stiffness of structural systems exposed to earthquake induced excitations. Variations of the AKF have been applied to vehicle navigation [116], [117], UAV control [118], robot operation [119]-[121] and battery state detection [122].

In [95], a Kalman filter was introduced to achieve force/torque estimation with empirical parameters used as Kalman filter gains. It is worth noting that although the method using empirical parameters worked effectively (better estimation performance is achieved compared to typical methods, e.g. nonlinear disturbance observer and generalized-momentum observer) and saves time (offline calibration experiments are not required), it is not generalised as the approach ignores the characteristics of the individual manipulator and uses uniform gains. Consequently, this thesis describes a new scientific goal of improving the estimation performance of the external wrench. This goal is achieved by exploring the potential uncertainty of the manipulator dynamics and system measurement (as discussed in section 3.2.3. and 3.2.4.).

A Kalman filter tuning method is presented in [96]. In this paper, uncertainty of robotic dynamics is captured. For

example, the errors in the friction model are assumed as the dominant part of $\boldsymbol{\tau_{inp}}$. However, this research using a UR5 showed that the fluctuations in current lead to more noise than the friction model does. This inspired us to take the errors from measured current into account. Intuitively, filtering the noisy current would help to improve estimation accuracy. However, time lag is ubiquitous with all the real-time moving averages. Thus, response speed and estimation accuracy can trade off. In order to solve this problem, one of the main contributions in this research, a mode-switching moving average (MSMA), is proposed. The improvement of the MSMA includes, but is not limited to, filtering the measured joint current. More intrinsically, the MSMA depends on the fact that smaller diagonal elements in the covariance matrix lead to faster CKF responses [96] and thus the optimal balance between response time and accuracy can be maintained. Ultimately, the approach is intended to allow more accurate estimation and faster response concurrently. Fig. 4.1 better displays the process of the mode-switching moving average.

In this research, information of current noise and dynamics uncertainty is employed to calibrate the AFK, due to which the AKF works faster and more precisely in contact estimation compared to peer methods [95] and [96]. Table 4-1 highlights the distinction of the proposed method to existing approaches.

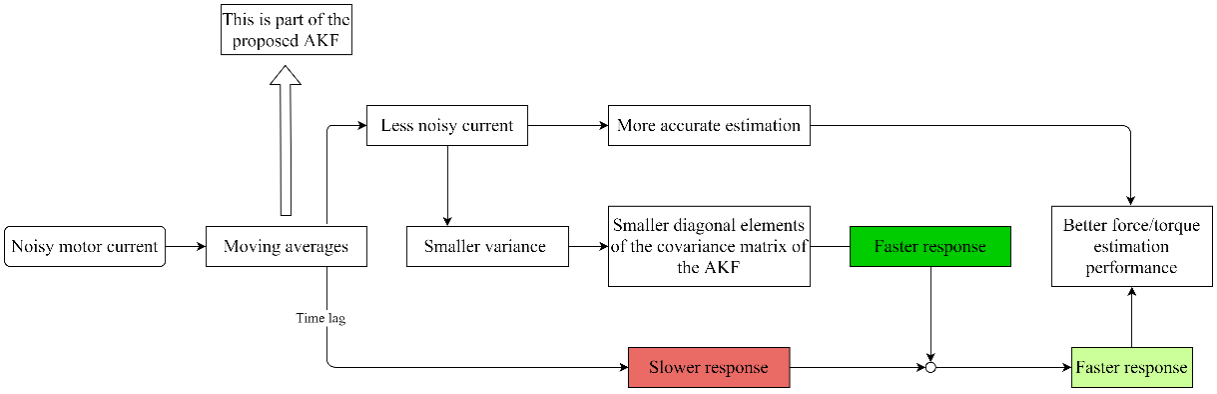

Fig. 4.1. Inner contribution of the proposed MSMA.

Table 4-1 A summary of different methods applied in this work and previous papers.

	Method in [47]	Method in [48]	Proposed method
Is the generalized-momentum-based model used?	Yes	Yes	Yes
Are the external force/torque sensors used when modelling the robot?	Yes	Yes	No
Is the classical Kalman filter involved?	Yes	Yes	Yes
Is the Kalman filter tuned?	No	Yes	Yes
Is the motor current used?	Yes	Yes	Yes
Is the motor current noise addressed?	No	No	Yes
Is the friction model errors considered?	No	Yes	Yes
Is the disturbance Kalman filter adaptive?	No	No	Yes
Is the mode-switching moving average involved and calibrated?	N/A	N/A	Yes

4.2. AKF based on WMA

The first AKF developed uses the WMA to filter the current. Structures of the WMA and the corresponding AKF are introduced in the following parts.

4.2.1. Weighted Moving Average with variable span

In contrast to the CKF that directly utilizes the measured current, the measured signal is regulated by the pre-filter with variable time period first and then used to enable estimation of the contact force and torque with the CKF. In this research, a single moving average is used as the pre-filter first. In [123], the Weighted Moving Average with variable span is proposed (as shown in Fig. 4.2) in order to smooth the currents.

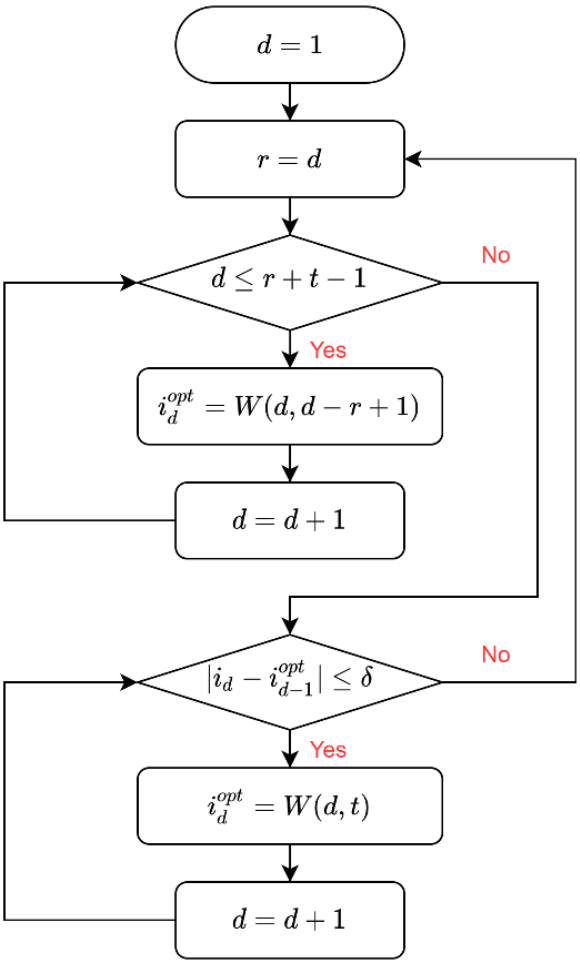

Fig. 4.2. The Weighted Moving Average based on variable span.

where r and d denote the step times. i_d is the measured current at step time d. t is the number of the samples which are averaged in each step. Detail of how t is determined is described in the following section. i_d^{opt} stands for the filtered current at step time d. δ is an experimentally determined parameter which is used to decide whether the span varies or not. $W(d, t)$ is the Weighted Moving Average and is calculated by

$$W(d,t) = 2[i_d t + i_{d-1}(t-1) + \cdots + i_{d-1+1}]/[t(t+1)] \quad 4\text{-}1$$

In this research, it is assumed that the time gap between any two sudden changes in the exerted external wrench is larger than $t_s \cdot t$.

Implementation of the WMA with variable span is as follows:

Step 1. At time step $d(1 \leq d < t)$, d samples (i_d included) before i_d are averaged to get the optimal option $i_d^{opt} = W(d, d)$ (as shown in Fig. 4.3).

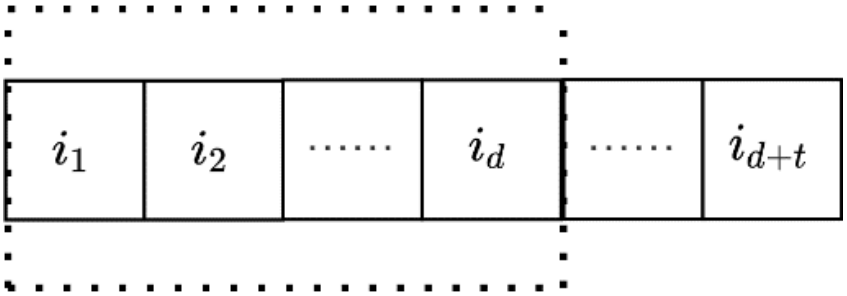

Fig. 4.3. d samples up to i_d are shown in the dotted rectangle.

Step 2. At time step $d(t \leq d)$, t samples (i_d included) before i_d are averaged to get the optimal option $i_d^{opt} = W(d,t)$. At the same time, i_{d+1} is checked to make sure whether external force occurs (as shown in Fig. 4.4). If external force is detected, go to Step 3, otherwise i_{d+1}^{opt} is calculated in a similar manner to Step 2.

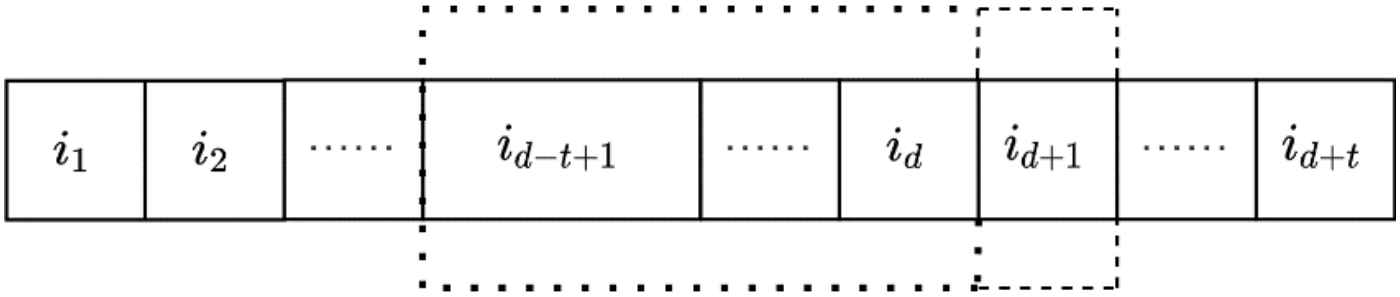

Fig. 4.4. t samples up to i_d are shown in the dotted-line rectangle. i_{d+1} in the dashed-line rectangle is checked.

Step 3. In case of dramatic change in the external wrench or joint acceleration at time step $d+1$, a sudden rise or drop will occur in the current. If the change between the present current i_{d+1} and the previous currents i_d^{opt} exceeds δ, an external wrench is assumed. Hence, from time step $d+1$ to time step $d+t$, b samples (i_{d+b} included, $1 \leq d < t$) before i_{d+b} are averaged to get the optimal option $i_{d+b}^{opt} = W(d+b,b)$ (as shown in Fig. 4.5).

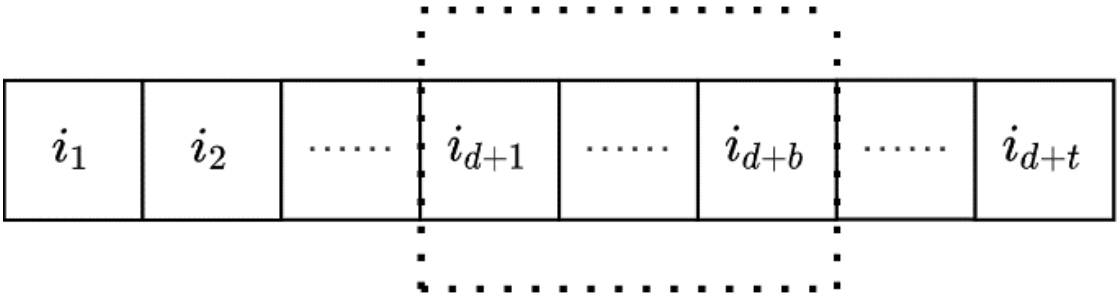

Fig. 4.5. b samples up to i_{d+b} are shown in the dotted-line rectangle.

Step 4. At time step $d+t$, the filter goes back to Step 2. $i_{d+t}^{opt} = W(d+t,t)$ is calculated and verification of i_{d+t+1} is performed (as shown in Fig. *4.6*).

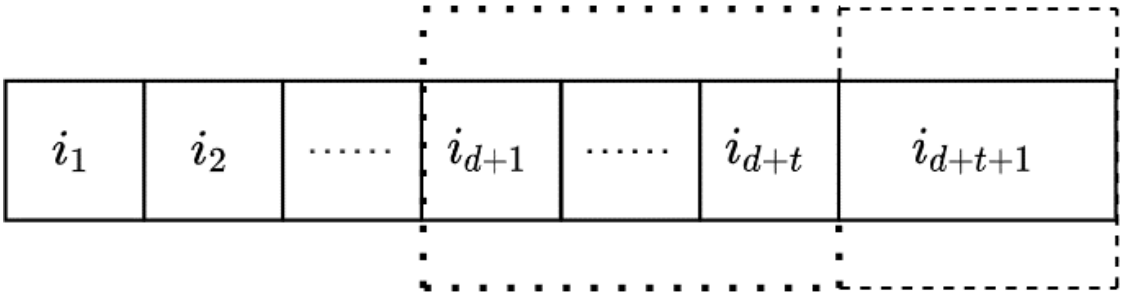

Fig. 4.6. t samples up to i_{d+t} are in the dotted-line rectangle. i_{d+t+1} in the dashed-line rectangle is checked.

4.2.2. AKF based on the WMA with variable span

With the Weighted Moving Average based on variable span, the proposed adaptive Kalman filter is introduced, which is displayed in Fig. 4.7. When the AKF starts to work, the motor current is measured and used to determine whether there was sudden pendulation, which can be assumed to be an external wrench exerted on the UR5. If there is sudden external wrench detected, the measured current will be filtered by the WMA with variable span; if not, the current will be filtered by the WMA with fixed span. The function of the variable span can facilitate a fast response of the contact estimation. As shown in Fig. 4.7, the SKF is calibrated based on the parameters obtained from measured motor current and measured joint speed. The filtered current is transferred to joint output torque and then the external wrench is calculated using the dynamic model of the UR5 and the environment.

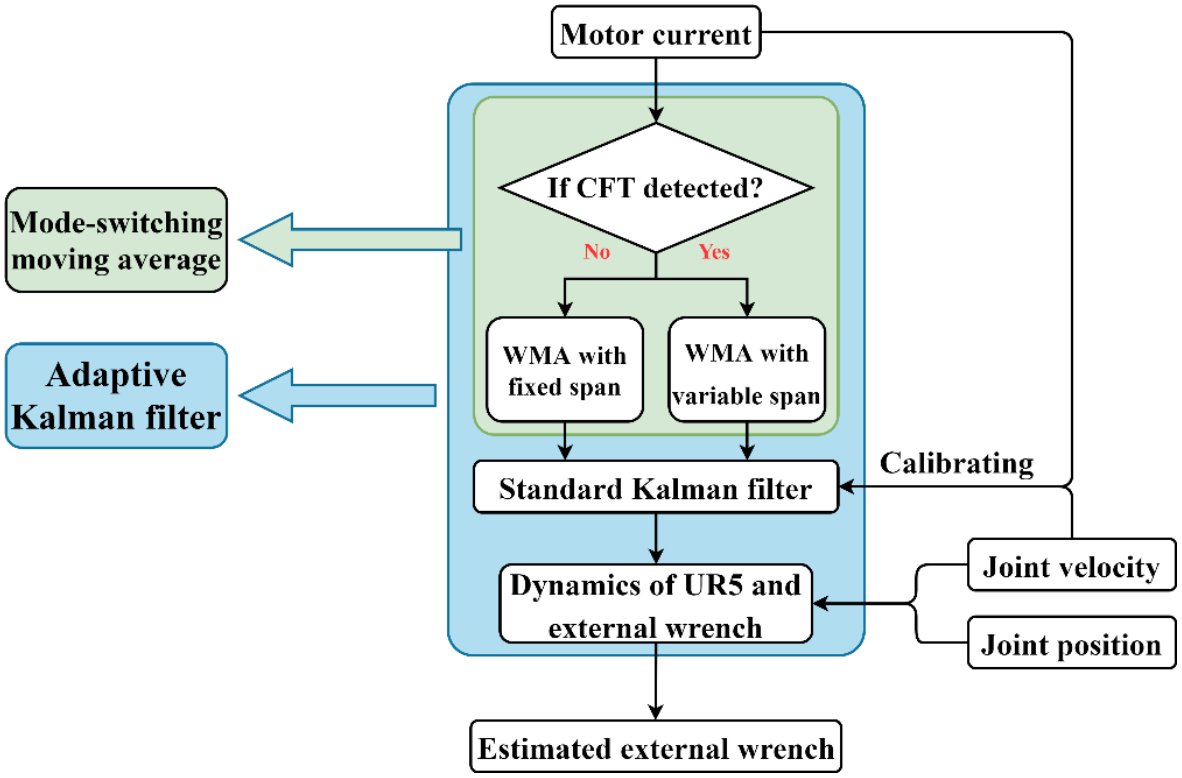

Fig. 4.7. Adaptive Kalman filter based on the WMA with variable span.

4.3. AKF based on MSMA

Although the WMA with variable span in [123] works well in external contact estimation, individual moving averages have specific advantages in different periods during external wrench estimation. Therefore, a mode-switching moving average is designed to optimize performance across multiple scenarios.

4.3.1. Determination of the moving averages

The most common moving averages are considered to build the MSMA: the Simple Moving Average (SMA), the Exponential Moving Average (EMA), the Weighted Moving Average (WMA), and the Hull Moving Average (HMA).

Firstly, the SMA was discounted since it overemphasizes the past samples in comparison to more recent samples, and this leads to poor performance in terms of respond time, especially when dealing with varying external contact. Secondly, as discussed in section 6, the smoothing effect of the HMA is better than that of the WMA when the time period is fixed and large. Conversely, the performance of the WMA is better in terms of reducing estimation errors and response time. Advantages of both moving average approaches are adopted in this research. The difference in the performance of WMA and EMA is negligible when the time period is small and varying and the weight coefficients for both averages are appropriately chosen. Thus, the approach can use a combination of the HMA (when the time period is large and fixed) and the EMA (when the time period is small and varying). However, it should be noted that the WMA is utilized when calculating the HMA (Eq. 4-1 and Eq. 4-2). This leads a less burdensome calculation in the proposed method. Specifically, calculation of the WMA is still required if the combination of the HMA and the EMA is employed.

4.3.2. Mode-switching moving average

The schematic of the mode-switching moving average based on variable time period for the single-arm robot is displayed in Fig. 4.8.

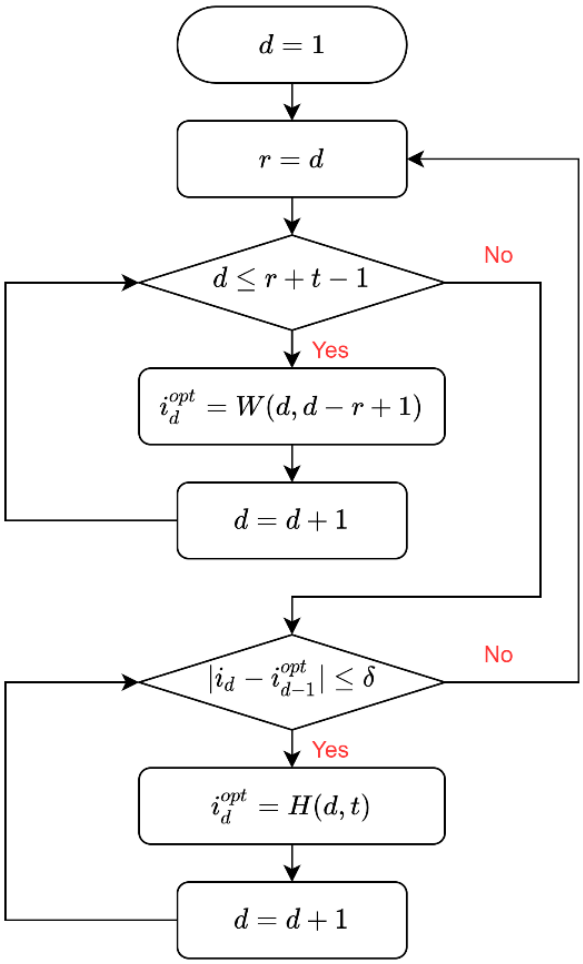

Fig. 4.8. Mode-switching filter based on variable time period for the single-arm robot.

where t denotes the time period, d is the step time, $\boldsymbol{i}_d^{opt}$ stands for the filtered current at step time d, δ is a experimentally determined parameter that determines whether the time period should be varied. $W(d,t)$ is the Weighted Moving Average. $H(d,t)$ is the Hull Moving Average, and the closing current is obtained by

$$H(d,t) = W\left\{\{2W[d, \text{int}(t/2)] - W(d,t)\}, \text{int}\left(\sqrt{t}\right)\right\} \quad 4\text{-}2$$

It is to be noted that the Mode-switching filter employed for the CFTE of dual-arm robot is different from that used for the single-arm robot. To be more specific, the HMA is employed at the start of the CFTE and during the period when the span is varying. Conversely, the WMA is used when the span is fixed. The mode-switching filter for the dual-arm system is displayed in Fig. 4.9.

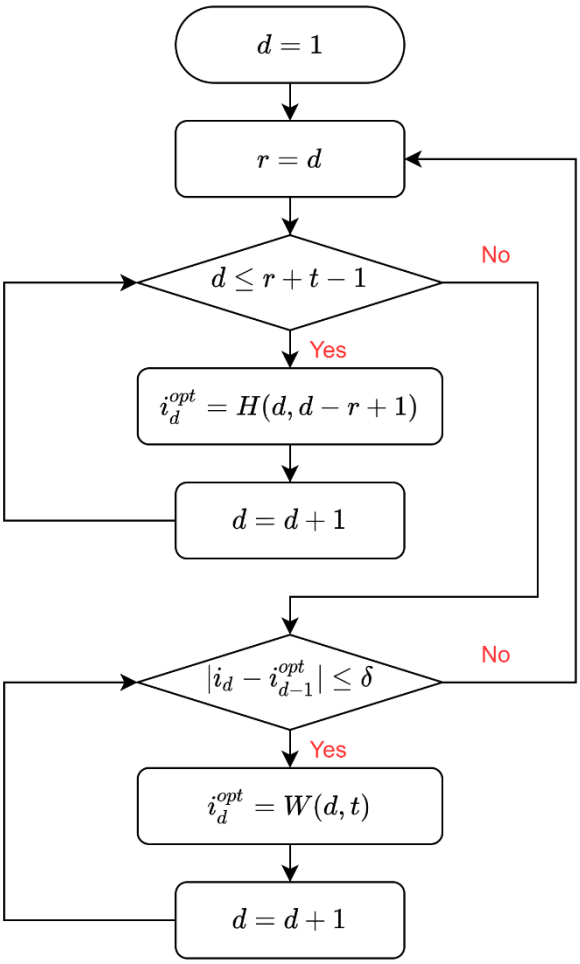

Fig. 4.9. Mode-switching filter based on variable time period for the dual-arm robot.

4.3.3. AFK based on the MSMA with variable span

With the MSMA based on variable span, a more powerful adaptive Kalman filter is introduced, and it is displayed in Fig. 4.7. When the AKF starts to work, the motor current is measured and used to determine whether there is sudden pendulation, which can allow assumption of an external wrench exerted on the UR5. When the proposed AKF is activated, the time period is allowed to vary from 1 to t. Then the measured current sample is compared to the previous current sample. If δ is larger than the magnitude of the gap, an external wrench is assumed to be exerted on the UR5 and the measured current will consequently be filtered by the WMA with variable span, which varies from 1 to t again; if not, the current will be filtered by the WMA with fixed span at t. With the filtered current, joint output torque is obtained and then the external wrench is calculated using the dynamic model of the UR5 and the environment. As shown in Fig. 4.10, tuning the threshold value δ will be talked about in the next section.

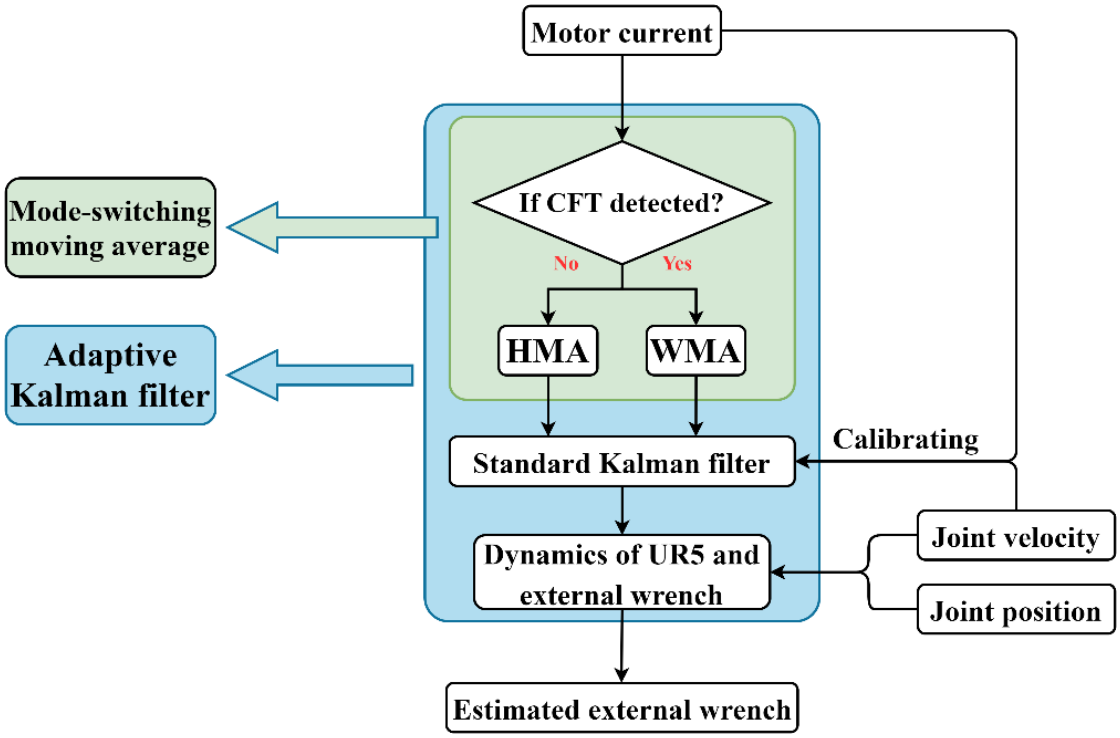

Fig. 4.10. Adaptive Kalman filter based on the MSMA with variable span for the single-arm robot.

As discussed in section 4.3.2. , the mode-switching filters employed for dual-arm robot is different from that used for the single-arm robot. Therefore, the AKF used for the dual-arm robot also differs from that of the single-arm robot and it is displayed in Fig. 4.11.

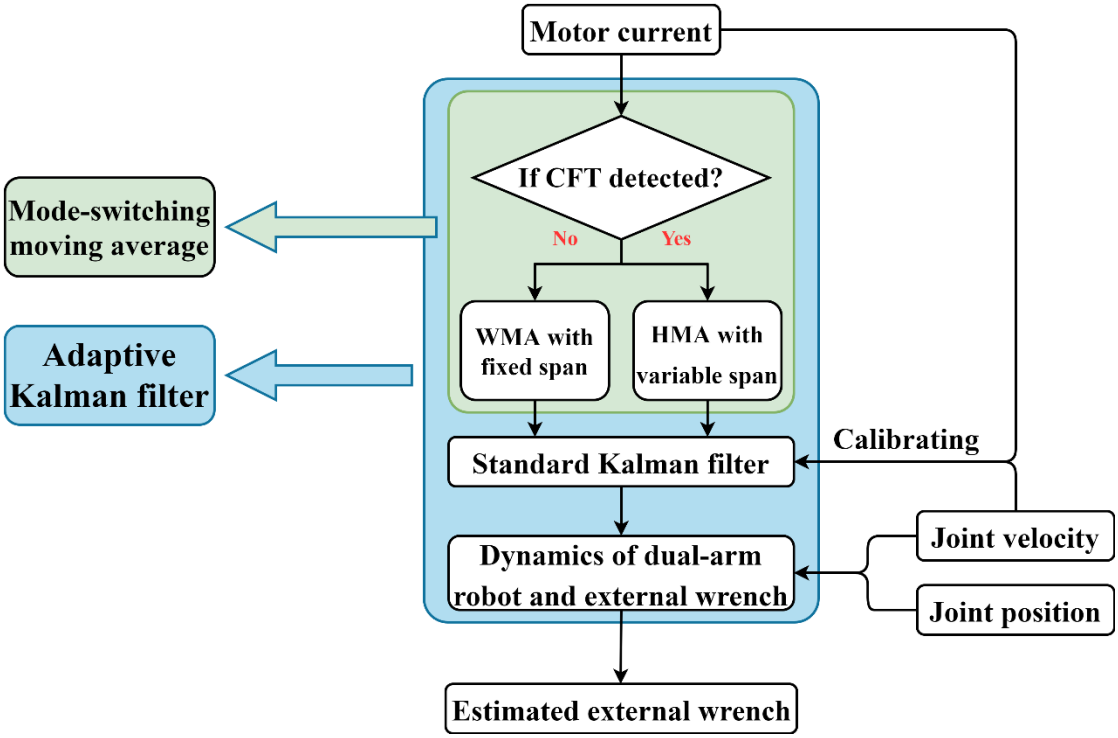

Fig. 4.11. Adaptive Kalman filter based on the MSMA with variable span for the dual-arm robot.

4.4. Calibration of the pre-filter

In order to apply the proposed AKF, another scientific challenge of exploring new tuning strategies for the mode-switching moving average must be met. To be more specific, by balancing time lags and the smoothing effect, the optimal time periods of individual moving averages are determined. Furthermore, appropriate threshold values must be decided considering the characteristics of the motor currents.

4.4.1. Threshold value of pre-filter

In order to obtain a value for δ, the elbow joint was commanded to move from position of 1.48 rad to position of 1.52 rad at constant speed of 0.01 rad/s. During this motion, the motor current is observed in Fig. 4.12.

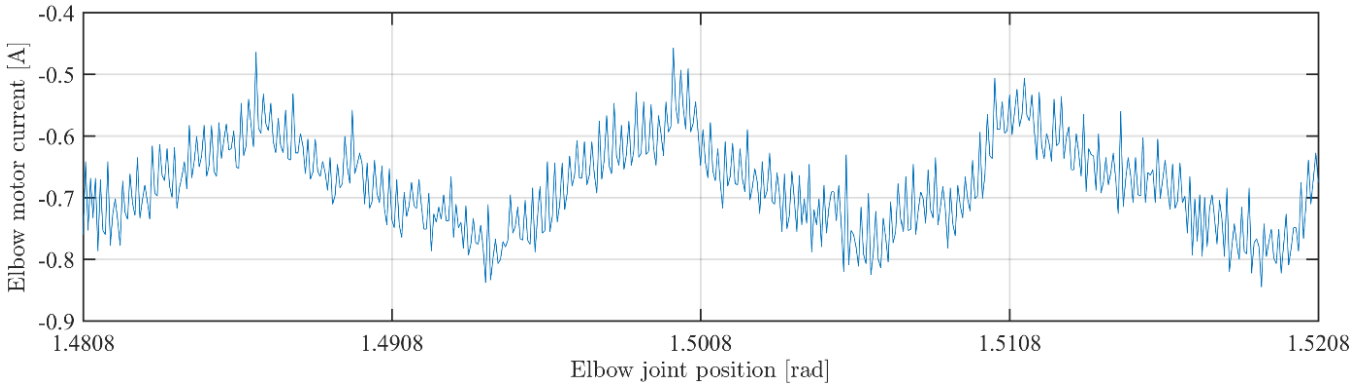

Fig. 4.12. Recorded motor current of the elbow joint varies as the joint position changes.

As shown in Fig. 4.12, the current fluctuated approximately 0.3 A (-0.8 to -0.5 A) without external payload. Consequently, the motor output can be reasonably approximated as constant, with an effective current of -0.65 A. Thus, δ was set to half the amplitude $0.3/2 = 0.15$. Beyond this threshold, the algorithm assumes an external wrench has been applied to the robot and the mode then switched.

4.4.2. Time period of the pre-filter

It is assumed that larger t values would lead to less noisy filtered current signals. Consequently, the response of the external force/torque estimation will be more precise, and thus quicker convergence is potentially achieved. However, excessive samples in each averaging step increase the time lag, and weaken the trends in the smoothed motor current signal. Hence, the variance decreases as t increases. However, beyond approximately $t = 50$, the variance in the driving torque errors plateaus as the smoothing benefits are cancelled by the latency of the system (Fig. 4.13). Furthermore, at high values of t, missed dynamics contribute to the errors observed by the estimator. In contrast, at low values, measurement errors from the sensor contribute more significantly to the errors observed by the estimator. Hence, while low values of t yield measurement error signals, larger values of t tend to lead to non-measurement ones. The span of the elbow joint using

HMA is determined and the value can be any integer between 45 and 55 (as shown in Fig. 4.13).

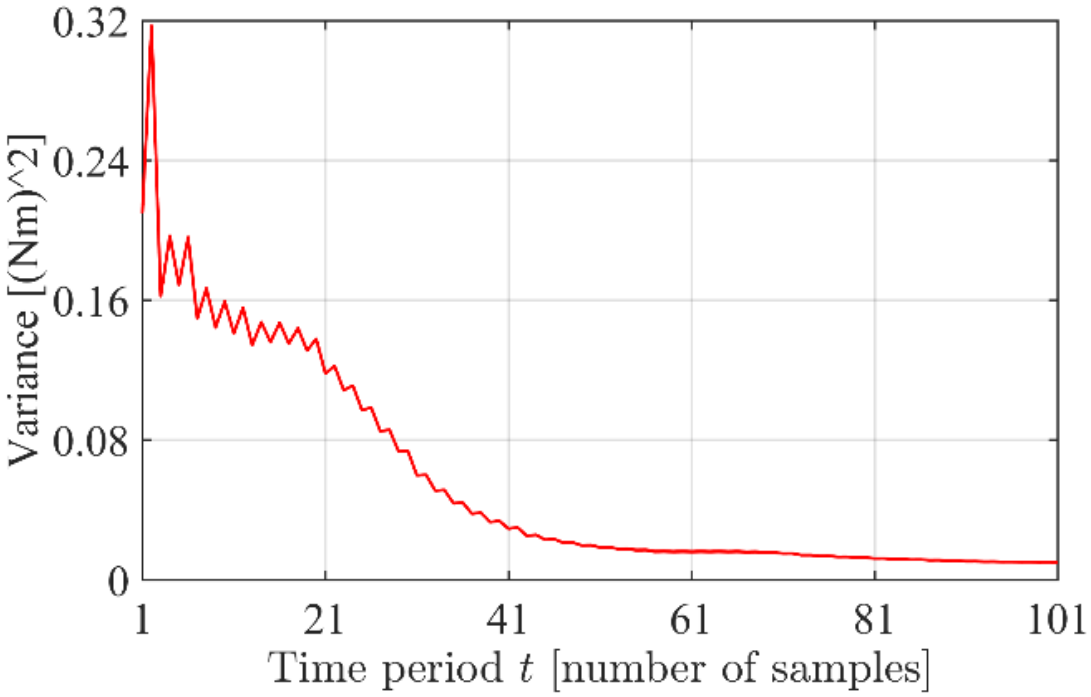

Fig. 4.13. The variance of the predicted state noise $\boldsymbol{e}_p$ with different time periods

However, an approximate estimation of the time period is not sufficiently enough for proposed approach. Consequently, determination of the optimal time period implementation is further researched. It is to be noted that the standard Kalman filter is proficient at dealing with Gaussian noise, and thus keeping the predicted state noise within Gaussian distribution will be one of requirements while choosing the optimal time period. In [123], the WMA is employed as the pre-filter. The variance of the predicted state noise is displayed in Fig. 4.14. Similarly, a greater number of samples in each averaging step will lead to a lower noise contribution in the current signal. However, excessive samples in each step will weaken the trends in the smoothed motor current signal because the actual current is changing all the time. Hence, the variance initially decreases as t increases. After that, the variance in the joint output torque errors plateaus as the smoothing benefits are cancelled by the latency of the system. Worse yet, excessive examples in each averaging step can lead to new errors that are not Gaussian. In that case, the largest span ($t = 19$) for which the noise in the elbow joint is still normally distributed is determined and the related variance is obtained.

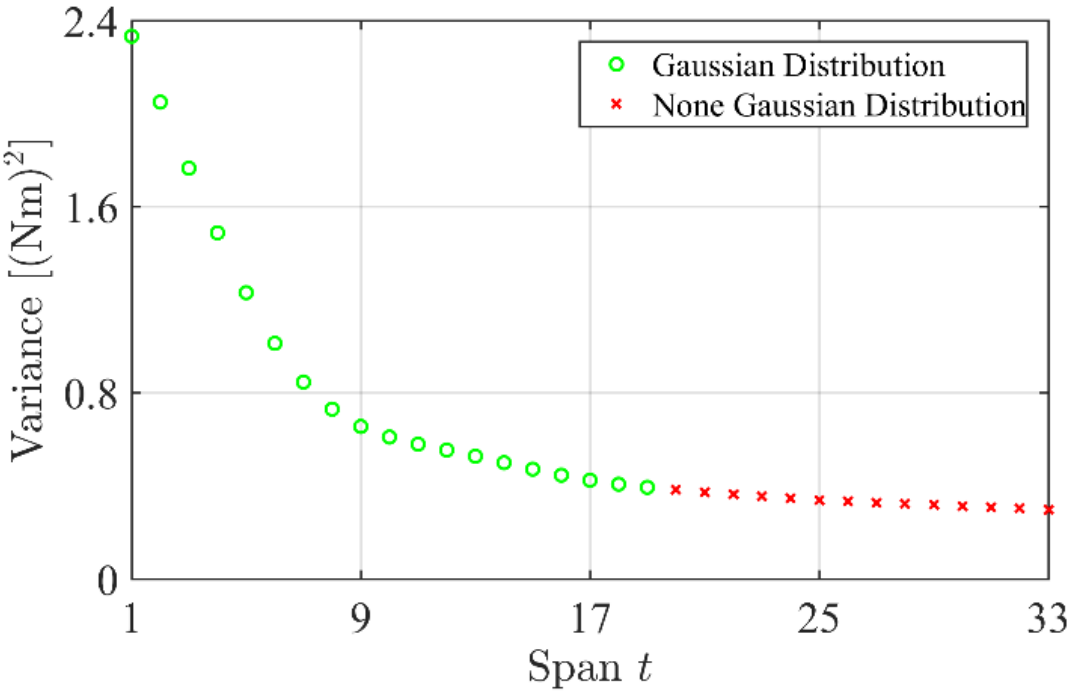

Fig. 4.14. The variance of the predicted state noise $\boldsymbol{e}_p$ with different spans. The green circles indicate noise which is normally distributed. The red crosses denote the noise that does not follow normal distribution.

5. CFTE OF THE SINGLE-ARM ROBOT WITH THE AKF BASED ON WMA

In this chapter, the effectiveness of the proposed CFTE method based on the WMA with variable time period is demonstrated in UR5 manipulator experiments. In section 5.1.1. , the algorithms used in this chapter are presented. In sections 5.1.2. to 5.1.4. , the CFTE experiments with different configurations are described and the results are presented. In section 5.1.5. the performance of the experiments is discussed.

An end-effector was prepared and rigidly attached to the manipulator by pneumatic power (Fig. 5.1(a)). The contact surface between the pneumatic end effector and the payload is horizontal. The end effector was commanded to move vertically at uniform speed during the experiment. Therefore, the exerted force on the manipulator from the payload can be precisely known. The contact torque can also be calculated as both the contact force and the distance between the TCP and the contact force are available.

At the start of motion, acceleration cannot be avoided. Therefore, the trajectory of end effector must be specifically designed in order to obtain a motion at uniform speed when the payload is engaged by the manipulator. In the following experiment, the speed of the end-effector is set at 0.06 m/s and the acceleration is set at 0.24 m/s^2.

The effectiveness of the proposed CFTE method is demonstrated at constant speed with varying payload. External wrench is exerted on the UR5, which includes three steps:

Step 1. The robot is moved to an initial position with a gripper attached to the end effector (Fig. 5.1(a)). After initialization, the TCP is programmed to move up vertically at constant speed. The payload (lead filled cup in Fig. 5.1) is initially not engaged by the gripper. The effect of gripper on the TCP can be deemed as a constant force of 17.09 N in the $-Z0$ direction and a constant torque in the $X0$ direction.

Step 2. The payload is engaged by the moving gripper, as shown in Fig. 5.1(b). The model has no *a priori* information to anticipate coupling with the payload.

Step 3. The payload and gripper are coupled and raised together (Fig. 5.1(c)). The effect of the payload and the gripper can be regarded as a constant force in the $-Z0$ direction and a constant torque in the $X0$ direction.

During the experiment, the joint kinematic information and motor current are recorded with a sampling frequency of 125 Hz.

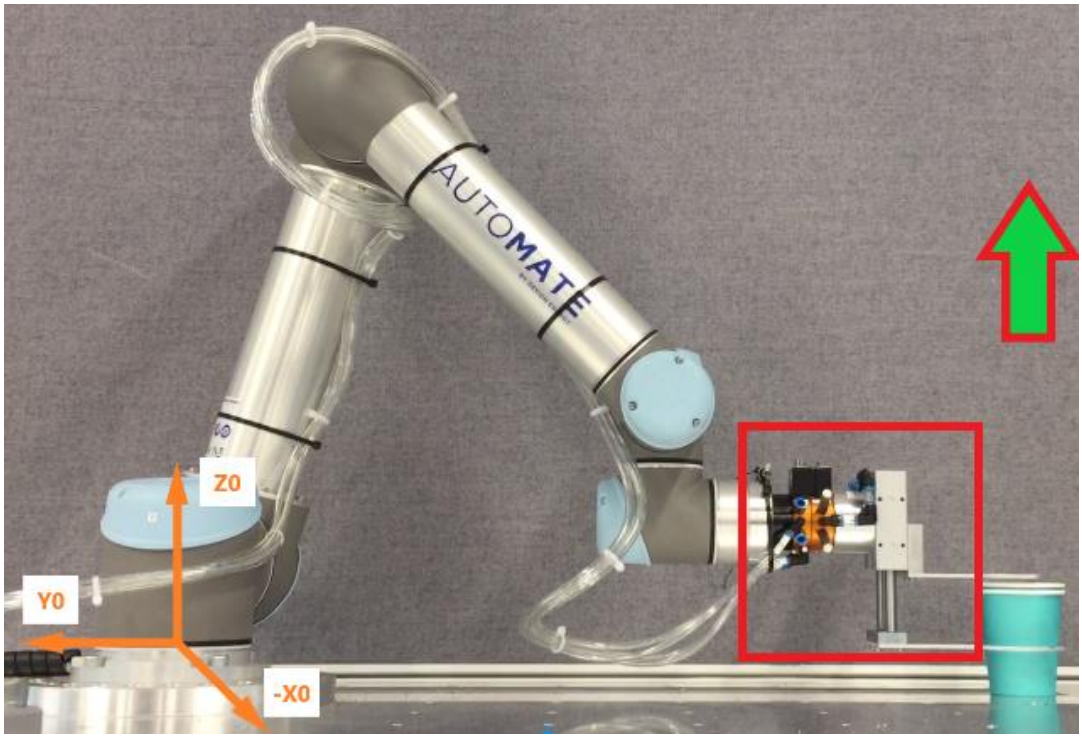

(a) Initial pose. The gripper in the red square weighs 1.742 kg. The TCP raises at constant velocity of 0.06m/s and the payload is stationary.

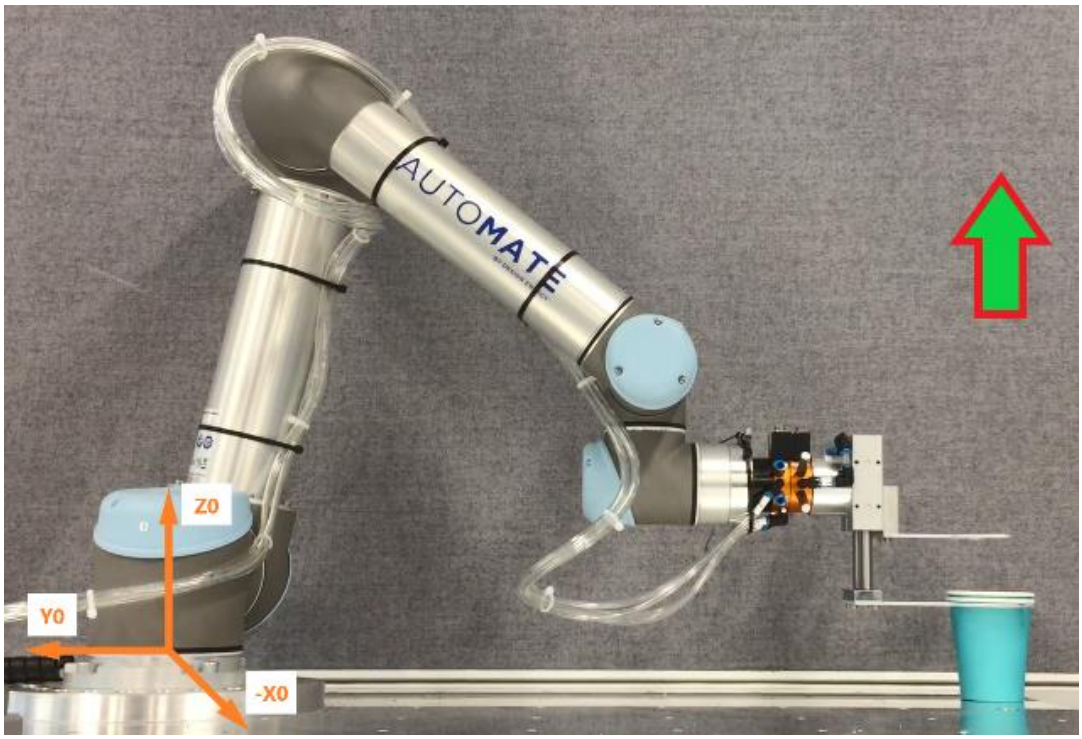

(b) The payload starts to move up vertically due to the contact with the gripper.

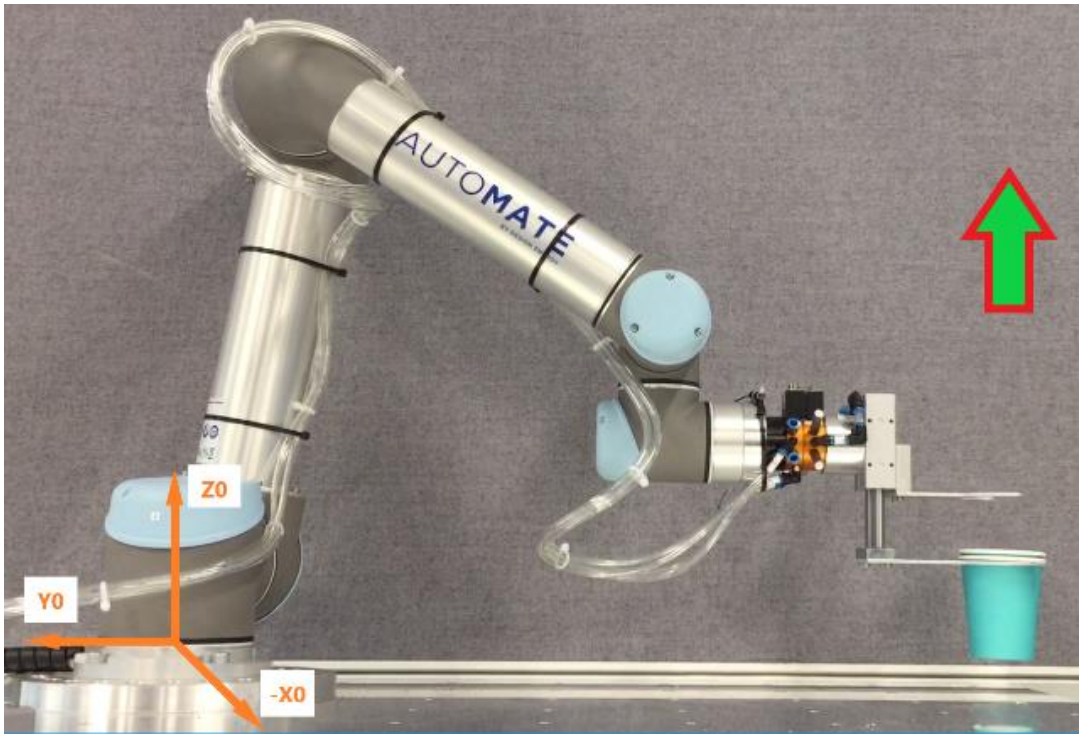

(c) The manipulator moves up at constant speed as the TCP does.

Fig. 5.1. Demonstration scenario for the experiment. The UR5 manipulator is initialized as (a). The TCP is commanded to move up vertically and the effect of the cup filled with lead can be regarded as constant external wrench exerted on the TCP.

5.1.1. Codes used in the experiments

The algorithms used in this experiment are displayed in Fig. 5.2. The codes used for communication between the computer and the UR5 are stored in ".py" files (Fig. 5.2 yellow). When the experiment starts, the data read and storage commands are sent from the computer to the UR5 by "realtimeclient.py" (Appendix A1) and "jointqqdidirecord.py" (Appendix A2). The UR5 movement commands are sent by "UR5.py" (Appendix A3) and "experiment.py" (Appendix A4).

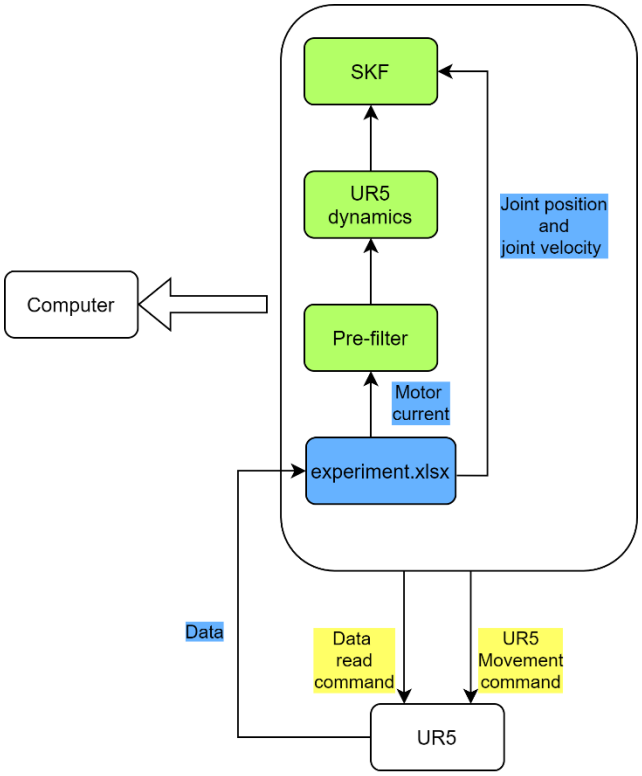

Fig. 5.2. Scripts used in the experiment.

The data generated by the UR5 is stored and transferred in "experiment.xlsx" files (blue background in Fig. 5.2). The time and data is stored in Column A and Column B (Fig. 5.3). Measured position of individual joints is stored in Column C-H (Fig. 5.3). Measured velocity of individual joints is stored in Column I-N (Fig. 5.3). Measured motor current of individual joins is stored Column O-T (Fig. 5.3).

A	B	C	D	E	F	G	H	I	J	K	L	M	N	O	P	Q	R	S	T
16340.44	!!!!2020-0	1.570753	-0.81035	1.214606	-0.40413	1.570791	-3.83972	0	-0.06048	-0.0602	0.118476	0	0	-0.15693	-5.19427	-3.01748	-0.16318	0.260782	0.022876
16340.45	!!!!2020-0	1.570776	-0.81083	1.214114	-0.40321	1.570815	-3.83971	0	-0.06266	-0.06269	0.123629	0	0	-0.20176	-5.08891	-2.95022	-0.17538	0.164704	0.024401
16340.46	!!!!2020-0	1.570765	-0.81133	1.21361	-0.4022	1.570887	-3.83972	0	-0.06117	-0.06045	0.119243	0.030152	0	-0.18383	-4.85128	-2.89194	-0.08083	0.019826	0.022876
16340.46	!!!!2020-0	1.570753	-0.81189	1.213095	-0.40127	1.570958	-3.83971	0	-0.06131	-0.06113	0.120873	-0.01438	0	-0.19055	-4.68538	-2.86952	-0.07778	-0.04423	0.027451
16340.47	!!!!2020-0	1.570776	-0.8123	1.212591	-0.40033	1.570935	-3.83969	0	-0.0589	-0.06237	0.118452	0.029361	0	-0.16141	-4.71453	-2.81347	-0.06558	0.080827	0.022876
16340.48	!!!!2020-0	1.570789	-0.81285	1.212051	-0.39936	1.570994	-3.83971	0	-0.05741	-0.06307	0.121376	-0.0214	0	-0.1771	-4.85576	-2.75743	-0.07625	-0.02135	0.024401
16340.49	!!!!2020-0	1.570776	-0.81327	1.211547	-0.39835	1.571066	-3.83971	0	-0.05814	-0.06292	0.117062	0.029529	0	-0.1233	-4.95664	-2.69017	-0.09455	0.036601	0.021351
16340.5	!!!!2020-0	1.570717	-0.81373	1.21108	-0.39736	1.570971	-3.83975	0	-0.05659	-0.06205	0.121544	-0.03238	0	-0.1771	-5.12702	-2.6969	-0.1098	0.126578	0.025926
16340.5	!!!!2020-0	1.570801	-0.81417	1.210564	-0.3963	1.571102	-3.83975	0	-0.05524	-0.06205	0.122383	0.031926	0	-0.13899	-5.23463	-2.67672	-0.16775	-0.08845	0.024401
16340.51	!!!!2020-0	1.570789	-0.81459	1.21006	-0.39526	1.570958	-3.83972	0	-0.054	-0.06173	0.120178	-0.02591	0	-0.17486	-5.36914	-2.69914	-0.1281	0.163179	0.036601
16340.52	!!!!2020-0	1.570776	-0.81502	1.20958	-0.39427	1.571054	-3.83971	0	-0.05527	-0.06277	0.119123	0.028594	0	-0.12106	-5.38259	-2.73053	-0.15403	-0.08845	0.036601
16340.53	!!!!2020-0	1.570741	-0.81549	1.209077	-0.39337	1.570958	-3.83972	0	-0.05626	-0.06321	0.117541	-0.02965	0	-0.17486	-5.36241	-2.73501	-0.12658	0.18758	0.038126
16340.54	!!!!2020-0	1.570801	-0.81598	1.208573	-0.3924	1.57109	-3.83972	0	-0.05662	-0.06277	0.118644	0.025574	0	-0.16141	-5.32654	-2.72156	-0.1708	-0.24248	0.033551
16340.54	!!!!2020-0	1.570801	-0.81641	1.208022	-0.39145	1.570923	-3.83972	0	-0.05731	-0.06463	0.11735	-0.00992	0	-0.16589	-5.20997	-2.65879	-0.19216	0.364485	0.032026
16340.55	!!!!2020-0	1.570753	-0.81691	1.207518	-0.3905	1.571138	-3.83971	0	-0.05708	-0.0634	0.119171	0.018504	0	-0.17038	-5.18979	-2.68569	-0.20588	-0.25468	0.054901
16340.56	!!!!2020-0	1.570765	-0.81731	1.20705	-0.38961	1.570911	-3.83965	0	-0.05825	-0.06317	0.118955	-0.00937	0	-0.16589	-5.04632	-2.59826	-0.19673	0.306533	0.053376
16340.57	!!!!2020-0	1.570776	-0.81782	1.206522	-0.38863	1.571066	-3.8397	0	-0.05806	-0.06315	0.117038	-0.00388	0	-0.13675	-5.08891	-2.62068	-0.14793	-0.24858	0.056427
16340.58	!!!!2020-0	1.570776	-0.81828	1.206031	-0.38771	1.570971	-3.83972	0	-0.05905	-0.06225	0.115432	-0.01074	0	-0.16141	-5.13375	-2.68121	-0.13573	0.308058	0.071677

Fig. 5.3. "experiment.xlsx" files

With "experiment.xlsx" files, the measured motor current is averaged by the WMA with variable span (Appendix B2). The filtering effect of WMA on the elbow joint is displayed in Fig. 5.4. The pre-filter is modelled in Matlab and stored in ".m" files (Fig. 5.2 green).

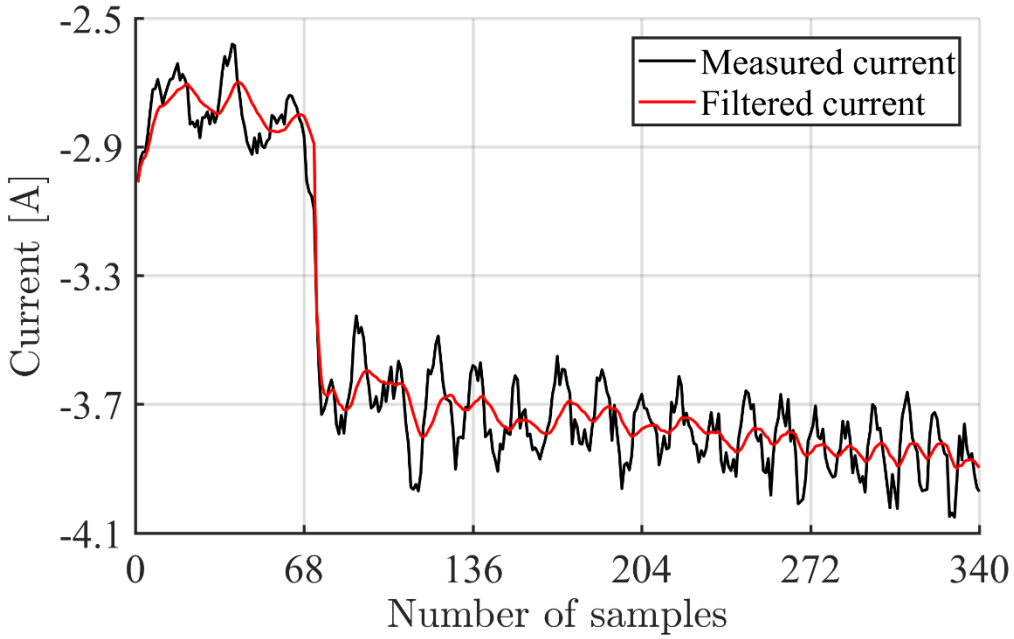

Fig. 5.4. Filtering effect of the WMA with variable time period.

Then, the filtered current is used to calculating the joint driving torque by Eq. 3-1. With the joint driving torque, all the parameters in Eq. 2-23 are obtained except for the external wrench. UR5 dynamics is then modelled in Matlab using the following 5 files (Fig. 5.5), and it is stored in ".m" files (Fig. 5.2 green). It is worth noting that "UR5dynamics.m" (Appendix B1) is the main file, and the others are its clients. "Coriolis.m" (Appendix B3) is used to model the Coriolis and centrifugal effect. However, in order to reduce calculation burden caused by "Coriolis.m", the Christoffel symbols of the first kind is introduced [90]. As the subroutine of "Coriolis.m", the file "christoffel.m" (Appendix B4) calculates the term c_{ijk} in Eq. 2-35. The effect of the manipulator gravity is modelled by "gravity.m" (Appendix B5). The homogeneous transformation (Eq. 2-3) is calculated by "Trans.m" (Appendix B6).

Name	Date modified	Type	Size
christoffel.m	7/16/2019 6:03 PM	MATLAB Code	1 KB
Coriolis.m	7/16/2019 6:23 PM	MATLAB Code	1 KB
gravity.m	7/16/2019 6:07 PM	MATLAB Code	1 KB
Trans.m	2/26/2019 11:43 AM	MATLAB Code	1 KB
UR5dynamics.m	7/26/2020 7:43 PM	MATLAB Code	7 KB

Fig. 5.5. The Matlab codes used for modelling the manipulator dynamics.

5.1.2. CFTE at constant speed with varying payload

In this experiment, the TCP goes up at the speed of 0.06 m/s, and the experiment is repeated with payloads of 400 g to 900 g with increments of 100 g and from 1000 g to 2000 g with increments of 200 g.

Fig. 5.6 shows the force estimation performance with the SKF presented in [96] and the proposed estimation approach of the standard Kalman filter based on the Weighted Moving Average with variable span (SKFW). The torque estimation results are displayed in Fig. 5.7.

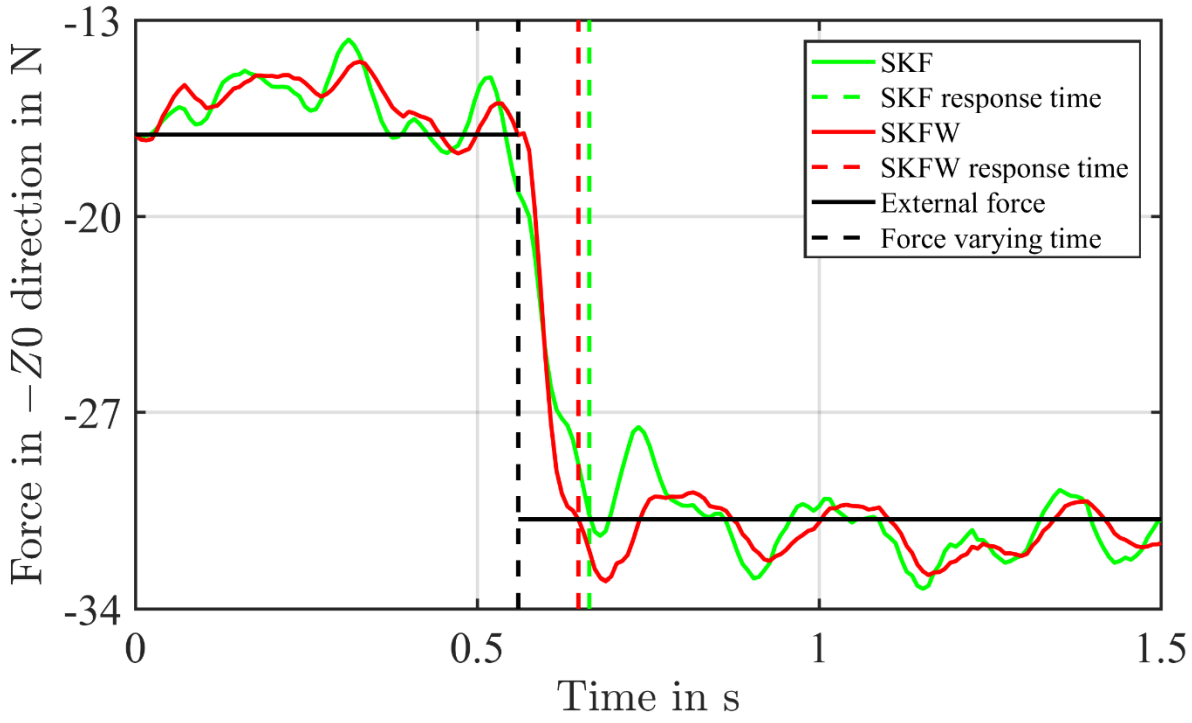

Fig. 5.6. Estimation of contact force (with 1400 g lead inside the cup) in the $-Z0$ direction.

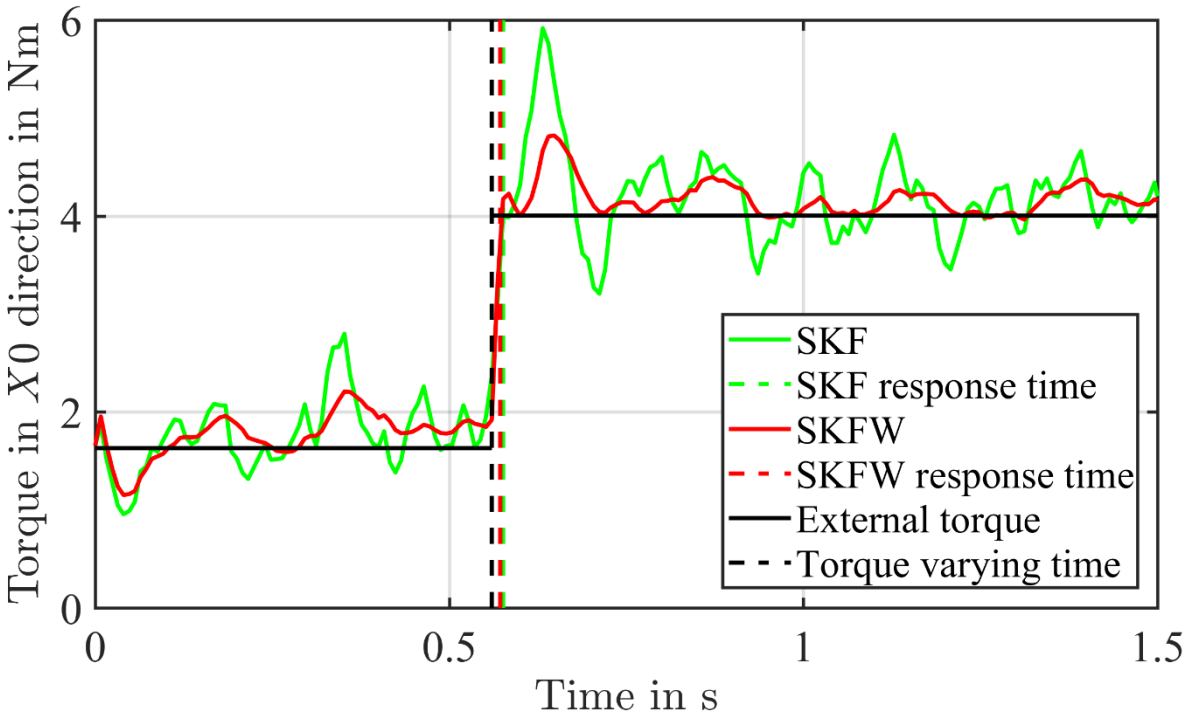

Fig. 5.7. Estimation of contact torque (with 1000 g lead inside the cup) in the $X0$ direction.

As a function of payload, the root-mean-squared errors (RMSE) of the force estimation based on the SKF and the SKFW are displayed in Fig. 5.8. The response time of force sensing based on both methods also varies with the payload changes (Fig. 5.9).

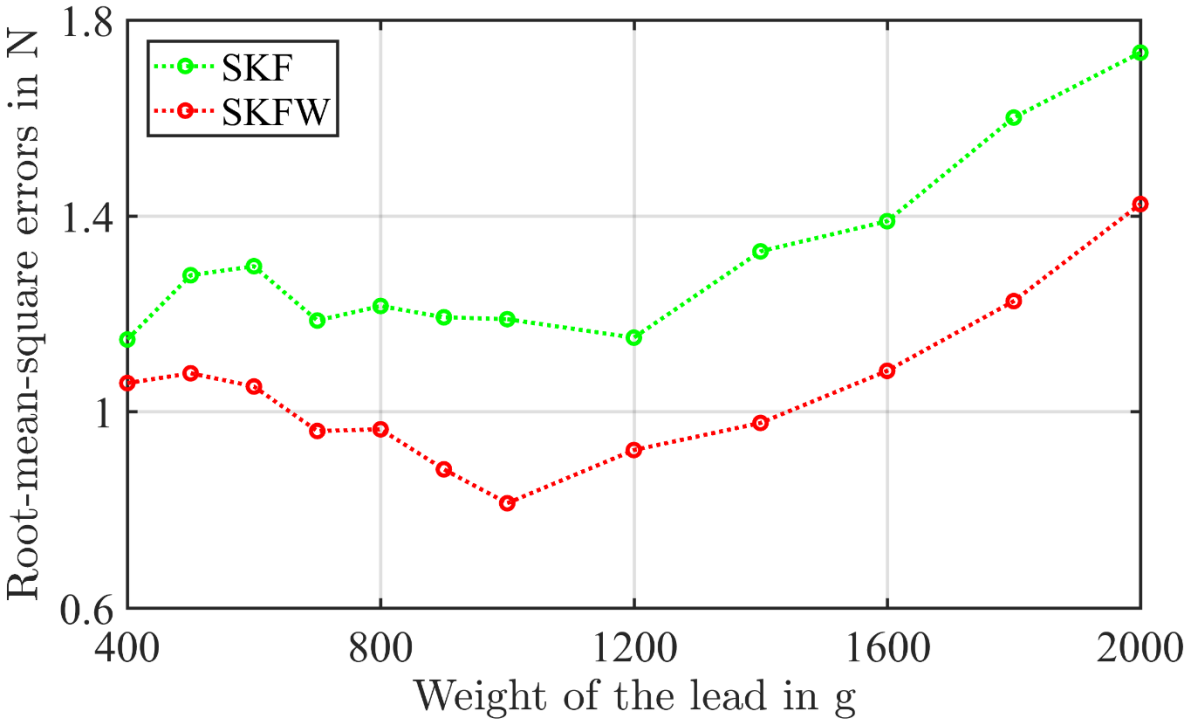

Fig. 5.8. The RMSE of the external force estimation based on the SKF and the SKFW from 400 g to 2000 g.

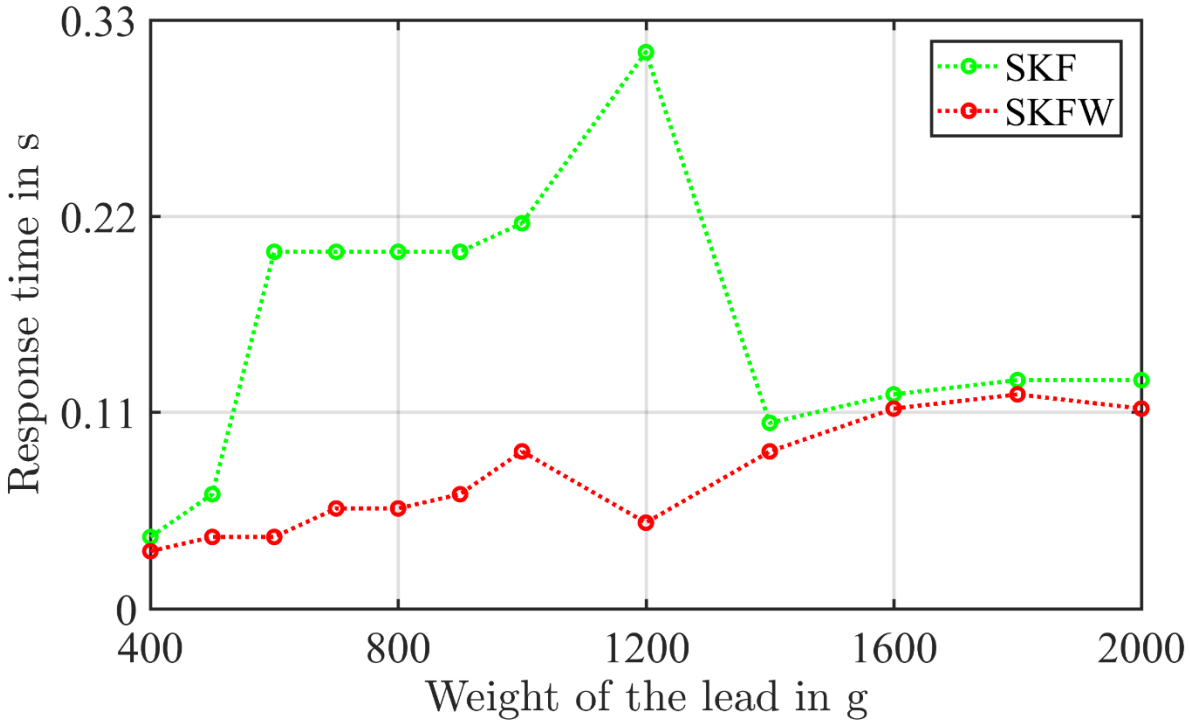

Fig. 5.9 Comparison of the response time with different payloads.

The proposed contact force estimation method based on the SKFW worked effectively in the physical experiments and the response time is reduced by 55.2% on average compared to an established SKF approach [96] (Fig. 5.9). Furthermore, the root-mean-square errors between the estimator force and the measured contact force is reduced by 20.8% (Fig. 5.8). As

to the torque estimation, the estimation errors of the SKFW are smaller than those from the SKF (Table 5-2). The response time of the SKFW is similar to that of the SKF for some payloads. However, the proposed SKFW outperforms the SKF at each payload.

5.1.3. CFTE at different speeds with constant payload

In order to validate the generalization of the WMA-based AKF across different speeds, an experiment with consistent payload but different speeds of 0.04 m/s, 0.06 m/s, and 0.08 m/s (as shown in Fig. 5.1) was conducted. The RMSE of the estimation errors of the approaches using the same payload and at different speed are compared in Table 5-1 and Table 5-2.

Table 5-1 RMSE [N] of the force estimation errors with different motions

Speed / Method	0.04 m/s	0.06 m/s	0.08 m/s
SKF	1.43	1.28	1.03
SKFW	1.32	1.14	0.93

Table 5-2 RMSE [Nm] of the torque estimation errors with different motions

Speed / Method	0.04 m/s	0.06 m/s	0.08 m/s
SKF	0.31	0.32	0.29
SKFW	0.21	0.18	0.15

5.1.4. CFTE in different orientation with constant payload

Another comparison experiment with the UR5 moving in the alternative orientation is conducted. Both methods are employed and their estimation results are displayed in Fig. 5.10. To validate the effect of the variable span, the force estimation results based on the SKFNW (Weighted Moving Average with No Variable Span) and the SKFW (Weighted Moving Average with Variable Span) are displayed in Fig. 5.11.

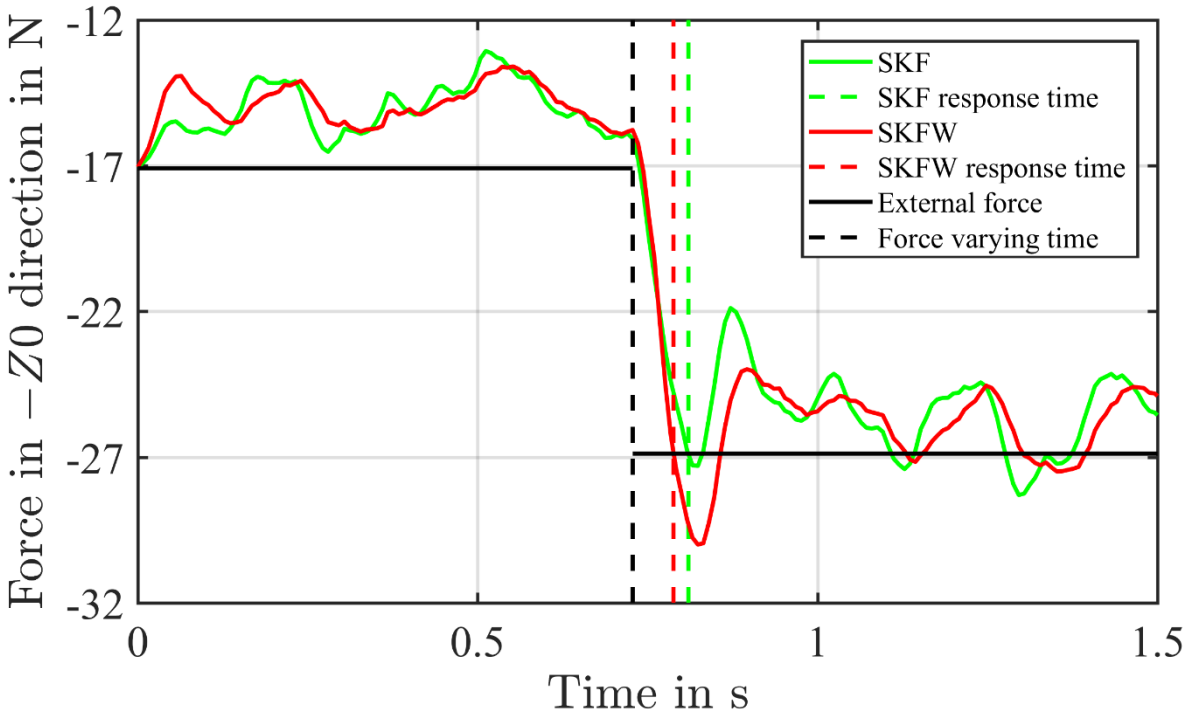

Fig. 5.10. Force estimation results of the comparison experiments (in different orientation from that in Fig. 13) in the $-Z0$ direction (with 1000 g payload).

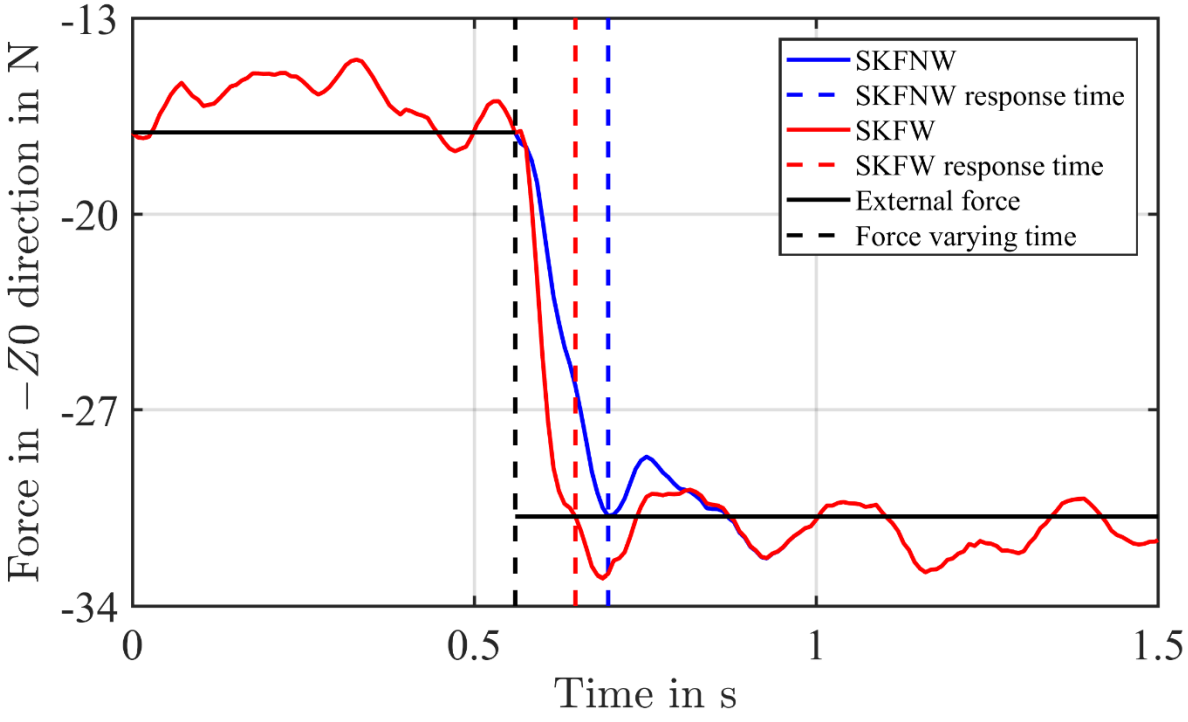

Fig. 5.11. Estimation of contact force (with 1400 g payload) in the $-Z0$ direction.

5.1.5. Discussion

a. Influence of the WMA and the variable span

The proposed SKFW method was validated with the TCP of the UR5 moving at different speeds (Table 5-1 and Table 5-2) and in different orientations (Fig. 5.10). The proposed method ultimately produces force and torque estimation errors that are smaller than the established method.

The SKFW works faster than the SKFNW when dealing with the varying contact force. Hence, it can be concluded that the variable span improves force detection speed. When external force is exerted on the manipulator, the previous current samples are omitted in each averaging step because of the variable span. The benefit is twofold: Firstly, the fixed span approach has a longer response time. Secondly, estimation errors are reduced significantly by the proposed approach since there are apparent discrepancies between previous motor current samples and the current samples extracted when external force is applied (Fig. 5.4).

In summary, both the WMA and the function of the variable span improves estimation performance in terms of response time and estimation quality. The noise in the measured current is reduced by the WMA and thus the diagonal elements of related $\boldsymbol{\sigma}_{\mathrm{Dyn}}^2$ are reduced. Smaller diagonal elements of covariance matrix $\boldsymbol{\sigma}_{\mathrm{Dyn}}^2$ lead to a lower response time for the system.

b. Influence of the generalized momentum model

Since the dynamic model is based on the format of generalized momentum (Eq. 2-44), the proposed contact force estimation method does not require inversion of the manipulator inertia matrix, and consequently the computational burden is low. Furthermore, joint acceleration is not required with the proposed method, and therefore amplification of the measurement noise can be avoided. In particular, acceleration is computed from measured joint angles. However, measurement noise is amplified via the numerical differentiation utilized in a latter step. Uncertainty in the manipulator dynamics is overcome in the approach presented since the noise in the measured current is mitigated by the averaging step and ultimately allows for definition of a more accurate dynamic model. For robotic manipulator tasks that require contact force information, the presented estimation method and control approach are validated in terms of response time and estimation quality. In addition, the costs of physical implementation of the approach cost are lower than the similar standard Kalman filter based approaches [95], [96] as it works independently of force/torque sensors. The proposed SKFW can potentially be applied to any robotic manipulators where the kinematic and dynamic information is accessible. However, the specific benefits in robotic manipulators of different orientations and sizes have not been established experimentally.

c. Limitation of the proposed method and future works

It must be noted that in order to apply the proposed estimation method, a time gap between every two occurrences of the external force during the experiment is assumed to be larger than $t_s \cdot t$. However, $t_s \cdot t$ is generally very small compared to the indicative time of the system dynamics. Hence, the assumption is valid in many manufacturing applications.

However, if the robotic manipulator is used in an environment with high frequency vibration, such as a turning or milling processes, the time gaps between contact may become smaller than $t_s \cdot t$, and the approach may not yield benefit. Future research should be conducted to evaluate the performance of the approach in such turning, milling, or grinding applications.

d. Conclusion

The proposed approach was validated in a physical system implementation with differing loading scenarios. The validation used key parameters that are critical for the effective implementation of robotic manipulators – response time and force estimation precision. The control system was not aware of the force contact *a priori* nor the weight of the end effector loading. Using a series of loading scenarios shows that parameters of the approach are not specifically tuned to succeed in limited range of applications. Hence, the successful results from the implementation of the approach can be assumed for industrial applications.

Identification results varied as the environmental conditions were altered. For example, the friction and noise were affected by the loading. This problem was somewhat mitigated in this case as the maximum load on the manipulator was 2 kg. However, a comprehensive system identification method will help to obtain more accurate model parameters. Therefore, modern machine learning techniques will be employed in the future work to determine the friction and noise.

In case of some particular orientations, singularity may occur and thus, the magnitude of the external wrench in some directions cannot be observed by the robot. Consequently the effectiveness of the proposed method will be affected. This phenomenon will be considered in the future to improve the generalizability of this work.

6. CFTE OF THE SINGLE-ARM ROBOT WITH THE AFK BASED ON MSMA

In this chapter, the mode-switching moving average (MSMA) is analysed using the similar validation to the SKFW (Chapter 5). The algorithms used in this chapter are introduced in section 6.1.1. The experiments are repeated with the manipulator moving at different speeds and with different orientations (section 6.1.2. to 6.1.4.). The proposed method is discussed in section 6.1.5.

6.1.1. Codes used in the experiments

Similar to the codes used in Chapter 5, the computer sent the read and storage commands ("realtimeclient.py" (Appendix A1) and "jointqqdidirecord.py" (Appendix A2)) to the manipulator. The pre-designed trajectory of the UR5 is transferred by "UR5.py" (Appendix A3) and "experiment.py" (Appendix A4).

The only script used in this experiment, which is different from that employed in Chapter 5, is the file of the mode-switching moving average with variable span (Appendix B7). The current smoothing effect of the elbow joint is used as an example in Fig. 6.1.

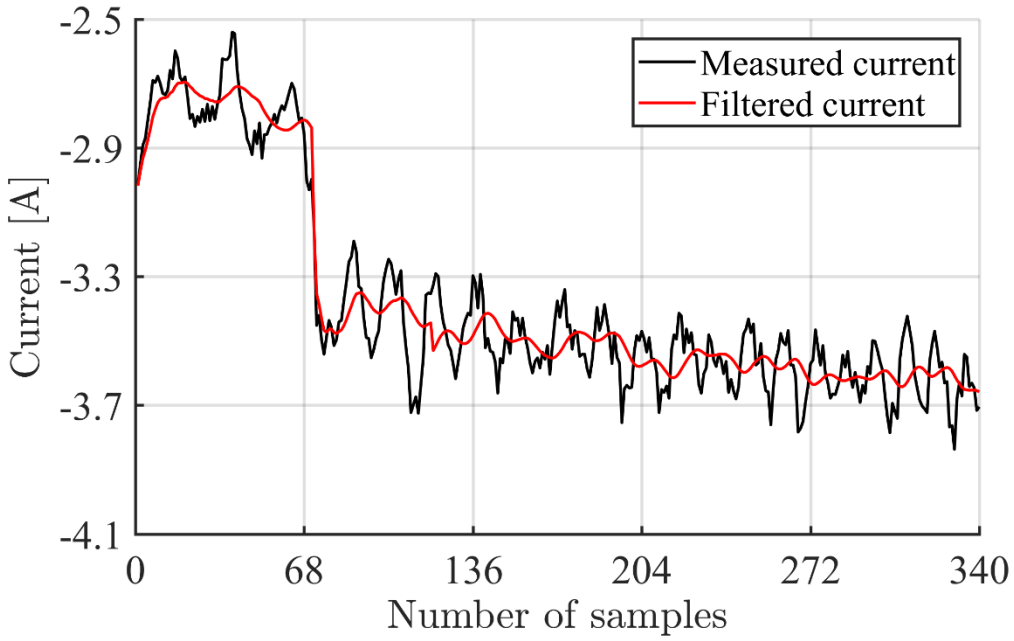

Fig. 6.1. Smoothing effect of the MSMA with variable span.

The joint output torques were calculated using the filtered current and Eq. 3-1. The dynamic model of the UR5 manipulator was then modelled in UR5dynamics.m" (Appendix B1) and its subroutine scripts ("Coriolis.m" (Appendix B3), "christoffel.m" (Appendix B4), "gravity.m" (Appendix B5), and "Trans.m" (Appendix B6)) by Matlab.

6.1.2. CFTE with varying payload

In this section, experiments (as shown in Fig. 5.1) undergo the same motion with payloads of 100 g to 1000 g in

increments of 100 g.

Fig. 6.2(a) and Fig. 6.2(b) show the performance of the varying contact force and torque (with 1000g payload) estimation based on the peer method of the CKF [96], the approach of the AKF without the WMA, and the proposed AKF that includes WMA.

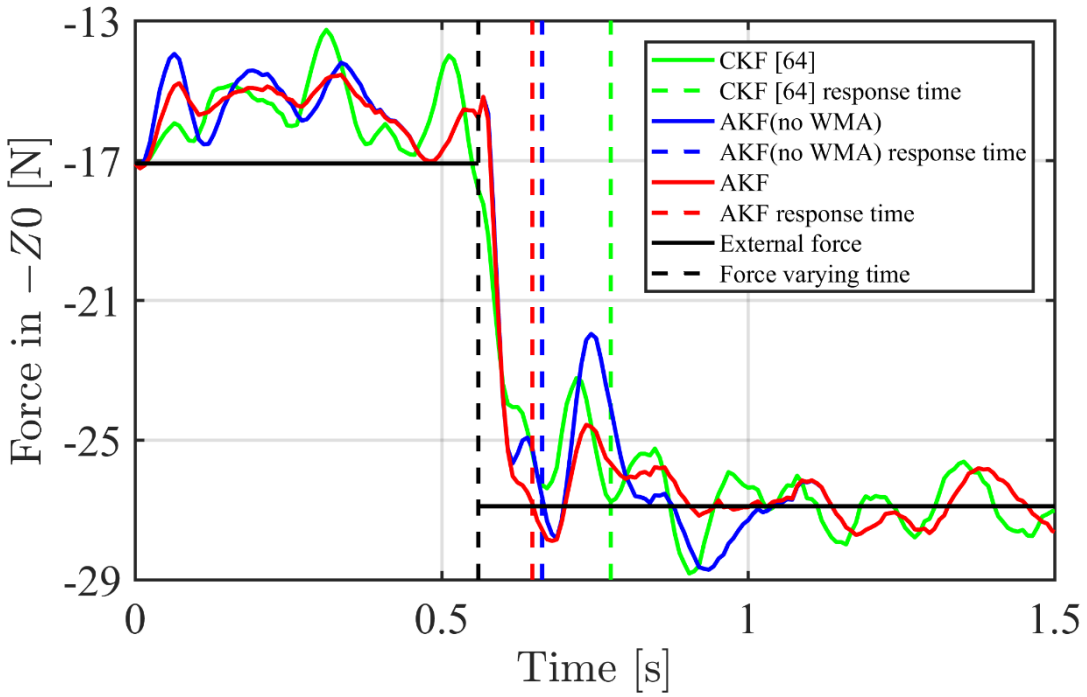

(a) Estimation of the varying force with the lead of 1kg.

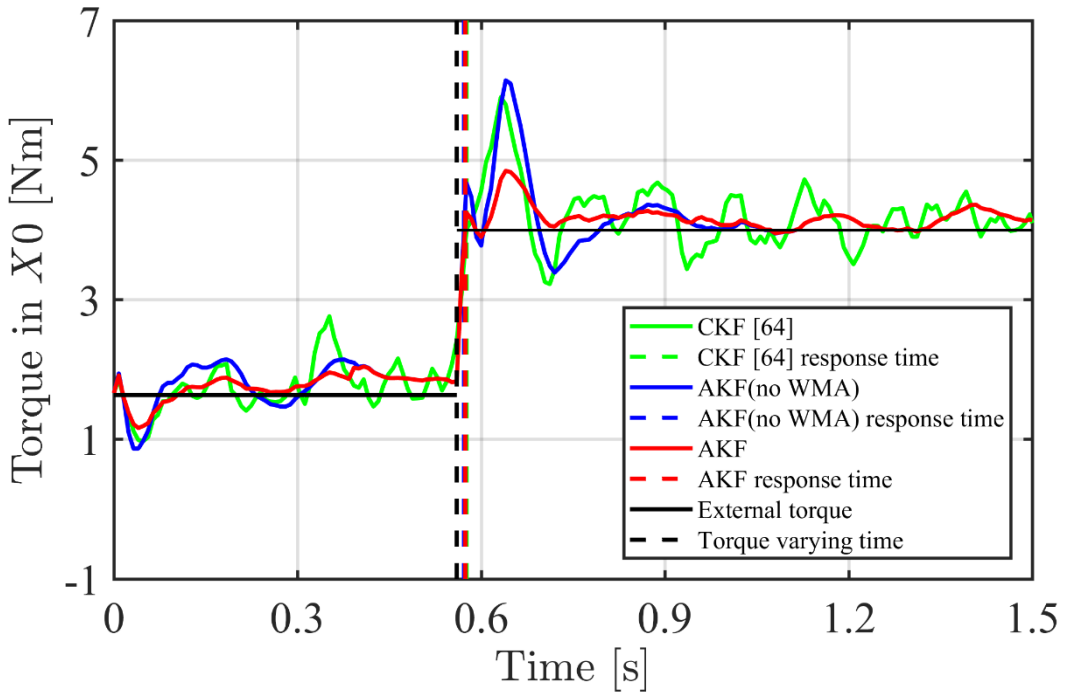

(b) Estimation of the varying torque with the lead of 1kg.

Fig. 6.2. Estimation of the force in -$Z0$ direction and torque in $X0$ direction. The estimation results of the AKF and the AKF (no WMA) are very similar. Therefore the red line and the blue line overlap.

With different payloads, the standard deviation (SD) and root mean squared error (RMSE) of the force and torque estimation based on the CKF and the AKF are displayed in Fig. 6.3 and Fig. 6.4.

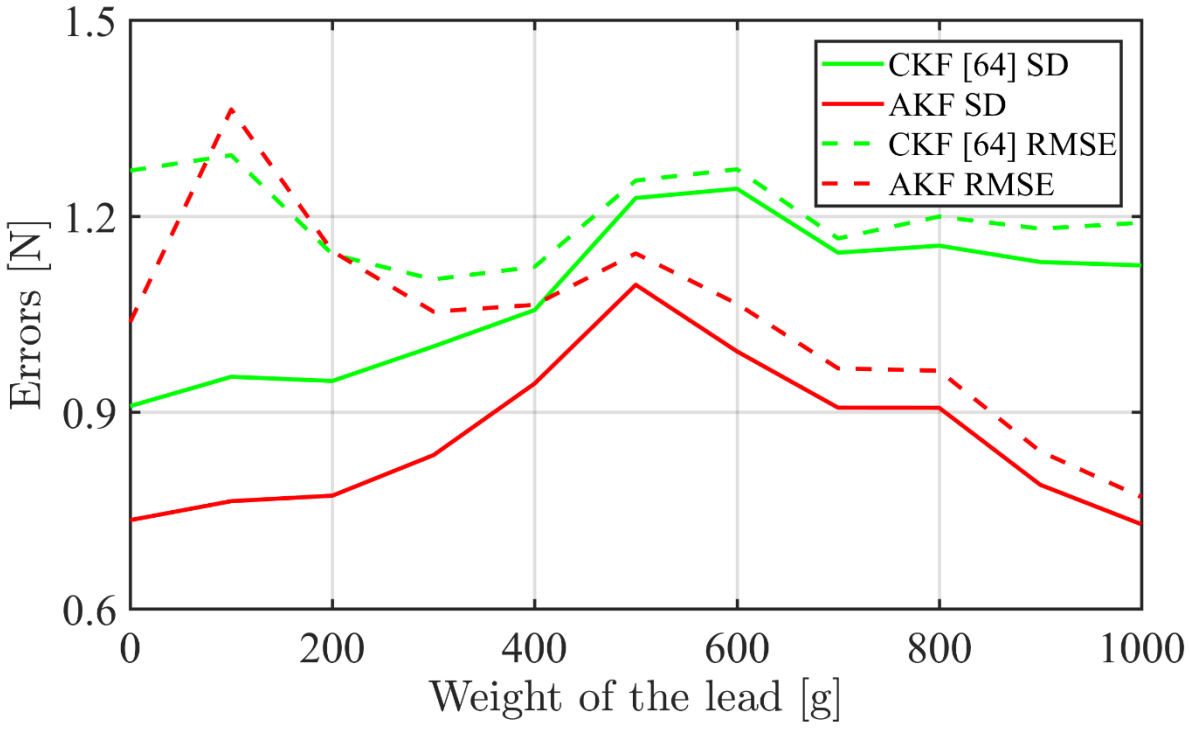

Fig. 6.3. The SD and RMSE of the contact force estimation based on the CKF and the AKF with different payloads.

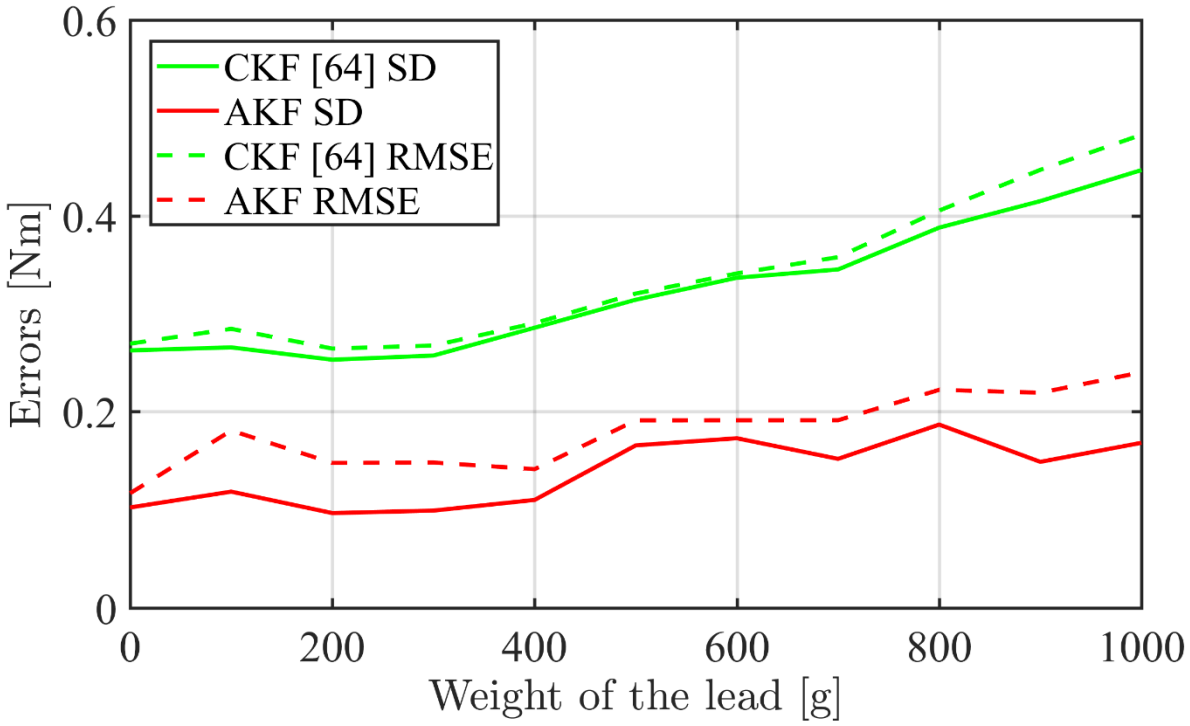

Fig. 6.4. The SD and RMSE of the contact torque estimation based on the CKF and the AKF with different payloads.

The response time of force and torque sensing based on different methods varies as the payload changes and is shown in Fig. 6.5(a) and Fig. 6.5(b).

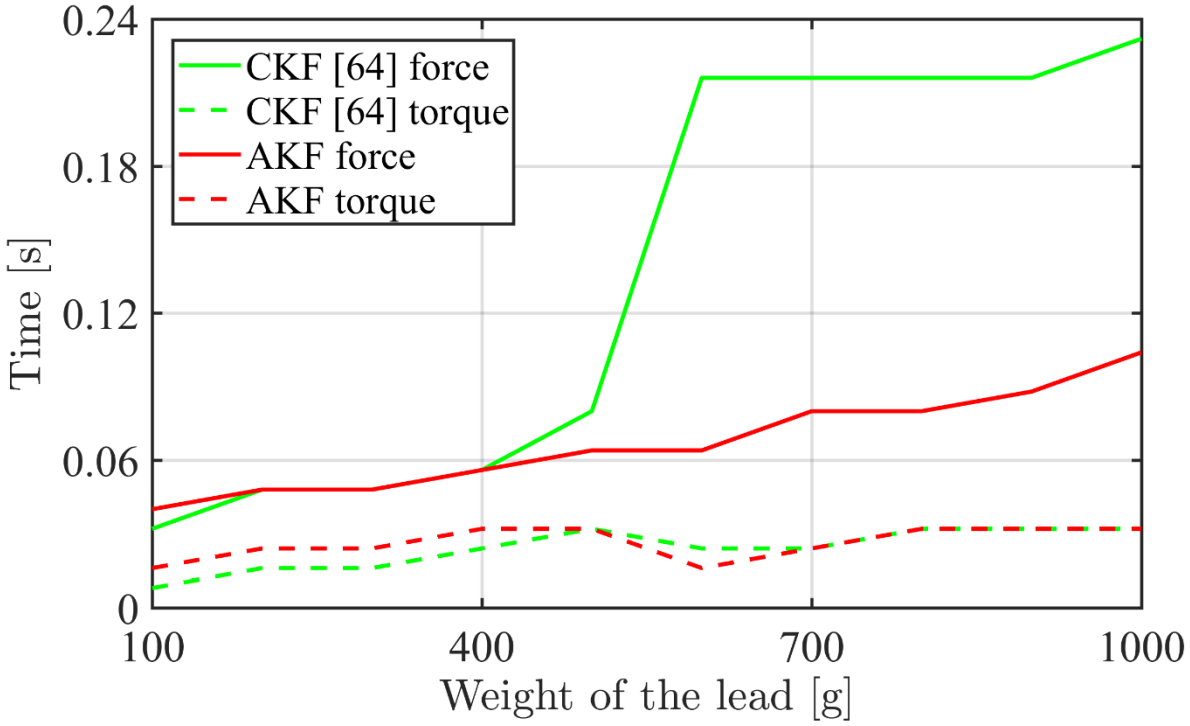

(a) Force/torque estimation of the CKF and the proposed AKF.

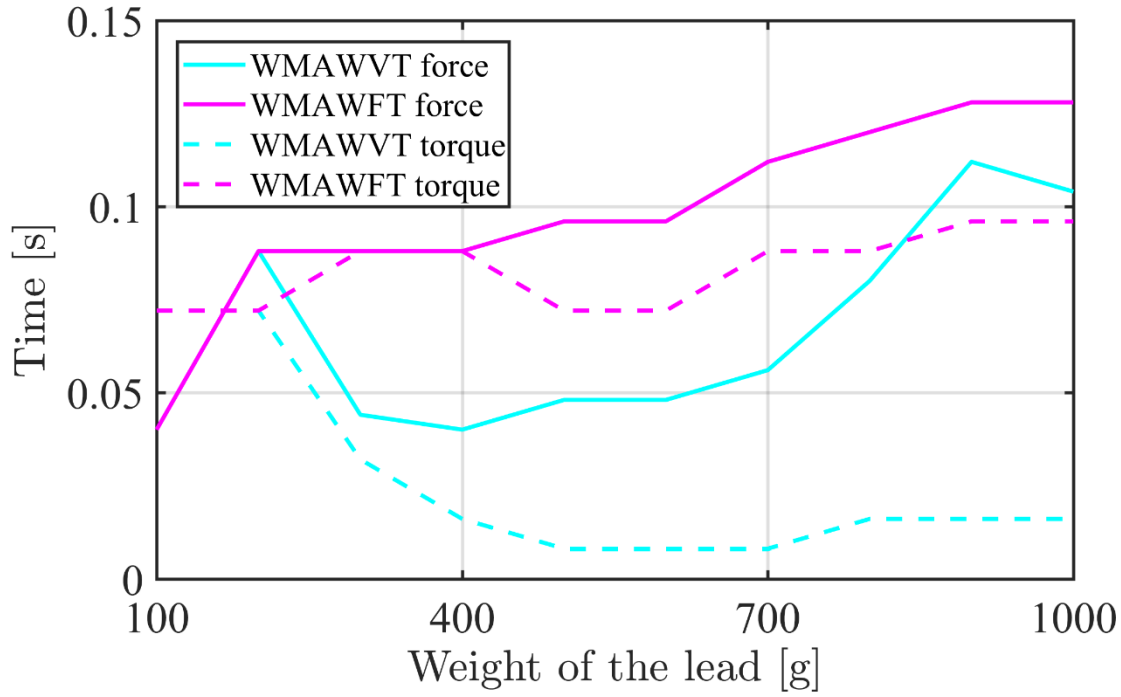

(b) The blue curve and dashed blue one stand for the force and torque estimation time by the proposed AKF with only the WMA and varying time period (WMAWVT). The purple ones represent the estimation based on the proposed AKF with only the WMA and fixed time period (WMAWFT).

Fig. 6.5. Comparison of the response time with different methods.

6.1.3. CFTE at constant speed with the constant payload

In order to validate the generalization of the proposed method across different speeds, another two experiments utilized the same payload but different vertical speeds (0.04 m/s and 0.08 m/s, respectively) as shown in Fig. 5.1. Fig. 6.6(a) and Fig. 6.6(b) show the estimation results of constant force and torque. The RMSE of the estimation errors in Fig. 6.6(a) and Fig. 6.6(b) are summarized in Tables 1 and 2.

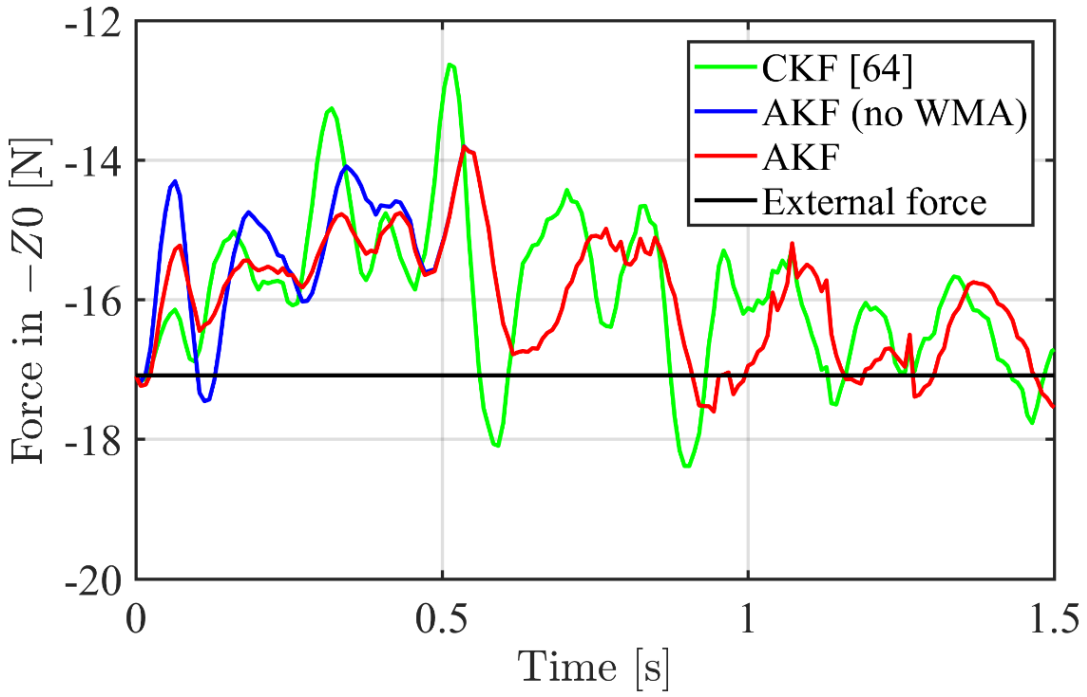

(a) Estimation of the constant force.

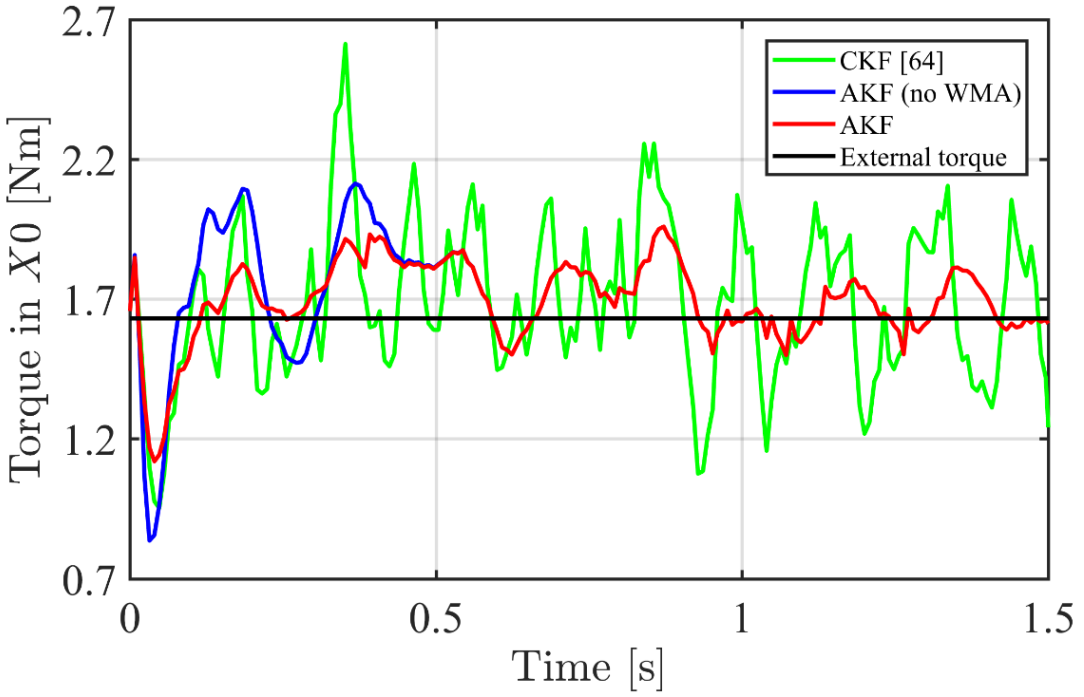

(b) Estimation of the constant torque.

Fig. 6.6. Estimation of the force in -$Z0$ direction and torque in $X0$ direction. Under some circumstances, the estimation results of the AKF and the AKF (no WMA) are very similar. Therefore the red line and the blue line overlap each other.

Table 6-1 RMSE [N] of the force estimation errors in different periods (0.06 m/s). (For Table 6-1 - Table 6-6, *denotes periods dominated by WMA averaging, and ** denotes periods dominated by HMA averaging – note that AKF automatically switches between WMA and HMA if permitted)

Time / Method	0-0.45 s	0.45-1.5 s	0-1.5 s
CKF	0.94	1.19	1.12
AKF(no WMA)	0.92**	0.88**	0.97
AKF	0.60*	0.88**	0.84

Table 6-2 RMSE [Nm] of the Torque estimation errors in different periods (0.06m/s).

Time / Method	0-0.45 s	0.45-1.5 s	0-1.5 s
CKF	0.33	0.26	0.28
AKF(no WMA)	0.30**	0.11**	0.20
AKF	0.20*	0.11**	0.14

6.1.4. CFTE at different speeds with constant payload

To establish velocity dependence of the methods, comparison experiments underwent the same payload but with different speeds of 0.04 m/s and 0.08 m/s. Results are displayed in Table 6-3 - Table 6-6.

Table 6-3 RMSE [N] of the force estimation errors in different periods (0.08 m/s).

Time / Method	0-0.45 s	0.45-1.5 s	0-1.5 s
CKF	1.06	0.92	0.98
AKF(no WMA)	1.50**	0.75**	1.07
AKF	0.96*	0.75**	0.90

Table 6-4 RMSE [Nm] of the Torque estimation errors in different periods (0.08 m/s).

Time / Method	0-0.45 s	0.45-1.5 s	0-1.5 s
CKF	0.27	0.28	0.28
AKF(no WMA)	0.27**	0.13**	0.19
AKF	0.17*	0.13**	0.16

Table 6-5 RMSE [N] of the force estimation errors in different periods (0.04 m/s).

Time / Method	0-0.45 s	0.45-1.5 s	0-1.5 s
CKF	1.24	1.58	1.49
AKF(no WMA)	1.59**	1.50**	1.53
AKF	1.09*	1.50**	1.41

Table 6-6 RMSE [Nm] of the Torque estimation errors in different periods (0.04 m/s).

Time / Method	0-0.45 s	0.45-1.5 s	0-1.5 s
CKF	0.28	0.34	0.33
AKF(no WMA)	0.33**	0.26**	0.28
AKF	0.18*	0.26**	0.25

6.1.5. Discussion

a. Effect of the AKF

The proposed contact force/torque estimation method based on the AKF performed better in physical experiments compared to the peer CKF method [96]. The SD and the RMSE of the force estimation based on two methods are shown in Fig. 6.3. With the exception of the RMSE of the estimation at 100g, the errors of the estimation based on the AKF were all smaller than those resulting from the CKF. Hence, in typical industrial scenarios, more accurate estimation of contact force is likely with the proposed AKF. The same conclusion can be made for torque estimation errors with the SD and the RMSE of the AKF being lower than those of the CKF. However, some model uncertainty was evident as the SD is larger than the RMSE (Fig. 6.3 and Fig. 6.4). This is likely to be caused by unmodelled effects, such as the weight and the damping of the hose that powers the gripper (Fig. 5.1).

It can be seen from Fig. 6.5(a) that the AKF conducted apparently faster force estimation than the CKF when the payload increased above 400 g. Below this threshold, the time consumed by both filters was very similar. The response time of torque estimation was similar across the two methods during all experiments.

The magnitude of the exerted torque is relatively small, thus which the advantage of torque-estimating response time is not apparent. As the varying torque gets larger, the response time advantages of the proposed AKF may emerge in concert with the benefits of force estimation. However, a validation experiment is required to validate this claim.

b. Effect of the switching mode, the HMA and the WMA

The mechanism of mode switching, the involved moving averages, and the variable time period all contribute to the improved response time and estimation accuracy. The smoothing effect of the HMA is better than that of the WMA when the time period is fixed and large. Conversely, the performance of the WMA is better in terms of reducing estimation errors and response time. Advantages of both moving average approaches were adopted in this research (Fig. 6.2). As shown in Fig. 6.2(a), the estimation errors resulting from the WMA were smaller than that resulting from the HMA when the time period was varied (from 0 to 0.45 s and from 0.56 to 1 s). Furthermore, the WMA also needed less time to finish the estimation. A similar outcome occurred for the torque estimation (as shown in Fig. 6.2(b)), although the gap in response time was not pronounced. These benefits outcomes were consistent across all payloads considered. Further, both the WMA

and the HMA produced faster response times than the CKF.

In particular, the smaller diagonal elements in the covariance matrix $\boldsymbol{\sigma}^2_{\mathrm{Dyn}}$ led to a reduced response time for the system. The effect of the noise in the measured current was reduced by the mode-switching filter (both the HMA and the WMA) and thus the diagonal elements of $\boldsymbol{\sigma}^2_{\mathrm{Dyn}}$ were reduced.

Compared to the CKF (Table 6-1), the RMSE of the MSMA was reduced from 0.94 to 0.60 in the initial period (0-0.45 s) of force estimation as the WMA was used in the proposed method. Across the time period 0.45-1.5 s, the RMSE was decreased from 1.19 to 0.88 due to the activation of the HMA. Consequently, the estimation precision was improved across the experiment (from 1.12 to 0.84). Furthermore, the WMA (0.60) facilitated better estimation accuracy compared to the HMA (0.92) during the initial time period 0-0.45 s. The RMSE of the torque estimation errors showed the similar results (Table 6-2). In the comparison experiments with the same payload but different speeds, the above conclusion was further validated from Table 6-3 to Table 6-6. The WMA and the HMA facilitate the application of the AKF and the estimation result was improved in terms of response time and estimation accuracy.

c. Effect of the variable time period

The variable time period further reduced the response time when interacting with the unexpected change in external force. Fig. 6.5 shows the effect of allowing the method to adapt the averaging span. In particular, when the external wrench was exerted on the manipulator, the proposed WMAWVT approach was able to omit the previous current samples in each averaging step due to the variable time period. Consequently, the proposed WMAWVT approach led to faster response (with the exceptions of estimation at low weights of 100g and 200g (Fig. 6.5(b)).

d. Effect of tuning strategy of the proposed AKF

In contrast to peer adaptive Kalman filters that update process and measurement covariance matrices using the estimated information, the proposed approach uses measured system uncertainty by offline experiments combined with the real-time dynamic information to update measurement covariance matrices in each iterative step. Hence, better performance was achieved by the proposed AKF as it was able to utilize measured values over a shorter timeframe upon recognition of an external wrench and could thus, determine the measured noise characteristics more precisely. Furthermore, tuning routines for the mode-switching moving averages must be considered in this research, and determining the optimal time period provides further potential to optimize estimation accuracy and response time when dealing unexpected loads.

e. Future work

Since the MSMA uses the same foundational averaging functions as the SKFW, potential benefits from optimising the time are similar to those described in section 5.1.5. In particular, a time gap between every two occurrences of the external force during the experiment is assumed to be larger than $t_s \cdot t$. However, this may not be the case for some industrial

applications with high frequency vibrational inputs. Therefore, the proposed approaches will be evaluated scenarios with different characteristic time gaps.

Only UR5 was used in the validation experiments, and the estimation quality may depend on the manipulator used. This concern is somewhat mitigated by the general ability of control system architecture to remain reasonably consistent across geometry. In the future, the AKF will be adapted to industrial manipulators used in various applications, such as polishing, assembly, and lead-through programming.

While there are a number of potential moving average functions that could be implemented in the proposed approach, this paper presents a comparison of the WMA and HMA filters. These filters were chosen for their popularity and comparative ease of implementation. Future research may consider other filters.

A simplified friction model identification was conducted in this research. Although validation of the proposed contact force/torque sensing method was realized based on it, a more advanced friction model identification will strengthen the approach. In the future, modern machine learning techniques will be used to determine a phenomenological friction model.

7. CFTE OF THE DUAL-ARM ROBOT WITH THE AKF BASED ON WMA

In this chapter, validation of the proposed AKF based on the WMA with variable span on the dual-arm robot is conducted. In section 7.1.1. , experiments are conducted with varying payload and the estimation results are shown. Section 7.1.2. discusses the estimation results.

A dual-arm robot was constructed with two UR5 (Fig. 7.1). To couple the UR5 robots, an end effector (Fig. 7.2) was designed by Solidworks and fabricated with a 3-D printer (Fig. 7.3). Two end effectors were rigidly attached to two manipulators using bolts (Fig. 7.4). A wooden batten (Fig. 7.5) was inserted through the holes on the end effectors. The contact between the wooden batten and the holes was tight, and thus the batten remained stationary with respect to the end effectors when two UR5 moved. The reason a wooden batten is used is threefold: First, the batten is rigid and allowed the two manipulators to be coupled. Secondly, the actual scenario is simulated since minor dislocation between two manipulators will cause obvious internal force/torque. Thirdly, in the case of unexpected kinematics, the wooden batten is easy to be broken and thus two UR5 are protected from damage.

The TCP is located in the middle of the batten (Fig. 7.7(a)). It is worth noting that, the batten is effectively rigid and thus end effectors of the two UR5 must maintain compatible positions and rotations with each other during motion. A simple option is to command two manipulators travel vertically at the same speed. The effectiveness of the proposed CFTE methods was demonstrated in experimental tests with single scenario: at constant speed and with varying payload.

In the general case, the internal interaction ($\boldsymbol{\tau}_{\text{int}}$ in Eq. 2-35) between two UR5 arises as they move. However, the main purpose of this experiment is to validate the proposed methods in the process of the CFTE. Therefore, the trajectory of two arms are specially defined in order to minimize the internal force and this simplifies the system dynamics.

When the experiment starts, the same data read and storage commands are sent from the computer to two UR5 by “realtimeclient.py” (Appendix A1) and “dualarm-jointqqdidirecord.py” (Appendix A5). While both UR5 had the same commands, each had its own port (192.168.1.1 and 192.168.1.2, respectively). Consequently, the real-time dynamic and kinematic information from both manipulators was stored in two different “.CSV” files ('1800g1.csv' and ‘1800g2.csv’) and then used to estimate the external wrench by codes (Appendix B8).

The UR5 movement commands are sent by “UR5.py” (Appendix A3) and “dualarm-experiement.py” (Appendix A4). Receiving the motion commands, two UR5 were commanded to raise at a speed from 0 to 0.06 m/s at a constant acceleration of 0.24 m/s^2. After 0.25 s, two end effectors reach 0.06 m/s and kept rising at the constant speed. Hence, the two end effectors stayed stationary with respect to each other and deformation of the wooden batten was avoided. Consequently, internal force/torque should be negligible.

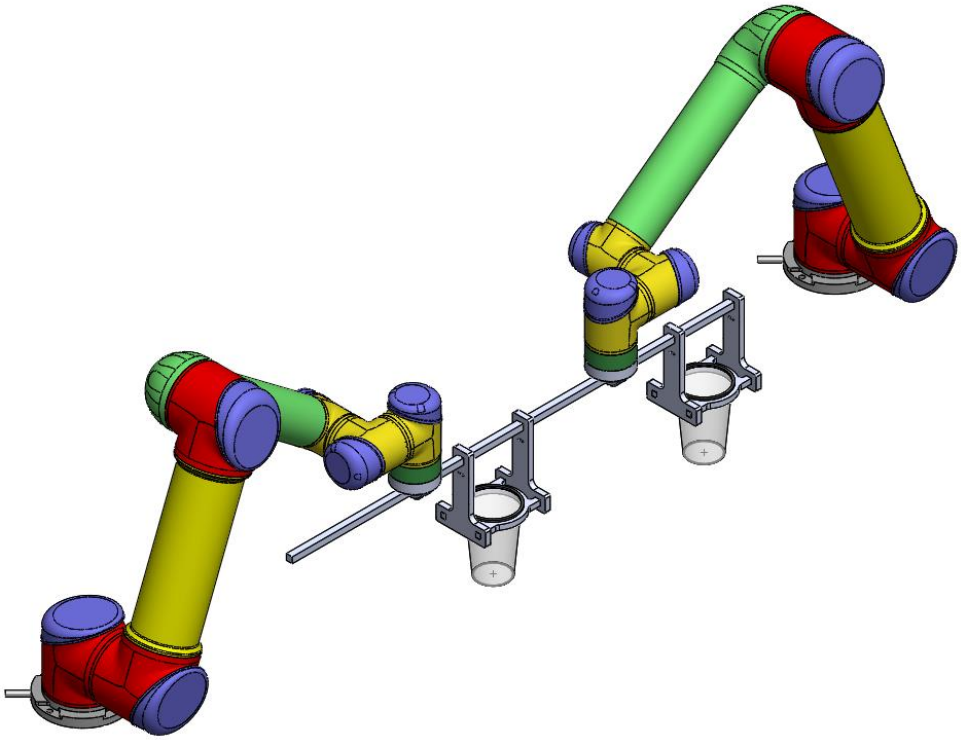

Fig. 7.1. Dual-arm robot.

Fig. 7.2. End effector.

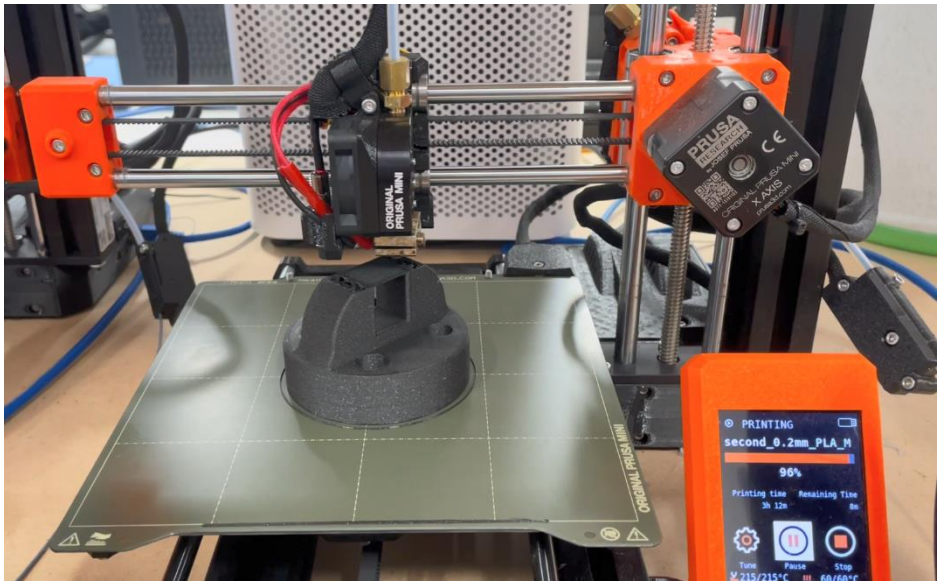

Fig. 7.3. 3-D printer.

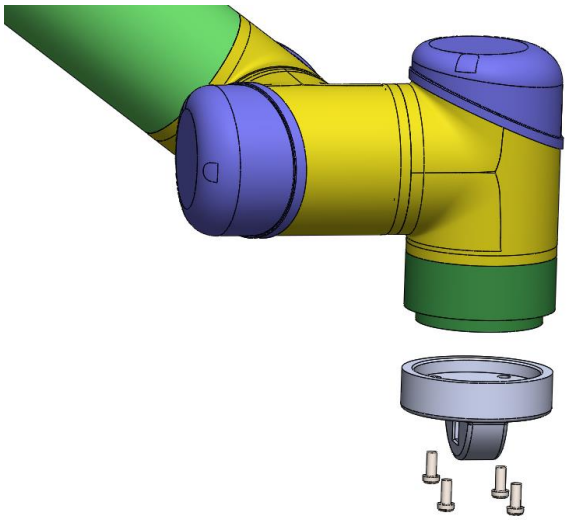

Fig. 7.4. The end effector is attached to the manipulator using bolts.

Fig. 7.5. Wooden batten.

The experimental process involves three steps:

Step 1. The TCP is moved to an initial position (Fig. 7.7(a)). After initialization, the TCP is programmed to move up vertically at constant speed. The payload (lead filled cups in Fig. 7.7) is initially not engaged by the cup holders. The effect of the batten and two holders on the TCP can be deemed as a constant force of 5.4 N in the $-Z0$ direction (Fig. 7.6) and a constant torque in the $X0$ direction.

Step 2. The payload is engaged by the moving holders, as shown in Fig. 7.7(b). The model has no *a priori* information to anticipate coupling with the payload.

Step 3. The payload and cup holders are coupled and raised together (Fig. 7.7(c)). The effect of the payload and the holders can be regarded as a constant force in the $-Z0$ direction and a constant torque in the $X0$ direction.

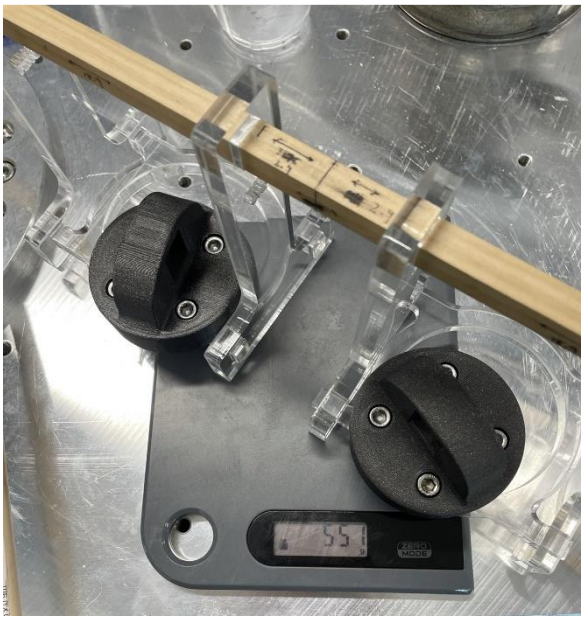

Fig. 7.6. The black grippers, batten, and cup holders weigh 0.55 kg.

(a) Initial pose. Two UR5 are coupled by a batten. The TCP is located in the middle of the batten and goes up at constant velocity of 0.06m/. Initially the cups are not engaged.

(b) Two cups and the lead inside them start to move up vertically due to the movement of the grippers.

(c) Two UR5 move up at constant speed as the TCP does.

Fig. 7.7. Demonstration scenario for the experiment. Two UR5 manipulators are initialized as (a). The TCP is commanded to move up vertically and the effect of two cups filled with lead can be regarded as constant external wrench exerted on the TCP.

7.1.1. CFTE with varying payload

Fig. 7.8(a) and Fig. 7.8(b) show the performance of the contact force and torque (with 4000g payload) estimation based on the peer method of the CKF [96] and the proposed AKF based on the WMA with variable time period. The force estimation errors in different periods are concluded in Table 7-1.

Table 7-1 RMSE [N] of the force estimation errors in different periods. (*denotes periods of WMA averaging)

Time / Method	0-0.288 s	0.288-0.968 s	0.968-1.256 s	1.256-1.5 s
AKF	1.71*	1.02*	10.45*	0.97*
CKF	1.92	1.73	9.78	1.13

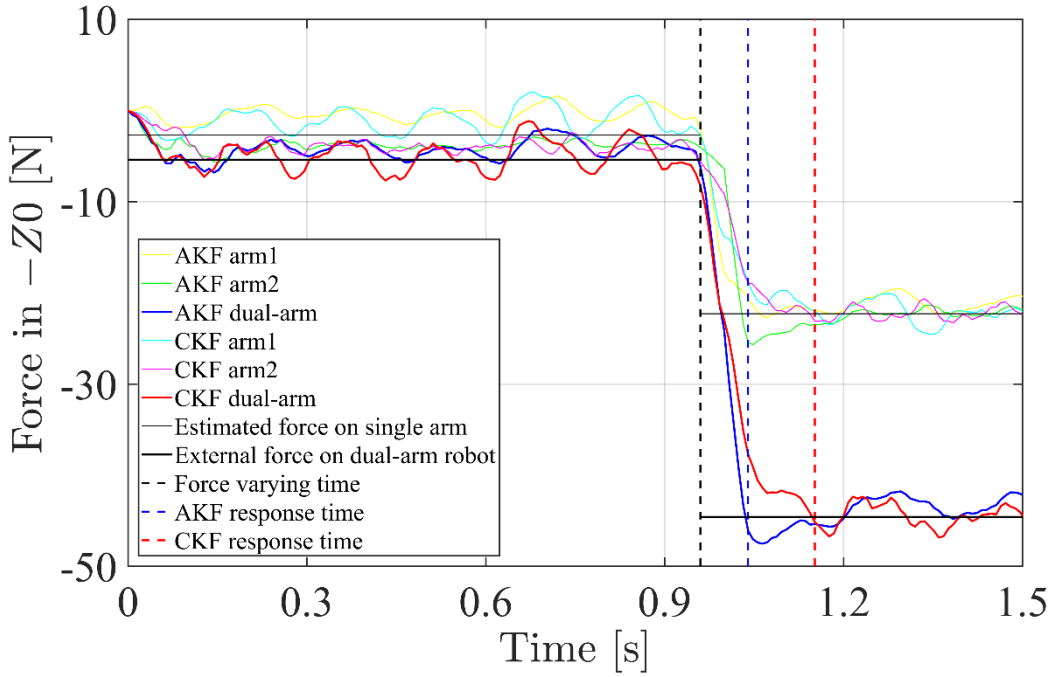

(a) Estimation of the varying force with a payload of 4kg.

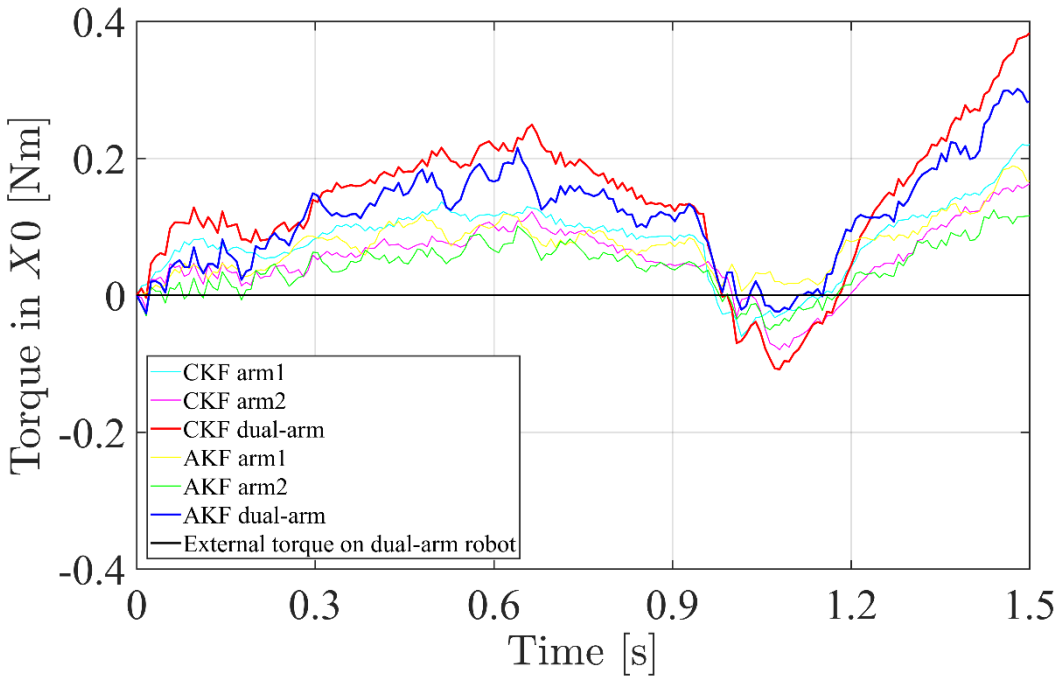

(b) Estimation of the varying torque with the lead of 4kg.

Fig. 7.8. Estimation of the force in -Z0 direction and torque in X0 direction. The actual force/torque (black curve) is compared to estimation with the CKF (red curve) and the AKF with the WMA (blue curve). The dashed blue and red lines show the response time of two methods.

Response time and the standard deviation of the CFTE based on the proposed method and the peer method [96] are

displayed in Fig. 7.9 and Fig. 7.10, respevtively.

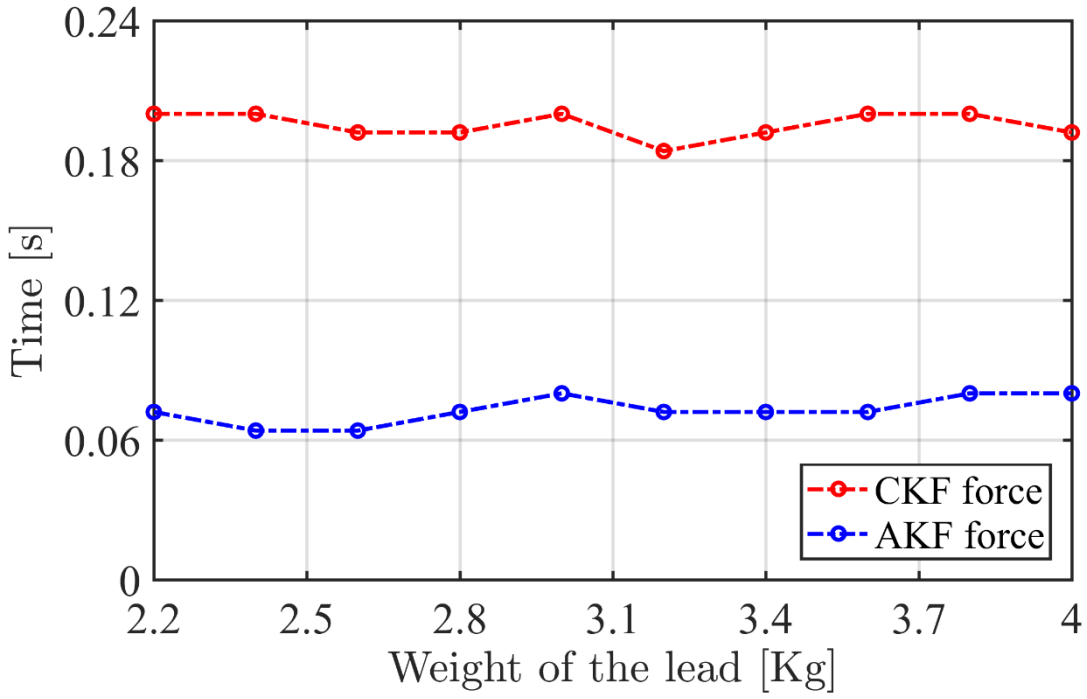

Fig. 7.9. Comparison of the response time with different methods. The red curve and blue one stand for the force estimation based on the CKF and the AKF respectively.

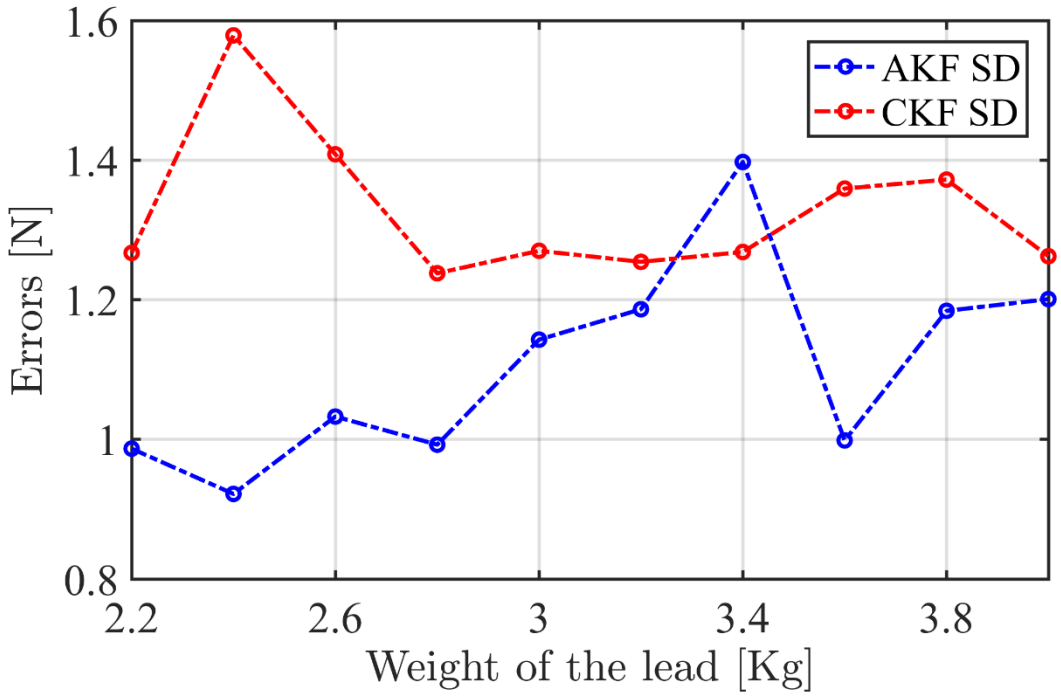

Fig. 7.10. The standard deviation of the contact force estimation based on the CKF and the AKF with different payloads.

In order to validate the performance of the variable time period, the CFTE are conducted with the proposed method and

the method of the AKF based on MSMA with fixed time period. The estimation results are displayed in Fig. 7.11.

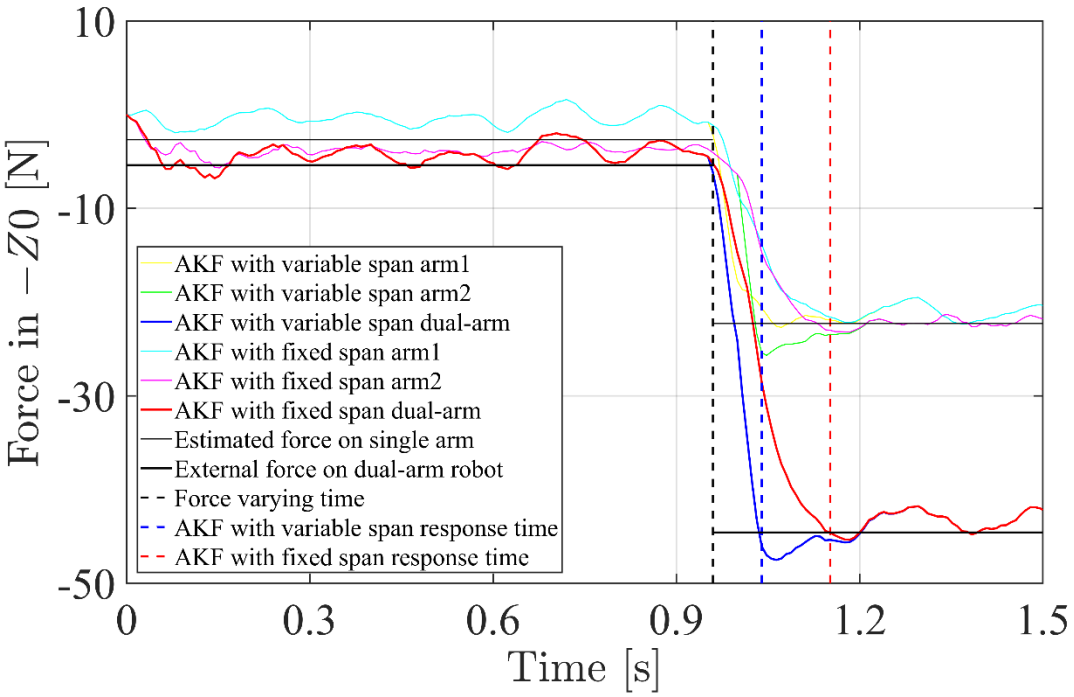

Fig. 7.11. Comparison of the response time with different methods.

7.1.2. Discussion

To the knowledge of the author, peer research of sensorless CFTE is exclusively focused on the single-arm robot, leaving the dual-arm robotic system ignored. Therefore, validation of the proposed method on the CFTE of the dual-arm robot was conducted. The proposed AKF performance exceeded the method using CKF [96]. Both the WMA and the variable time period contribute to the improved response time and estimation accuracy.

a. Interaction between the two robotic arms

The two arms were instructed to conduct mirrored motion in this experiment. Thus the external wrench exerted on both manipulators was expected to be the same. However, small perturbation occurred and perfect parallel movement could not be achieved. Furthermore, the contact between the batten and two end effectors was fixed. Consequently, minor dislocation would cause noticeable internal force between two manipulators.

As shown in Fig. 7.8(a), there is an apparent gap between the estimated force (AKF method) on the master manipulator (yellow line) and that on the slave manipulator (green line). The similar situation happens to the estimation results with the CKF method (magenta line and cyan line). Although the estimated force and torque on both manipulators differed from the ideal values, the observed contact force on the whole robotic system is consistent with the target. To be more specific, the internal effects between two UR5 have no influence on the estimation results of the dual-arm system.

Fig. 7.8(b) shows torque estimation results. The theoretical torques exerted on both manipulators are 0. However, noise and dynamics uncertainty exist, and thus curves fluctuate near zero. Furthermore, flexure in the batten coupled with rotational rigidity in the end effectors may have produced some residual torque on the end effectors. However, the torque estimation errors appear larger than that of force estimation. However, since there was no step input in torque, there was no effective comparator.

b. Effect of the AKF

The proposed contact force/torque estimation method based on the AKF performs better in the physical experiments of dual-arm robot compared to the peer [96] method of the CKF. The standard deviation of the force estimation based on two methods are shown in Fig. 7.10. With the exception of the SD of the estimation at 3.4 Kg, the errors of the estimation based on the AKF are all smaller than those resulting from the CKF. Hence, in cases similar to the experimental process, more accurate estimation of contact force is likely with the proposed AKF. The same conclusion can be made for torque estimation errors with the SD of the AKF being lower than those of the CKF.

It can be seen from Fig. 7.9 that the AKF conducts apparently faster force estimation than the CKF throughout the differing payloads. Furthermore, it is worth noting in Fig. 7.8 that, force estimation on two single robotic arms with the AKF is also faster than that with CKF. This outcome also occurred in section 5.1.5. In this experiment, the payload is exerted in the middle of the batten, and thus the torques exerted on both two UR5 and the dual-arm system are zero.

c. Effect of the WMA

With the WMA, the RMSE of estimation errors are reduced (Table 7-1). Although the WMA leads to larger errors in the period of 0.968-1.256 s, faster estimation is achieved. In particular, the effect of the noise in the measured current is reduced by the WMA and thus the diagonal elements of $\boldsymbol{\sigma}_{\mathrm{Dyn}}^2$ are reduced. Consequently, the smaller diagonal elements in the covariance matrix $\boldsymbol{\sigma}_{\mathrm{Dyn}}^2$ led to a further reduced response time for the system.

d. Effect of the variable time period

The WMA facilitates the application of the AKF and the estimation result is improved in terms of response time and estimation accuracy. Furthermore, the variable time period further reduces the response time when interacting with the unexpected change in external force (Fig. 7.11). The only difference between two methods in Fig. 7.11 is whether the time period is varying or not. In particular, when the external wrench is exerted on the dual-arm system, the proposed approach is able to omit the previous current samples in each averaging step due to the variable time period. Consequently, the proposed approach leads to faster response.

e. Comparison to the single arm SKFW (Chapter 5)

Although the approach used in this chapter was similar to that employed in Chapter 5, validation of the proposed method

was conducted on the dual-arm system. In order to simplify the dynamic model, limitations on the motion were necessary. An experiment considering unexpected internal interaction between two robotic arms will be considered in the future. In this chapter, the limitation that two UR5 must perform mirrored motions in the experimental tests could be avoided and the proposed method can be validated in more general scenarios. However, the simple case analysed in Chapter 7 show evidence of the potential of the overall approach.

8. CFTE OF THE DUAL-ARM ROBOT WITH THE AKF BASED ON MSMA

In this section, experiments in Fig. 7.7 are repeated with the proposed method of the AKF based on the MSMA with variable span. In particular, section 4.3.3. notes that the MSMA used for the CFTE of dual-arm robot is different from that employed for the single-arm robot.

The payloads on the dual-arm robot varied from 4.2 to 6 kg (2.1 to 3 kg in each cup). Two cups were symmetrically distributed on both sides of the TCP similar to Chapter 7. Experiments with varying payload are conducted in section 8.1.1. and the results presented. The estimation performance is then discussed in section 8.1.2.

8.1.1. CFTE with varying payload

Fig. 8.1(a) and Fig. 8.1(b) show the performance of the varying contact force and torque (with 6000g payload) estimation based on the peer method of the CKF [96] and the proposed approach.

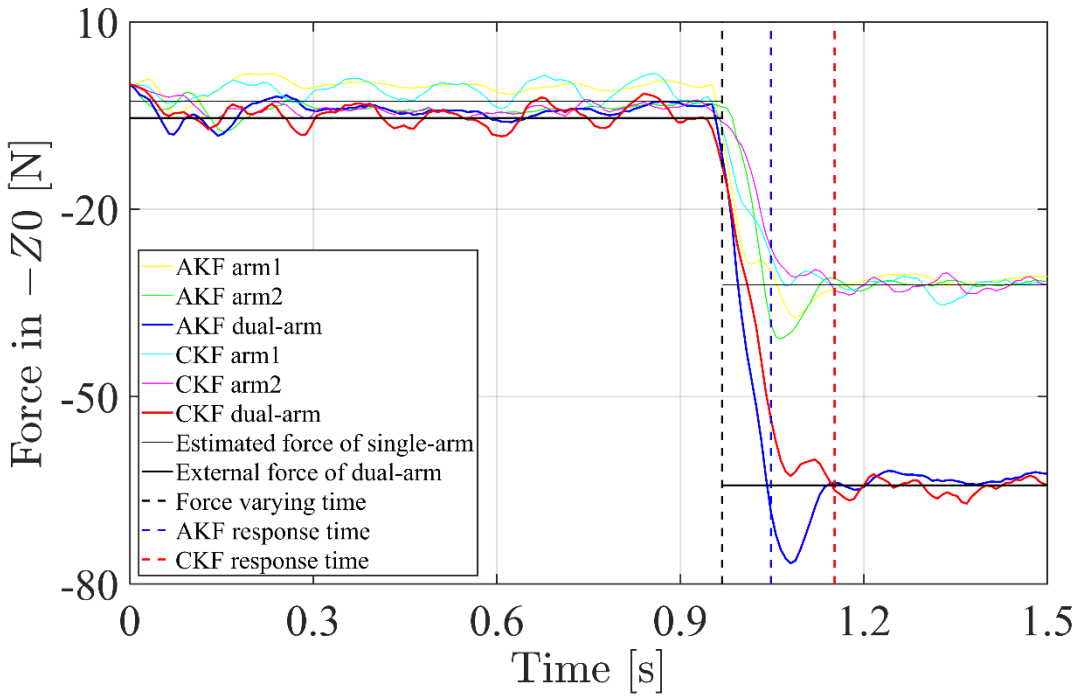

(a) Estimation of the varying force with the lead of 6kg.

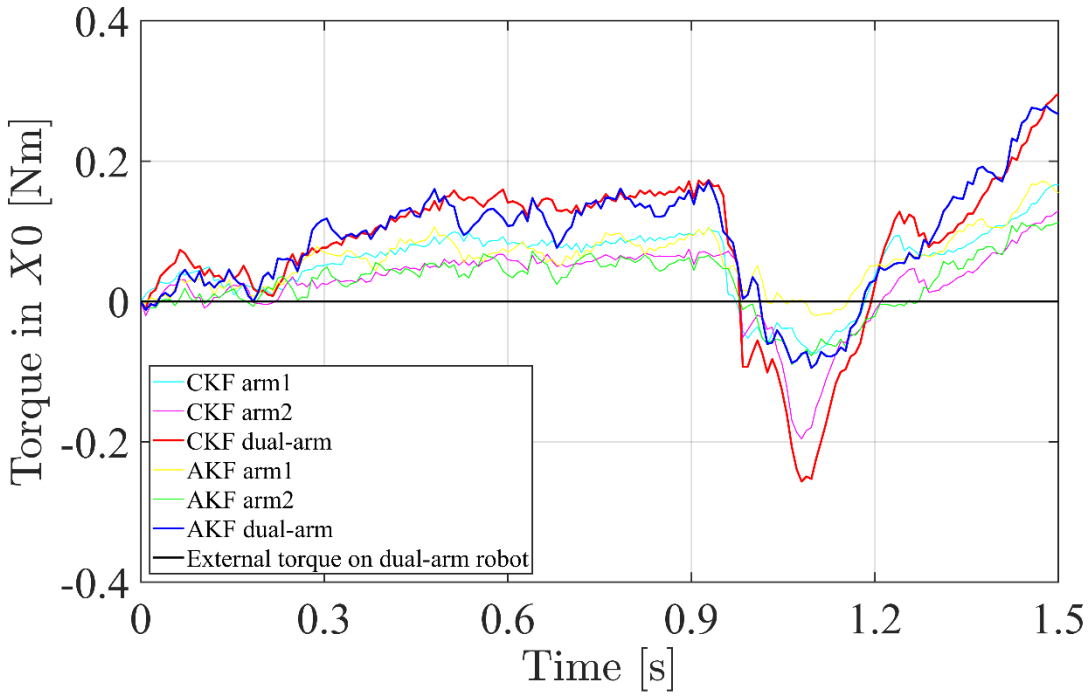

(b) Estimation of the varying torque with the lead of 6kg.

Fig. 8.1. Estimation of the force in -$Z0$ direction and torque in $X0$ direction. The actual force/torque (black curve) is compared to estimation with the AKF (blue curve) with MSMA and the CKF (red curve). The dashed blue and red lines show the response time of two methods.

The RMSE of force estimation errors with two methods in Fig. 8.1(a) is concluded in Table 8-1 and it is divided into four periods. In the starting period (0-0.288 s), the HMA is active and the span is varying. During the period (0.288-0.968 s and 1.256-1.5 s), the WMA is employed and the span is fixed. When the external wrench is exerted on the manipulator and the time period is varying (0.968-1.256 s), the HMA is used. For the peer method, the CKF is active for the duration of the experiment.

Table 8-1 RMSE [N] of the force estimation errors in different periods. (For Table 8-1 - Table 8-4, *denotes periods of WMA averaging, and ** denotes periods of HMA averaging – note that AKF automatically switches between WMA and HMA if permitted)

Time / Method	0-0.288 s	0.288-0.968 s	0.968-1.256 s	1.256-1.5 s
AKF	2.36**	0.81*	16.63**	0.62*
CKF	1.99	1.76	16.05	1.22

Response time and the standard deviation of the CFTE based on the proposed method and the peer method [96] are displayed in Fig. 8.2 and Fig. 8.3 respectively.

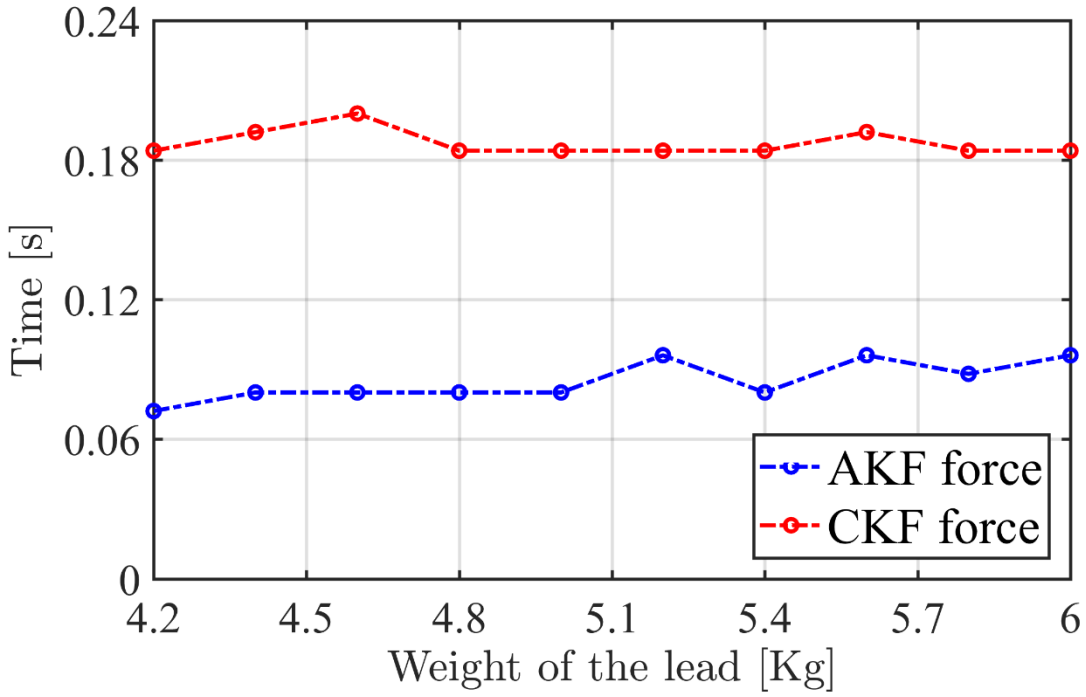

Fig. 8.2. Comparison of the response time with different methods.

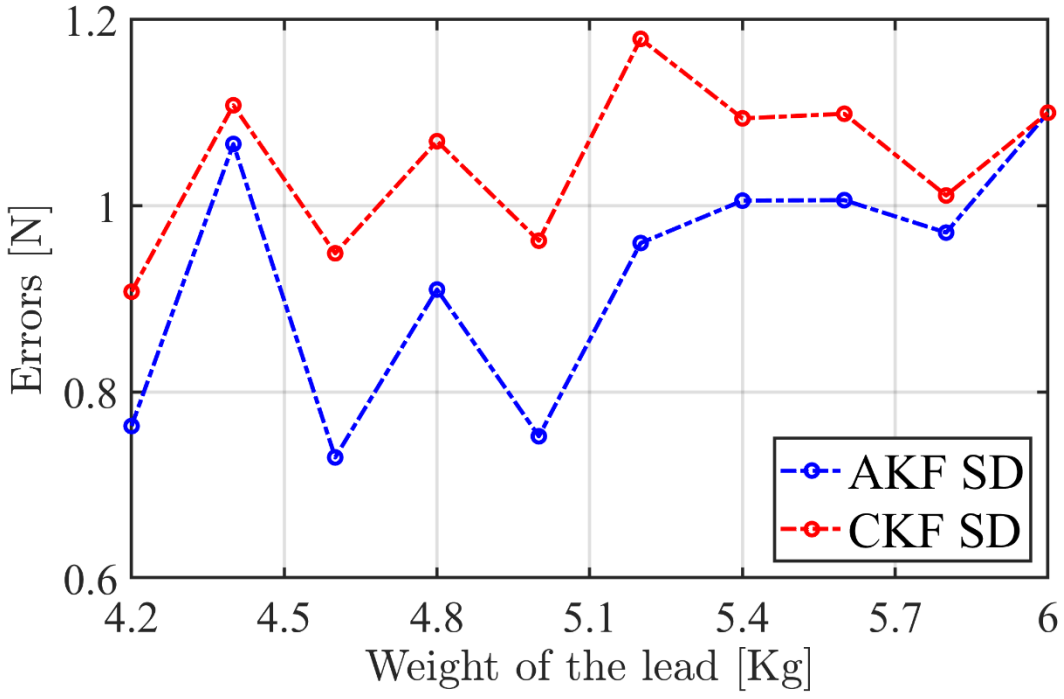

Fig. 8.3. The standard deviation of the contact force estimation based on the CKF and the AKF with different payloads.

In second experiment, the AKF based on the MSMA with variable time period was compared to the AKF based on the HMA with variable time period and the force estimation performance (2.9 kg payload) is displayed in Fig. 8.4.

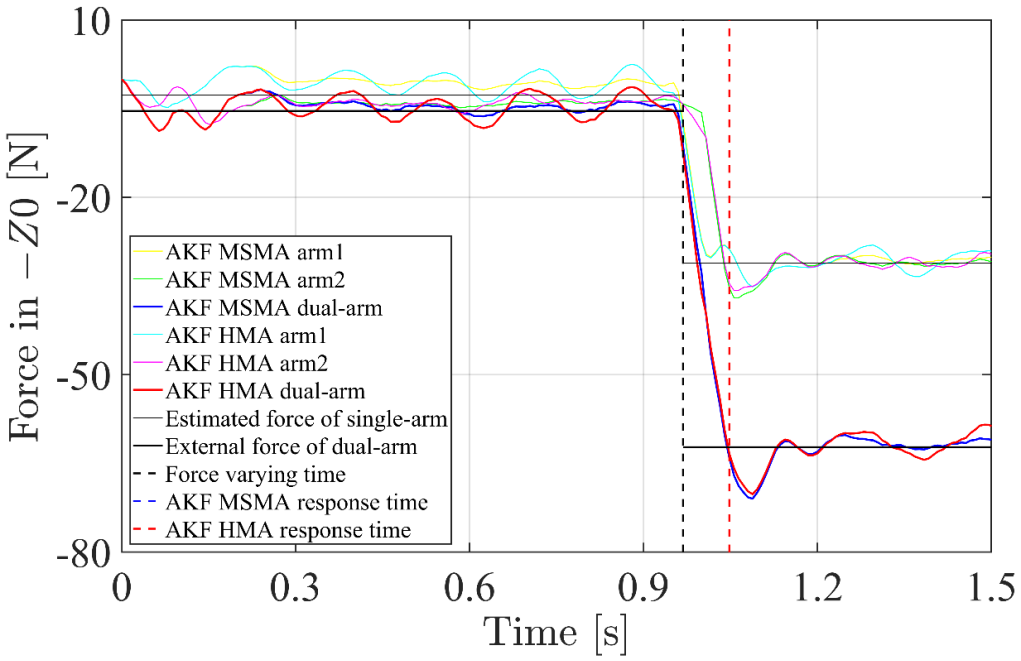

Fig. 8.4. Estimation of the force (62.24 N) in -$Z0$ direction. The actual force/torque (black curve) is compared to estimation with the AKF based on the MSMA (blue curve) and the AKF based on only the HMA (red curve). The dashed blue and red lines show the response time of two methods.

The RMSE of force estimation errors with two methods in Fig. 8.4 is concluded in Table 8-2. The experiment is divided into four periods. In the starting period (0-0.288 s), the HMA is active. In the periods of 0.288-0.968 s and 1.256-1.5 s, the WMA is employed. When the external wrench is exerted on the manipulator and the time period is varying (0.968-1.256 s), the HMA is used. For the AKF HMA method, only the HMA is active for the duration of the experiment.

Table 8-2 RMSE [N] of the force estimation errors in different periods

Time / Method	0-0.288 s	0.288-0.968 s	0.968-1.256 s	1.256-1.5 s
AKF MSMA	2.46**	0.65*	14.79**	0.63*
AKF HMA	2.46**	1.93**	14.79**	1.81**

In the third experiment, the AKF based on the MSMA with variable time period as compared to the AKF based on the WMA with variable time period and the force estimation performance (2.8 kg payload) is displayed in Fig. 8.5.

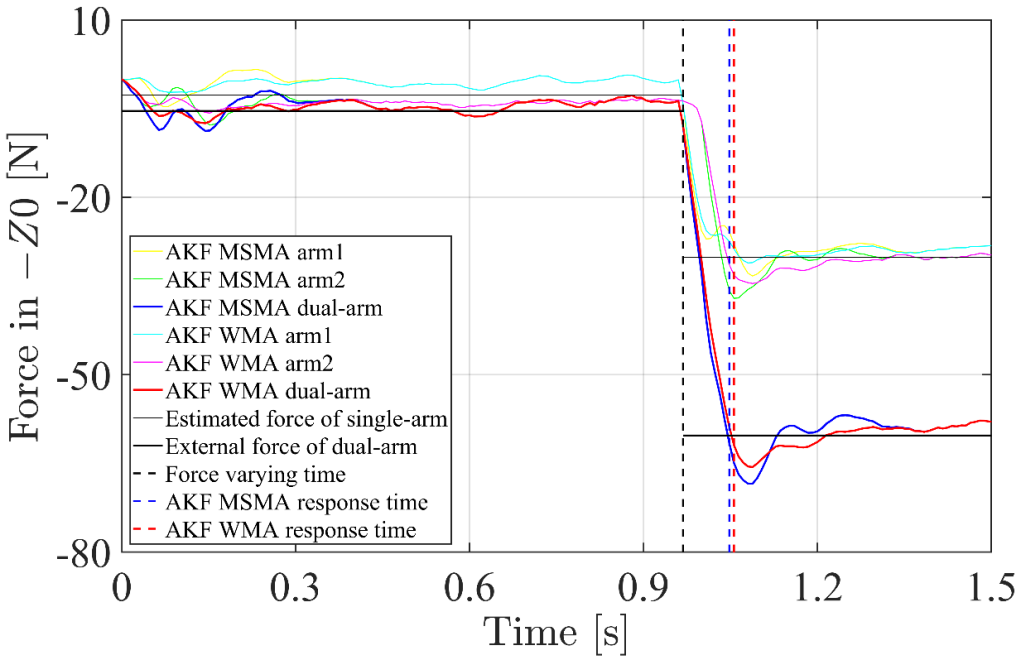

Fig. 8.5. Estimation of the force in -$Z0$ direction.

The RMSE of force estimation errors with two methods in Fig. 8.5 is presented in Table 8-3 and it is divided into four periods. In the starting period (0-0.288 s), the HMA is active. In the fixed-span period (0.288-0.968 s and 1.256-1.5 s), the WMA is employed. When the external wrench is exerted on the manipulator and the time period is varying (0.968-1.256 s), the HMA is used. For the AKF WMA method, only the WMA is active for the duration of the experiment.

Table 8-3 RMSE [N] of the force estimation errors in different periods

Time / Method	0-0.288 s	0.288-0.968 s	0.968-1.256 s	1.256-1.5 s
AKF MSMA	2.52**	0.87*	15.11**	0.75*
AKF WMA	1.77*	0.87*	15.72*	0.76 *

In the last experiment, the AKF based on the MSMA with variable time period was compared to the AKF based on the WMA with no variable time period and the force estimation performance (2.7 kg payload) is displayed in Fig. 8.6.

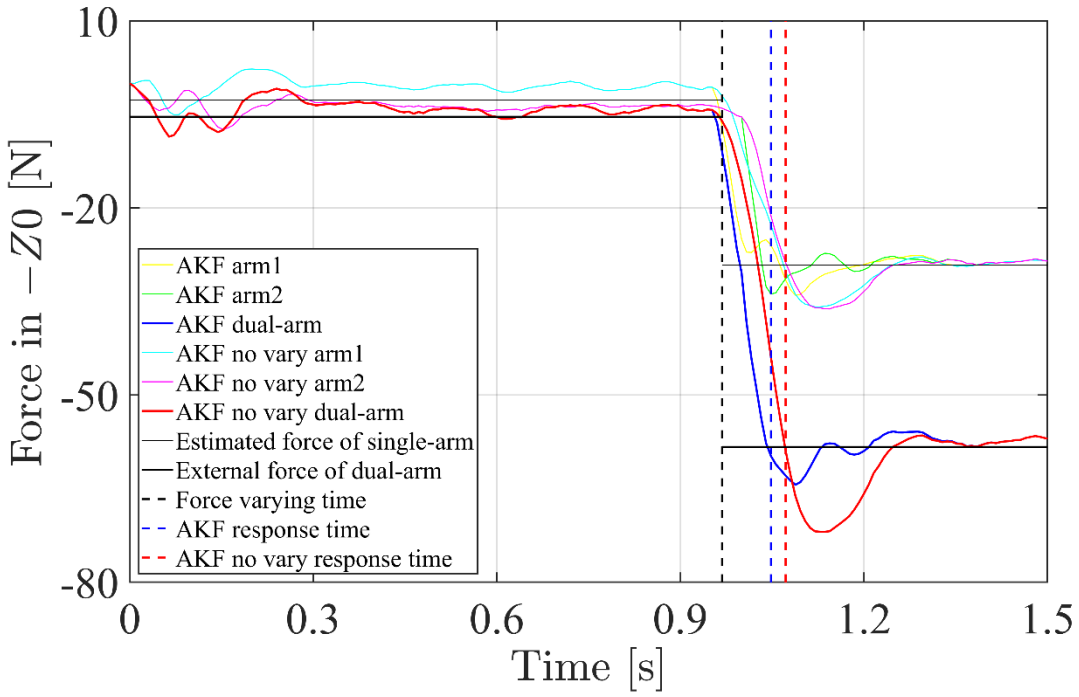

Fig. 8.6. Estimation of the force in -$Z0$ direction.

The RMSE of force estimation errors with two methods in Fig. 8.6 is concluded in Table 8-4 and it is divided into four periods. In the starting period (0-0.288 s), the HMA works. In the fixed-span period (0.288-0.968 s and 1.256-1.5 s), the WMA is employed. When external wrench is exerted on the manipulator and the time period is varying (0.968-1.256 s), the HMA is used. The only difference for the AKF no vary method is that the time period is fixed when the HMA is working during the period of 0.968-1.256 s.

Table 8-4 RMSE [N] of the force estimation errors in different periods

Time / Method	0-0.288 s	0.288-0.968 s	0.968-1.256 s	1.256-1.5 s
AKF	2.67**	0.68*	14.19**	0.74*
AKF no vary	2.67**	0.68*	22.32**	0.52 *

8.1.2. Discussion

In this chapter, the proposed AKF based on the MSMA with variable time period is discussed and its force/torque estimation performance on the decoupled system is validated.

a. Difference between the MSMA used for single-arm robot and that used for the dual-arm robot

Although the MSMA with HMA working in the period of varying span and WMA working in the period of fixed span leads to better performance in CFTE for single-arm robot, the converse phenomenon occurred when the proposed approach

was applied to dual-arm robot. Therefore, the MSMA employs the HMA at the start and in case of changing external wrench, and use the WMA when the time period is fixed.

b. Effect of the AKF

The proposed contact force/torque estimation method based on the AKF performs better in the dual-arm physical experiments compared to the peer CKF method [96]. The standard deviation of the force estimation based on two methods are shown in Fig. 8.3. The errors of estimation from the AKF were all smaller than those from the CKF. Hence, in cases similar to the experimental process, more accurate estimation of contact force is likely with the proposed AKF. The same conclusion can be made for torque estimation errors as the AKF error SD was lower than those of the CKF (Fig. 8.1 (b)). However, more torque estimation experiments with different payloads should be conducted to further validate the conclusion.

The RMSE of the estimation errors presented in Table 8-1 shows the CKF had a higher RMSE (1.76) than the AKF (0.81). However, the RMSE of the proposed method was worse (1.99 vs 2.36) during the initial period (0-0.288 s), and (16.05 vs 16.63) during these periods the HMA was active. However, the response time of the AKF was superior (0.184 vs 0.072 s). Therefore, the accuracy and response time must be balanced depending on the application scenario.

It can be seen from Fig. 8.2 that the AKF conducts apparently faster force estimation than the CKF throughout all payloads. The response time of torque estimation is not displayed in these experiments since the external exerted torques on both the single-arm and the dual-arm robots are supposed to be constant. Hence, a valid comparison is impossible. Furthermore, the magnitude of the ideal exerted torque is zero, because of which the advantage of torque-estimating response time is not apparent. An experimental test is required to validate if the response time advantages of the proposed AKF are likely to emerge in concert with the benefits in force estimation as the varying torque gets larger.

c. Effect of the switching mode, the HMA, the WMA, and the variable time period

The mechanism of mode switching, the involved moving averages, and the variable time period all contribute to the improved response time and estimation accuracy.

The smoothing effect of the WMA is better than that of the HMA when the time period is fixed and large. Fig. 8.4 shows the AKF based on the MSMA and the AKF based on only HMA. The performance of the MSMA is better in terms of reducing estimation errors, which can be concluded from 0.288 to 1.256 s and 1.256 to 1.5 s. During the period of span varying (0 to 0.288 s and 0.968 to 1.256 s), the MSMA and WMA only curves almost overlap each other. Furthermore, the RMSE of estimation errors is shown in Table 8-2. During the period of 0 to 0.288 s and 0.968 to 1.256 s, the estimation results of both methods are similar since only the HMA is active. However, the estimation errors are reduced dramatically with the proposed method since the time period is fixed and the WMA is working.

When a varying external wrench is exerted on the manipulator, the HMA needs less time to effectively recognize the load. As shown in Fig. 8.5, the response time resulting from the HMA are smaller than that resulting from the WMA when the time period is varied. Furthermore, the estimation errors of the HMA is also smaller than that of the WMA. As shown in Table 8-3, the RMSE of estimation error is reduced from 15.72 to 15.11. This is possible as the HMA is active in the period of 0.968-1.256 s with the proposed method. These benefits occurred across all payloads considered. Both the WMA and the HMA produced faster response times than the CKF.

Advantages of both moving average approaches are adopted in this research, the performance of which can be seen in Fig. 8.1(a). Time lag is ubiquitous with all non-predictive moving averages. Consequently, using any moving averages in a CFTE will lead to estimation lag. However, fast estimation is realized in this experiment for two reasons: Firstly, the smaller diagonal elements in the covariance matrix $\boldsymbol{\sigma}^2_{\mathrm{Dyn}}$ leads to a reduced response time for the system. The effect of the noise in the measured current is reduced by the mode-switching filter (both the HMA and the WMA) and thus the diagonal elements of $\boldsymbol{\sigma}^2_{\mathrm{Dyn}}$ are reduced. Secondly, the variable time period adapts quickly to large changes in the motor current and further reduces the response time.

d. Effect of the variable time period

The WMA and the HMA facilitate the application of the AKF and achieve improved estimation results in terms of response time and estimation accuracy. Furthermore, the variable time period further reduces the response time when interacting with the unexpected change in external force. As shown in Fig. 8.6, estimation results of the AKF based on MSMA with variable span and the counterpart without variable span are displayed. When the external wrench is applied to the UR5, the varying span approach is able to omit the previous current samples in each averaging step due to the variable time period. Consequently, the proposed approach leads to faster response. It can also be concluded from Table 8-4 that the RMSE time period is able to reduce estimation errors when the span is varying (0.968-1.256 s), and the RMSE is reduced from 22.32 to 14.19.

Noted that the RMSE in the period of 1.256-1.5 s (Table 8-4) is supposed to be the same for two methods, while the RMSE for the AKF is bigger than that for the AKF with a fixed span. The reason is the current samples from 0.968-1.256 s are still employed to calculate the estimated current samples at the start of the 1.256-1.5 s period. Thus the obtained currents in 1.256-1.5 s are derived from two methods. Anyway, during the experiment, the difference will become increasingly negligible. In the period of 0 – 0.968 s, the RMSE for two methods are the same since the same moving average is active.

e. Effect of tuning strategy of the proposed AKF

In order to calibrate the AKF, various tuning routines are proposed. The peer method [95] updates process and

measurement covariance matrices using the estimated information. In [96], uncertainty of the modelled joint driving torques is calculated and thus applied to calibrate the AKF. In contrast to these AKF approaches, the proposed approach measured system uncertainty by offline experiments (section 3.2) on the dual-arm robot. Furthermore, the real-time dynamic and kinematic information of the dual-arm robot is observed. Using these information, measurement covariance matrices are updated in each iterative step. Hence, better CFTE performance is achieved for the dual-arm robot as the approach is able to utilize measured values over a shorter timeframe upon recognition of an external wrench and can thus, determine the noise characteristics more precisely.

Moreover, tuning routines for the mode-switching moving averages were also considered in this research (section 4.4). Off-line-experiments-determined switching mechanism and the optimal varying time period provide an ability to optimize estimation accuracy and response time when dealing with unexpected loads.

f. Effect of the generalized-momentum-based model

Similar to the method of the CFTE for the single-arm robot, the proposed contact force estimation approach depends on the generalized-momentum-based model. Therefore, inversion of the manipulator inertia matrix is not required and the computational burden is reduced.

Furthermore, joint acceleration is not required with the proposed method, and therefore amplification of the measurement noise can be avoided. Uncertainty of the manipulator dynamics is overcome in the proposed approach as the noise in the measured current is taken into account and ultimately allows for definition of a more accurate Kalman filter gain. In addition, the physical implementation cost of the approach is lower than the similar Kalman filter based approaches [95] as it does not require additional force/torque sensors.

Moreover, as discussed in [123] and [124], the proposed method can be applied to not only the dual-arm robot but any robotic manipulators where the kinematic and dynamic information is accessible.

g. Overview of the AKF based on the MSMA

The proposed approach is validated in a dual-arm robotic system with variable loading scenarios. The validation used key parameters that are critical for the effective implementation of robotic manipulators – response time and force/torque estimation precision. The control system was not aware of the force/torque contact before occurrence nor the weight of the end effector payload. Use of a series of loading scenarios shows that parameters of the approach are not specifically tuned to succeed in limited range of applications.

Typically, the internal force and torque between two robotic arms occur as the dual-arm system operates. Consequently, a model of the interaction needed to be built before the proposed method could be applied to the physical experiment. However, parallel movements are conducted in this experiment for two manipulators and thus the dynamics can be

simplified as a model of the internal interaction is avoided in this research. In order to generalize the proposed method, the internal force and torque between two robotic manipulators must first be modelled.

Theoretically, the proposed method can be applied to robotic systems which consist of any number of robotic manipulators as long as the information of manipulator kinematics, manipulator dynamics, and motor feedbacks is available. However, this conclusion needs to be verified and validation of the generalization of the proposed method will be conducted on more manipulators.

9. CONCLUSION

In Chapter 1, the state of art of the contact force/torque estimation for serial industrial manipulator was presented. Motivation of sensorless CFTE for manipulators was clarified and objective of this research is introduced. Organization of the thesis was described. Kinematic models were built based on the Denavit-Hartenberg convention in Chapter 2 for both the single-arm robot and the dual-arm robot. With the kinematic models, Jacobians of the robots were determined. Based on the manipulator kinematics and Jacobians, dynamics of the robotic systems were expressed by the Euler-Lagrange equations.

The dynamic models based on Euler-Lagrange equations were modified into the format of the generalized momentum. Using models in the new format reduces calculation and observation burden in the CFTE. The generalized-momentum-based models are then discretized as state space equations, which could then be applied to the conventional Kalman filter.

Sensorless identification of the motor constant was accomplished based on the dynamic and kinematic parameters obtained from the manufacture in Chapter 3. With the motor information, a simplified joint friction model was built and applied to the Euler-Lagrange dynamics. The performance of the simplified model in the sensorless CFTE of the robotic systems was validated and discussed. Sensorless identification of the predicted state noise and the measurement noise was also presented in Chapter 3. With this information, the uncertainty in the Euler-Lagrange dynamics was determined and facilitated improvements in the performance of the sensorless CFTE. Analysis of these noise was also conducted.

Development of the adaptive Kalman filter was introduced in Chapter 4. The proposed AKF based on the weighted moving average with variable time period was presented and contrasted to some popular current methods. Calibration and application strategies of the AKF was introduced. A mode-switching moving average concept was also presented in Chapter 4. Determination of the moving averages was presented according to different application scenarios. With the MSMA, a different potential AKF strategies with variable time periods can be active estimators. The mode-switching algorithm of the pre-filter was presented. Calibrating strategies of the threshold value and time period of the pre-filter were clarified.

Experimental tests of the AKF based on the WMA with variable time period on the single-arm robot were performed in Chapter 5. Experiments were conducted with differing configurations. The method was test using different payloads, different speeds, and different orientations. Experimental results are summarized and analysed. Effects of the pre-filter, the current detecting mechanism, the variable time period, the generalized-momentum-based model, and the limitations of the approach were discussed. Critically, the proposed AKF yielded force and torque estimation that exceeded the performance of the current state-of-the-art methods.

Experimental tests of the AKF based on the MSMA with variable time period on the single-arm robot were performed

and presented in Chapter 6. Again, experiments were conducted in different scenarios. Experimental results are summarized and analysed. Effects of the WMA and the HMA, the mode switch mechanism, and the tuning method are discussed. Again, the proposed MSMA algorithm predicted force better than the comparator methods. Since, the MSMA incorporates the best elements of the moving averages presented in chapter 4, it also improved upon the performance presented in Chapter 5.

Experimental tests of the AKF based on the WMA with variable time period on the dual-arm robot were performed and presented in Chapter 7. The experimental results were summarized and analysed. Internal interaction between two manipulators and effects of the pre-filter were discussed. The performance of applying the method to the dual-arm robot is compared to that to the single-arm robot. Ultimately, the performance of the proposed approach exceed the performance of current methods.

The MSMA used in Chapter 8 is different from that in Chapter 5 (section 4.3.3.). Experiments of the AKF based on this MSMA with variable time period on the dual-arm robot were performed and presented in Chapter 8. Experimental results showed that the MSMA has potential to accurately estimate the external wrenches on dual arm arrangements. Furthermore, effects of the AKF, the switching mode, the HMA, the WMA, and the calibrating approach on the dual-arm robot are discussed.

All the physical experiments were conducted on UR5. The codes employed for commanding the UR5 and collecting robot data are summarized in Appendix A. The robot dynamics are modelled and experimental data are analysed using Matlab. The related codes are summarized in Appendix B.

10. FUTURE WORK

In future analysis, the proposed adaptive Kalman filters should be applied to different manipulators to validate their performance. In this research, the experimental tests were conducted on UR5 manipulators. However, the UR5 is a collaborative robot and the physical constitution is different from the traditional industrial manipulators with six degrees of freedom. In particular, servo motors or stepper motors are used for most current industrial serial robots [125]. Furthermore, harmonic reducers or RV (rotate vector) reducers are employed. Therefore, the dynamics uncertainty and measurement noise of UR5 joints may differ from that of the conventional manipulators when the proposed method is applied.

The proposed CFTE methods will be applied to more industrial scenarios. In Chapter 5 to Chapter 8, the proposed AKF were tested with the UR5 manipulators lifting a payload. However, force/torque feedback of the robotic manipulator is required in control strategies of more applications and orientations. For example, it has been hypothesized that force/torque control is necessary for improving the precision of robotic polishing or grinding tasks. Therefore, more complicated and challenging tests of the presented approach should be undertaken to validate the generality.

A neural network approach will be employed to build a more general friction model. In this research, a simplified friction model was employed in order to simplify the system dynamics. Consequently, the joint speeds were limited within certain ranges to ensure the effectiveness of the friction model. However, joint velocity cannot be predicted in the real applications. Furthermore, the joint friction is also affected by the temperature and payload, which are ignored in this thesis. Therefore, a more comprehensive friction model should be designed and parameterized via a neural network optimization.

The potential for the method to be used in the risk mitigation for attendant human operators will be investigated. Cooperation of these robots with human operators requires that the emergency stop can be activated if the robot is in expected contact with human or external environment. To achieve that goal, the CFTE method must recognize whether the accidental contact or the expected external wrench is exerted. Such discrimination is an important but nontrivial task.

A model to predict the internal interaction of two manipulators will be built. In this thesis, two robotic arms conducted mirrored motions in order to avoid the internal interaction between two arms. However, dual arm robots often yield imperfect coordination in the real case. For example, internal force/torque will occur if two arms conducted different uncoordinated motions in Chapter 7, and thus the proposed method may fail since the model of the internal interaction is ignored. Consequently, CFTE experiments with two manipulators moving with different motions will be conducted and the estimation results will be analysed.

In Chapter 3, sensorless identification of the dynamics and system uncertainty is conducted. Although better estimation results (compared to peer method) were obtained in Chapter 5 to Chapter 8 with these identified parameters, more accurate

identification using the physical sensors will be considered in the future. The sensorless identified results will be analysed and compared to that received with sensors.

APPENDIX A: PYTHON CODES

Appendix A1

```
import datetime
import time
import socket
import struct
import collections


TIMEOUT_SAMPLES = 5 # How many missed samples should count as a timeout?
TIMEOUT_RESET = 1 # How many seconds until the timeout counter is reset.
TIMEOUT_MAX = 5 # How many timeouts before a connection reset?

RATE = {30001:10,
        30002:10,
        30003:125,
        30004:125}

VECTOR_6F = 'd'*6

DATA_TYPES = collections.OrderedDict([
    ('Message Size', 'i'),
    ('Time', 'd'), # [s]
    ('q target', VECTOR_6F),
    ('qd target', VECTOR_6F),
    ('qdd target', VECTOR_6F),
    ('I target', VECTOR_6F),
    ('M target', VECTOR_6F),
    ('q actual', VECTOR_6F), # [rad,rad,rad,rad,rad,rad]
    ('qd actual', VECTOR_6F),
    ('I actual', VECTOR_6F),
    ('Tool Accelerometer data', 'd'*3),
    ('RTC_Unused', 'd'*15),
    ('TCP force', VECTOR_6F),
    ('Tool vector', VECTOR_6F), # [m,m,m,rad,rad,rad]
    ('TCP speed', VECTOR_6F),
    ('Digital input bits', 'd'),
    ('Motor temperatures', VECTOR_6F),
    ('Controller Timer', 'd'),
    ('Test value', 'd'),
    ('Robot Mode', 'd'),
    ('Joint Modes', VECTOR_6F)])

class RTC:
    def __init__(self, host, port=30003):
        self.host = host
        self.port = port
        self.timeoutcount = 0
```

```
47.         self.timeoutlast = time.time()
48.         self.data = dict()
49.         self.msgSizeMin = struct.calcsize(DATA_TYPES['Message Size'])
50.
51.     def connect(self):
52.         self.socket = socket.socket(socket.AF_INET, socket.SOCK_STREAM)
53.         self.socket.connect((self.host, self.port))
54.         self.socket.settimeout(TIMEOUT_SAMPLES / RATE[self.port])
55.         self.buffer = bytearray()
56.         print('Connected')
57.
58.     def disconnect(self):
59.         self.socket.close()
60.         print('Disconnected')
61.
62.
63.     def read(self, writer):
64.         try:
65.             self.buffer += self.socket.recv(1024)
66.         except socket.timeout:
67.             print('Timeout')
68.             now = time.time()
69.             if (now - self.timeoutlast) > TIMEOUT_RESET:
70.                 self.timeoutcount = 0
71.                 self.timeoutlast = now
72.             self.timeoutcount += 1
73.             if self.timeoutcount >= TIMEOUT_MAX:
74.                 print('Max timeouts reached')
75.                 self.disconnect()
76.                 self.connect()
77.                 self.timeoutcount = 0
78.                 return(0)
79.
80.         packetsRead = 0
81.         packetsAvailable = len(self.buffer) >= self.msgSizeMin
82.
83.         while packetsAvailable:
84.             i = 0
85.             for name in DATA_TYPES.keys():
86.                 if name == 'Message Size':
87.                     self.timestamp = datetime.datetime.now()
88.                 fmt = DATA_TYPES[name]
89.                 value = struct.unpack_from('>'+fmt, self.buffer, i)
90.
91.                 if len(fmt) == 1:
92.                     value = value[0]
93.                 if i == 0:
94.                     msgSize = value
95.                     packetsAvailable = len(self.buffer) >= msgSize
96.                     if packetsAvailable:
97.                         pass#print()
```

```
98.                     else:
99.                         return(packetsRead)
100.
101.                self.data[name] = value
102.                #print(name + ':\t' + str(value))
103.                i += struct.calcsize(fmt)
104.
105.            self.buffer = self.buffer[msgSize:]
106.            packetsAvailable = len(self.buffer) >= self.msgSizeMin
107.            writer()
108.            packetsRead += 1
109.        return(packetsRead)
```

Appendix A2

```
import realtimeclient

robot = realtimeclient.RTC("132.181.60.76")
robot.connect()
f = open('experiment.xlsx', 'w')

def record_fun():
    f.write(str(robot.data['Time']))
    f.write(',!!!!')
    f.write(str(robot.timestamp))


    for i in range(6):
        f.write(',')
        f.write(str(robot.data['q actual'][i]))
    for i in range(6):
        f.write(',')
        f.write(str(robot.data['qd actual'][i]))
    for i in range(6):
        f.write(',')
        f.write(str(robot.data['I actual'][i]))


    for i in range(6):
        f.write(',')
        f.write(str(robot.data['q target'][i]))
    for i in range(6):
        f.write(',')
        f.write(str(robot.data['qd target'][i]))
    for i in range(6):
        f.write(',')
        f.write(str(robot.data['I target'][i]))
    for i in range(6):
        f.write(',')
        f.write(str(robot.data['qdd target'][i]))

    f.write('\n')

try:
    while True:
        robot.read(record_fun)


except (KeyboardInterrupt, SystemExit):
    f.close()
    robot.disconnect()
```

Appendix A3

```
import socket
import time


PORT = {30001: 'PRIMARY_CLIENT',
        30002: 'SECONDARY_CLIENT',
        30003: 'REAL_TIME_CLIENT',
        30004: 'REAL_TIME_DATA_EXCHANGE'}

'''
DATA_TYPES = collections.OrderedDict([
    ('packageSize', 'i'),
    ('packageType', 'B'),
    ('timestamp', 'Q'),
    ('isRobotConnected', '?'),
    ('isRealRobotEnabled', '?'),
    ('isPowerOnRobot', '?'),
    ('isEmergencyStopped', '?'),
    ('isProtectiveStopped', '?'),
    ('isProgramRunning', '?'),
    ('isProgramPaused', '?'),
    ('robotMode', 'B'),
    ('controlMode', 'B'),
    ('targetSpeedFraction', 'd'),
    ('speedScaling', 'd'),
    ('targetSpeedFractionLimit', 'd')])
'''

class UR5:
    def __init__(self, host, port, wait=3):
        self.host = host
        self.port = port
        if not(port in PORT.keys()):
            print('Unsupported port.')
        self.socket = socket.socket(socket.AF_INET, socket.SOCK_STREAM)
        self.wait = wait

    def connect(self):
        self.buffer = bytearray()
        self.socket.connect((self.host, self.port))

    def disconnect(self):
        self.socket.close()

    def send(self, command):
        ur_cmd = command.strip('\n\r') + '\n'
        self.socket.send(ur_cmd.encode())
        print("Sending: " + command + '\n')
```

```
50.         time.sleep(self.wait)
51.
52.     def receive(self):
53.         self.buffer += self.socket.recv(1024)
54.         return self.buffer
55.
56.     def set_tool_voltage(self, volts):
57.         volts = max(volts, 0)
58.         volts = min(volts, 24)
59.         volts = 12*round(volts/12)
60.         self.send("set_tool_voltage({})".format(volts))
61.
62.     def set_payload(self, mass):
63.         mass = max(mass, 0)
64.         self.send("set_payload({})".format(mass))
65.
66.     def set_gravity(self, d):
67.         self.send("set_gravity({})".format(d))
68.
69.     def movej(self, q, a=3, v=0.75, t=0, r=0):
70.         self.send("movej({},{},{},{},{})".format(q,a,v,t,r))
71.
72.     def movel(self, p, a, v,t,r):
73.         self.send("movel({},{},{},{},{})".format(p,a,v,t,r))
74.
75.     def speedj(self, qd, a, t_min):
76.         self.send("speedj({},{},{})".format(qd,a,t_min))
77.
78.     def speedl(self, xd, a, t_min):
79.         self.send("speedl({},{},{})".format(xd,a,t_min))
80.
81.     def stopj(self, a):
82.         self.send("stopj({})".format(a))
83.
84.     def stopl(self, a):
85.         self.send("stopl({})".format(a))
86.
87.     def set_digital_out(self, n, b):
88.         self.send("set_digital_out({},{})".format(n,b))
89.
90.     def get_actual_joint_speeds(self):
91.         self.send("get_actual_joint_speeds()")
92.
93.     def get_target_payload(self):
94.         self.send("get_target_payload()")
```

Appendix A4

```
2. import ur5
3. from math import pi
4. import time
5.
6. HOST = "132.181.60.76"    # Robot's IP address.
7. PORT = 30002            # Port used for standard communications.
8.
9.
10.robot = ur5.UR5(HOST, PORT)
11.robot.connect()
12.time.sleep(1)
13.
14.DEG_TO_RAD = pi/180
15.Q_HOME = [90,-46,70,-24,90,-220]
16.robot.movej([DEG_TO_RAD*x for x in Q_HOME])
17.time.sleep(70)
18.
19.
20.xd =[0,0,0.06,0,0,0]
21.robot.speedl(xd,0.24,3)
22.time.sleep(5)
23.
24.
25.robot.disconnect()
26.input("Press any key to close.")
```

Appendix A5

```
import realtimeclient

robot = realtimeclient.RTC("192.168.1.1")
robot2 = realtimeclient.RTC("192.168.1.2")

robot.connect()
robot2.connect()

f = open('1800g1.csv', 'w')
f2 = open('1800g2.csv', 'w')

def record_fun1():
    f.write(str(robot.data['Time']))
    f.write(',!!!!')
    f.write(str(robot.timestamp))


    for i in range(6):
        f.write(',')
        f.write(str(robot.data['q actual'][i]))
    for i in range(6):
        f.write(',')
        f.write(str(robot.data['qd actual'][i]))
    for i in range(6):
        f.write(',')
        f.write(str(robot.data['I actual'][i]))


    for i in range(6):
        f.write(',')
        f.write(str(robot.data['q target'][i]))
    for i in range(6):
        f.write(',')
        f.write(str(robot.data['qd target'][i]))
    for i in range(6):
        f.write(',')
        f.write(str(robot.data['I target'][i]))
    for i in range(6):
        f.write(',')
        f.write(str(robot.data['qdd target'][i]))

    f.write('\n')

def record_fun2():
    f2.write(str(robot2.data['Time']))
    f2.write(',!!!!')
    f2.write(str(robot2.timestamp))

```

```
50.
51.     for i in range(6):
52.         f2.write(',')
53.         f2.write(str(robot2.data['q actual'][i]))
54.     for i in range(6):
55.         f2.write(',')
56.         f2.write(str(robot2.data['qd actual'][i]))
57.     for i in range(6):
58.         f2.write(',')
59.         f2.write(str(robot2.data['I actual'][i]))
60.
61.
62.
63.     for i in range(6):
64.         f2.write(',')
65.         f2.write(str(robot2.data['q target'][i]))
66.     for i in range(6):
67.         f2.write(',')
68.         f2.write(str(robot2.data['qd target'][i]))
69.     for i in range(6):
70.         f2.write(',')
71.         f2.write(str(robot2.data['I target'][i]))
72.     for i in range(6):
73.         f2.write(',')
74.         f2.write(str(robot2.data['qdd target'][i]))
75.
76.     f2.write('\n')
77.
78. try:
79.     while True:
80.         robot.read(record_fun1)
81.         robot2.read(record_fun2)
82.
83.
84. except (KeyboardInterrupt, SystemExit):
85.     f.close()
86.     f2.close()
87.     robot.disconnect()
88.     robot2.disconnect()
```

Appendix A6

```
import ur5
from math import pi
import time

HOST1 = "192.168.1.1"    # Robot1's IP address.
PORT1 = 30003            # Port1 used for standard communications.

HOST2 = "192.168.1.2"    # Robot2's IP address.
PORT2 = 30003            # Port2 used for standard communications.

robot1 = ur5.UR5(HOST1, PORT1)
robot1.connect()
time.sleep(1)

robot2 = ur5.UR5(HOST2, PORT2)
robot2.connect()
time.sleep(1)

DEG_TO_RAD = pi/180

Q_HOME1 = [180,-113,-105,-52,90,0]
Q_HOME2 = [180,-67,105,-128,-90,0]

robot1.movej([DEG_TO_RAD*x for x in Q_HOME1])
robot2.movej([DEG_TO_RAD*x for x in Q_HOME2])
time.sleep(10)

xd =[0,0,0.06,0,0,0]
robot1.speedl(xd,0.24,3)
robot2.speedl(xd,0.24,3)
time.sleep(5)

xd =[0,0,-0.06,0,0,0]
robot1.speedl(xd,-0.24,3)
robot2.speedl(xd,-0.24,3)
time.sleep(5)

robot1.disconnect()
robot2.disconnect()
input("Press any key to close.")
```

APPENDIX B: THE MATLAB CODES

Appendix B1

```
clear;
clc;

global M;
global P;

global theta1 theta2 theta3 theta4 theta5 theta6;

global dtheta1 dtheta2 dtheta3 dtheta4 dtheta5 dtheta6;

global ddtheta1 ddtheta2 ddtheta3 ddtheta4 ddtheta5 ddtheta6;

global tauext;

global tauf1 tauf2 tauf3 tauf4 tauf5 tauf6;
global taum1 taum2 taum3 taum4 taum5 taum6;
global miuv1 miuv2 miuv3 miuv4 miuv5 miuv6;
global miuc1 miuc2 miuc3 miuc4 miuc5 miuc6;
global taun1 taun2 taun3 taun4 taun5 taun6;

global sf1 sf2 sf3 sf4 sf5 sf6;

global J6;
global Ja3;
global MM3;
syms alpha0 a0 theta1 d1
syms alpha1 a1 theta2 d2
syms alpha2 a2 theta3 d3
syms alpha3 a3 theta4 d4
syms alpha4 a4 theta5 d5
syms alpha5 a5 theta6 d6

% centroid of link i expressed in coordinates i
syms x1 y1 z1
syms x2 y2 z2
syms x3 y3 z3
syms x4 y4 z4
syms x5 y5 z5
syms x6 y6 z6

syms m1 m2 m3 m4 m5 m6 g

%Angle, angular velocity and angular acceleration
syms theta1 theta2 theta3 theta4 theta5 theta6
syms dtheta1 dtheta2 dtheta3 dtheta4 dtheta5 dtheta6
syms ddtheta1 ddtheta2 ddtheta3 ddtheta4 ddtheta5 ddtheta6
```

```
syms M M1 M2 M3 M4 M5 M6
syms fx fy fx nx ny nz

g = sym(-9.81);

theta =  [theta1;  theta2;  theta3;  theta4;  theta5;  theta6];
dtheta = [dtheta1; dtheta2; dtheta3; dtheta4; dtheta5; dtheta6];

% inertial tensor of link i expressed in the coordinates whose
% origin is located at the centroid of link i

Ic1=[0.0084 0 0; 0 0.0084 0; 0 0 0.0064];
Ic2=[0.0078 0 0; 0 0.2100 0; 0 0 0.2100];
Ic3=[0.0016 0 0; 0 0.0462 0; 0 0 0.0462];
Ic4=[0.0016 0 0; 0 0.0009 0; 0 0 0.0016];
Ic5=[0.0016 0 0; 0 0.0009 0; 0 0 0.0016];
Ic6=[0.0001 0 0; 0 0.0001 0; 0 0 0.0001];
% Ic6=[0.0016 0 0; 0 0.0009 0; 0 0 0.0016];

%UR5 parameters
d1 = sym(0.08916);    d2 = sym(0);          d3 = sym(0);
d4 = sym(0.10915);    d5 = sym(0.09465);    d6 = sym(0.0823);
a0 = sym(0);          a1 = sym(0);          a2 = sym(-0.425);
a3 = sym(-0.39225);    a4 = sym(0);          a5 = sym(0);
alpha0 = sym(0);      alpha1 = sym(pi/2);   alpha2 = sym(0);
alpha3 = sym(0);      alpha4 = sym(pi/2);   alpha5 = sym(-pi/2);
m1 = 3.7;             m2 = 8.393;           m3 = 2.33;
m4 = 1.219;           m5 = 1.219;           m6 = 0.1879;

T01 = Trans(alpha0, a0, theta1, d1);
T12 = Trans(alpha1, a1, theta2, d2);
T23 = Trans(alpha2, a2, theta3, d3);
T34 = Trans(alpha3, a3, theta4, d4);
T45 = Trans(alpha4, a4, theta5, d5);
T56 = Trans(alpha5, a5, theta6, d6);

T00 = [1 0 0 0; 0 1 0 0; 0 0 1 0; 0 0 0 1];
T01 = T01;
T02 = T01 * T12;
T03 = T01 * T12 * T23;
T04 = T01 * T12 * T23 * T34;
T05 = T01 * T12 * T23 * T34 * T45;
T06 = T01 * T12 * T23 * T34 * T45 * T56;

% centroid of link 1 to 6 expressed in coordinate 0
c1 = [1, 0, 0, 0; 0, 1, 0, -0.00193; 0, 0, 1, -0.02561; 0 0 0 1];
T0c1 = T01 * c1;
c2 = [1, 0, 0, -0.2125; 0, 1, 0, 0; 0, 0, 1, 0.11336; 0 0 0 1];
T0c2 = T02 * c2;
c3 = [1, 0, 0, -0.24225; 0, 1, 0, 0; 0, 0, 1, 0.0265; 0 0 0 1];
T0c3 = T03 * c3;
```

```
c4 = [1, 0, 0, 0; 0, 1, 0, -0.01634; 0, 0, 1, -0.0018; 0 0 0 1];
T0c4 = T04 * c4;
c5 = [1, 0, 0, 0; 0, 1, 0, 0.01634; 0, 0, 1, -0.0018; 0 0 0 1];
T0c5 = T05 * c5;
c6 = [1, 0, 0, 0; 0, 1, 0, 0; 0, 0, 1, -0.001159; 0 0 0 1];
T0c6 = T06 * c6;

B = [0; 0; 0];

%Z axes of coordinate 0 to 6 expressed in coordinate 0
Z0 = T00([1 2 3], 3);
Z1 = T01([1 2 3], 3);
Z2 = T02([1 2 3], 3);
Z3 = T03([1 2 3], 3);
Z4 = T04([1 2 3], 3);
Z5 = T05([1 2 3], 3);
Z6 = T06([1 2 3], 3);

%Origin of coordinate 0 to 6 expressed in coordinate 0
o0 = T00([1 2 3], 4);
o1 = T01([1 2 3], 4);
o2 = T02([1 2 3], 4);
o3 = T03([1 2 3], 4);
o4 = T04([1 2 3], 4);
o5 = T05([1 2 3], 4);
o6 = T06([1 2 3], 4);

%Centroid of link 1 to 6 expressed in coordinate 0
oc1 = T0c1([1 2 3], 4);
oc2 = T0c2([1 2 3], 4);
oc3 = T0c3([1 2 3], 4);
oc4 = T0c4([1 2 3], 4);
oc5 = T0c5([1 2 3], 4);
oc6 = T0c6([1 2 3], 4);

%Jacobian of centroid of link 1
JV1_1 = cross(Z1, oc1-o1);
J1 = [JV1_1, B, B, B, B, B; Z1, B, B, B, B, B];
Jv1 = J1([1 2 3], :);
Jw1 = J1([4 5 6], :);

%Jacobian of centroid of link 2
JV2_1 = cross(Z1, oc2-o1);
JV2_2 = cross(Z2, oc2-o2);
J2 = [JV2_1, JV2_2, B, B, B, B; Z1, Z2, B, B, B, B];
Jv2 = J2([1 2 3], :);
Jw2 = J2([4 5 6], :);

%Jacobian of centroid of link 3
JV3_1 = cross(Z1, oc3-o1);
JV3_2 = cross(Z2, oc3-o2);
```

```
JV3_3 = cross(Z3, oc3-o3);
J3 = [JV3_1, JV3_2, JV3_3, B, B, B;Z1, Z2, Z3, B, B, B];
Jv3 = J3([1 2 3], :);
Jw3 = J3([4 5 6], :);

%Jacobian of centroid of link 4
JV4_1 = cross(Z1, oc4-o1);
JV4_2 = cross(Z2, oc4-o2);
JV4_3 = cross(Z3, oc4-o3);
JV4_4 = cross(Z4, oc4-o4);
J4 = [JV4_1, JV4_2, JV4_3, JV4_4, B, B;Z1, Z2, Z3, Z4, B, B];
Jv4 = J4([1 2 3], :);
Jw4 = J4([4 5 6], :);

%Jacobian of centroid of link 5
JV5_1 = cross(Z1, oc5-o1);
JV5_2 = cross(Z2, oc5-o2);
JV5_3 = cross(Z3, oc5-o3);
JV5_4 = cross(Z4, oc5-o4);
JV5_5 = cross(Z5, oc5-o5);
J5 = [JV5_1, JV5_2, JV5_3, JV5_4, JV5_5, B;Z1, Z2, Z3, Z4, Z5, B];
Jv5 = J5([1 2 3], :);
Jw5 = J5([4 5 6], :);

%Jacobian of centroid of link 6
JV6_1 = cross(Z1, oc6-o1);
JV6_2 = cross(Z2, oc6-o2);
JV6_3 = cross(Z3, oc6-o3);
JV6_4 = cross(Z4, oc6-o4);
JV6_5 = cross(Z5, oc6-o5);
JV6_6 = cross(Z6, oc6-o6);
J6 = [JV6_1, JV6_2, JV6_3, JV6_4, JV6_5, JV6_6;Z1, Z2, Z3, Z4, Z5, Z6];
Jv6 = J6([1 2 3], :);
Jw6 = J6([4 5 6], :);

R0c1 = T0c1([1 2 3], [1 2 3]);
R0c2 = T0c2([1 2 3], [1 2 3]);
R0c3 = T0c3([1 2 3], [1 2 3]);
R0c4 = T0c4([1 2 3], [1 2 3]);
R0c5 = T0c5([1 2 3], [1 2 3]);
R0c6 = T0c6([1 2 3], [1 2 3]);

%kinetic energy
M1 = m1.* (Jv1.' * Jv1) + Jw1.' * (R0c1 * Ic1 * R0c1.') * Jw1;
M2 = m2.* (Jv2.' * Jv2) + Jw2.' * (R0c2 * Ic2 * R0c2.') * Jw2;
M3 = m3.* (Jv3.' * Jv3) + Jw3.' * (R0c3 * Ic3 * R0c3.') * Jw3;
M4 = m4.* (Jv4.' * Jv4) + Jw4.' * (R0c4 * Ic4 * R0c4.') * Jw4;
M5 = m5.* (Jv5.' * Jv5) + Jw5.' * (R0c5 * Ic5 * R0c5.') * Jw5;
M6 = m6.* (Jv6.' * Jv6) + Jw6.' * (R0c6 * Ic6 * R0c6.') * Jw6;

M = M1 + M2 + M3 + M4 + M5 + M6;
```

```
200.
201.P01 = T0c1([1 2 3],[4]);
202.P02 = T0c2([1 2 3],[4]);
203.P03 = T0c3([1 2 3],[4]);
204.P04 = T0c4([1 2 3],[4]);
205.P05 = T0c5([1 2 3],[4]);
206.P06 = T0c6([1 2 3],[4]);
207.
208.P = m1 * g * P01(3, 1) + m2 * g * P02(3, 1) + m3 * g * P03(3, 1) +  m4 * g *
   P04(3, 1) +  m5 * g * P05(3, 1) +  m6 * g * P06(3, 1);
```

```
clc
clear

global tt;
A = xlsread('D:\experiment.xlsx');

B  = size(A);
length = B(1,1);
T2 = 19;
aa=1:1:length;

hold on
grid on

joint = 17;
tt = A(1:length,joint);
plot(aa,tt(1:length,1),'k','linewidth',1.5);
i=2;
while i<= T2
        WMA(i,i);
        A(i,joint)=WMA(i,i);
        i=i+1;
end
while i<=length
    if abs(A(i,joint)- A(i-1,joint))<= 0.47
        A(i,joint)=WMA(i,T2);
        i=i+1;
    else
        old = i
        222
        newT2=i+T2-2;
        WMA(i,T2);
        i=i+1;
        while i <=newT2
            WMA(i,i-old+1);
            A(i,joint)=WMA(i,i-old+1);
            i=i+1;
        end
    end
end
plot(aa,A(1:length,joint),'r','linewidth',1.5);

xlswrite('D:\experiment.xlsx',A,'Sheet1','A1');
```

Appendix B3

```
function f = Coriolis(k)

s= 0;
global dtheta1;
global dtheta2;
global dtheta3;
global dtheta4;
global dtheta5;
global dtheta6;
 for i=1:6
    for j=1:6
     s = s + christoffel(i,j,k)*eval(['dtheta' num2str(i)])*eval(['dtheta' num2str(j)]);
    end
 end
f = s;
end
```

Appendix B4

```
function f = christoffel(i,j,k)
syms s

global M;
global theta1;
global theta2;
global theta3;
global theta4;
global theta5;
global theta6;

s = diff(M(k,j),eval(['theta' num2str(i)]))+diff(M(k,i),eval(['theta' num2str(j)]))-diff(M(i,j),eval(['theta' num2str(k)]));

f = 0.5 * s;
end
```

Appendix B5

```
function f = gravity(k)

global P;
global theta1;
global theta2;
global theta3;
global theta4;
global theta5;
global theta6;

f = diff(P,eval(['theta' num2str(k)]));
end
```

Appendix B6

```
function [ T ] = Trans( alpha, a, theta, d)
T = [            cos(theta)           -sin(theta)           0             a;
      sin(theta)*cos(alpha) cos(theta)*cos(alpha) -sin(alpha) -sin(alpha)*d;
      sin(theta)*sin(alpha) cos(theta)*sin(alpha)  cos(alpha)  cos(alpha)*d;
                          0                     0           0             1];
end
```

Appendix B7

```
clc
clear

global tt;
A = xlsread('D:\experiment.xlsx');
B  = size(A);
length = B(1,1);
T = 49;
TT = 49;
aa=1:1:length;

joint = 17;
tt = A(1:length,joint);
hold on
grid on

tt = A(1:length,joint);
plot(aa,tt(1:length,1),'k','linewidth',1.5);
i=2;
while i<= T
        HMA(i,i);
        A(i,joint)=WMA(i,1,i);
        i=i+1;
end
while i<=length
    if i ~= 72
        A(i,joint)=HMA(i,T);
        i=i+1;
    else
        old = i
        222
        newTT=i+T-2;
        HMA(i,T);
        i=i+1;
        while i <=newTT
            HMA(i,i-old+1);
            A(i,joint)=WMA(i,1,i-old+1);
            i=i+1;
        end
    end
end
plot(aa,A(1:length,joint),'r','linewidth',1.5);

```

Appendix B8

```
global M;

global theta1 theta2 theta3 theta4 theta5 theta6;

global J6;

A_1 = xlsread('D:\dualarm_experiment1.xls');%KF WMA
A_2 = xlsread('D:\dualarm_experiment2.xls');%KF WMA
Qcf     = diag([1500,1500,1500,1500,1500,1500]);%KF WMA
Qcp_1   = diag([0,0.6,0.26,0.03,0,0]);%KF WMA
Qcp_2   = diag([0,0.34,0.28,0.04,0,0]);%KF WMA

i     = 1;
Bc    = eye(12,6);
Cc    = eye(6,12);

Mc_1    = diag([0,12.932,12.6,13,0,0]);%motor1 constant
Mc_2    = diag([0,12.9,12.7,13,0,0]);%motor2 constant
x_1     = [0;0;0;0;0;0;0;0;0;0;0;0];
x_2     = [0;0;0;0;0;0;0;0;0;0;0;0];


Qc_1    = [Qcp_1 zeros(6,6);zeros(6,6) Qcf];
Qc_2    = [Qcp_2 zeros(6,6);zeros(6,6) Qcf];

data_1  = [];
data_2  = [];
data_3  = [];

p_1     = eye(12,12);
p_2     = eye(12,12);

fri1_1  = diag([0,-0.8207,-1.495,-0.4154,0,0]);
fri1_2  = [0;0.6996;0.71325;0.1577;0;0];

fri2_1  = diag([0,-0.5474,-0.9978,-0.4287,0,0]);%??
fri2_2  = [0;0.6564;0.572;0.1658;0;0];

while i <= 201
    q_1     = [pi, A_1(i,4:6), pi/2, 0];
    q_2     = [pi, A_2(i,4:6), -pi/2, 0];
    qd_1    = [0, A_1(i,10:12), 0, 0];
    qd_2    = [0, A_2(i,10:12), 0, 0];
    m_1     = vpa(subs(M,{theta1,theta2,theta3,theta4,theta5,theta6},{q_1}));
    m_2     = vpa(subs(M,{theta1,theta2,theta3,theta4,theta5,theta6},{q_2}));
    Rc_1    = m_1*diag([0,0.000003,0.000002,0.000005,0,0])*transpose(m_1);
    Rc_2    = m_2*diag([0,0.000003,0.000002,0.000005,0,0])*transpose(m_2);
    R_1     = double(Rc_1/0.008);
    R_2     = double(Rc_2/0.008);
```

```
50.
51.     cd      = zeros(6,1);
52.
53.     gra_1   = vpa(subs([0;gravity(2);gravity(3);gravity(4);0;0],{theta1,theta2
    ,theta3,theta4,theta5,theta6},{q_1}));
54.     gra_2   = vpa(subs([0;gravity(2);gravity(3);gravity(4);0;0],{theta1,theta2
    ,theta3,theta4,theta5,theta6},{q_2}));
55.
56.     u_1     = -
    Mc_1*transpose([0  A_1(i,16:18) 0 0]) + cd - gra_1 - Mc_1*(fri1_1*transpose(qd
    _1)+diag([0,-sign(qd_1(1,2)),-sign(qd_1(1,3)),-sign(qd_1(1,4)),0,0])*fri1_2);
57.     u_2     = -
    Mc_2*transpose([0  A_2(i,16:18) 0 0]) + cd - gra_2 - Mc_2*(fri2_1*transpose(qd
    _2)+diag([0,-sign(qd_2(1,2)),-sign(qd_2(1,3)),-sign(qd_2(1,4)),0,0])*fri2_2);
58.
59.     Jaco_1    = vpa(-
    transpose(subs(J6,{theta1,theta2,theta3,theta4,theta5,theta6},{q_1})));
60.     Jaco_2    = vpa(-
    transpose(subs(J6,{theta1,theta2,theta3,theta4,theta5,theta6},{q_2})));
61.
62.     Ac_1      = double([zeros(6,6) Jaco_1; zeros(6,6)  zeros(6,6)]);
63.     Ac_2      = double([zeros(6,6) Jaco_2; zeros(6,6)  zeros(6,6)]);
64.
65.     [Ak_1,Bk_1] = c2d(Ac_1,Bc,0.008);
66.     [Ak_2,Bk_2] = c2d(Ac_2,Bc,0.008);
67.
68.     GUO_1     = expm([-transpose(Ac_1) Qc_1; zeros(12,12) Ac_1]*0.008);
69.     GUO_2     = expm([-transpose(Ac_2) Qc_2; zeros(12,12) Ac_2]*0.008);
70.
71.     M22_1     = GUO_1(13:24,13:24);
72.     M12_1     = GUO_1(1:12,13:24);
73.     M22_2     = GUO_2(13:24,13:24);
74.     M12_2     = GUO_2(1:12,13:24);
75.
76.     Q_1       = transpose(M22_1)*M12_1;
77.     Q_2       = transpose(M22_2)*M12_2;
78.
79.     xp_1      = Ak_1*x_1 + Bk_1*u_1;
80.     xp_2      = Ak_2*x_2 + Bk_2*u_2;
81.
82.     pp_1      = Ak_1*p_1*transpose(Ak_1)+Q_1;
83.     pp_2      = Ak_2*p_2*transpose(Ak_2)+Q_2;
84.
85.     aaa_1     = pp_1*transpose(Cc);
86.     bb_1      = Cc*pp_1;
87.     bbb_1     = bb_1*transpose(Cc);
88.     bbbb_1    = double(bbb_1+R_1);
89.
90.     aaa_2     = pp_2*transpose(Cc);
91.     bb_2      = Cc*pp_2;
92.     bbb_2     = bb_2*transpose(Cc);
```

```
93.     bbbb_2     = double(bbb_2+R_2);
94.
95.     K_1        = aaa_1/bbbb_1;
96.     K_2        = aaa_2/bbbb_2;
97.
98.     Y_1        = m_1*transpose(qd_1)+[0;0.000003;0.000002;0.000005;0;0];
99.     Y_2        = m_2*transpose(qd_2)+[0;0.000003;0.000002;0.000005;0;0];
100.
101.     x_1        = xp_1 + K_1*[Y_1-Cc*xp_1];
102.     x_2        = xp_2 + K_2*[Y_2-Cc*xp_2];
103.     x_1        = [x_1(1:6,1); x_1(7,1); 0; x_1(9:10,1); 0; 0];
104.     x_2        = [x_2(1:6,1); x_2(7,1); 0; x_2(9:10,1); 0; 0];
105.     x_3        = x_1 + x_2;
106.
107.     p_1        = (eye(12,12)-K_1*Cc)*pp_1;
108.     p_2        = (eye(12,12)-K_2*Cc)*pp_2;
109.
110.     data_1(i,1:6) = x_1(7:12,1);
111.     data_2(i,1:6) = x_2(7:12,1);
112.     data_3(i,1:6) = x_3(7:12,1);
113.
114.end
```

REFERENCE

[1] Smith, C., Karayiannidis, Y., Nalpantidis, L., Gratal, X., Qi, P., Dimarogonas, D. V., & Kragic, D. (2012). Dual arm manipulation—A survey. *Robotics and Autonomous systems*, 60(10), 1340-1353.

[2] https://phys.org/news/2020-04-additions-resource-industry-underwater-robots.html

[3] https://www.robots.com/articles/arc-welding-101

[4] https://www.therobotreport.com/industrial-robots-sales-72-first-half-2019/

[5] https://new.abb.com/products/robotics/industries/packaging-and-palletizing/palletizing

[6] C. Chen, Z. Liu, Y. Zhang, and S. Xie, "Coordinated motion/force control of multiarm robot with unknown sensor nonlinearity and manipulated object's uncertainty," *IEEE Trans. Syst., Man, Cybern., Syst*., vol. 47, no. 7, pp. 1123–1134, Jul. 2017.

[7] Jinjun, Duan, et al. "Symmetrical adaptive variable admittance control for position/force tracking of dual-arm cooperative manipulators with unknown trajectory deviations." *Robotics and Computer-Integrated Manufacturing* 57 (2019): 357-369.

[8] Hichri, B., et al. "Design of cooperative mobile robots for co-manipulation and transportation tasks." *Robotics and computer-integrated manufacturing* 57 (2019): 412-421.

[9] Zhang, Zhirong, Yongduan Song, and Kai Zhao. "Neuroadaptive cooperative control without velocity measurement for multiple humanoid robots under full-state constraints." *IEEE Transactions on Industrial Electronics* 66.4 (2018): 2956-2964.

[10] Fan, Qi, et al. "A vision-based fast base frame calibration method for coordinated mobile manipulators." *Robotics and Computer-Integrated Manufacturing* 68: 102078.

[11] Goertz R C. Fundamentals of General-purpose Remote Manipulators[J]. *Nucleonics*, 1952, Vol: 10, No. 11(11):36-42.

[12] Bloss R. Robotics innovations at the 2009 Assembly Technology Expo[J]. *Industrial Robot An International Journal*, 2010, volume 37(5):427-430.

[13] Ju, Z., Yang, C., & Ma, H. (2014, July). Kinematics modeling and experimental verification of baxter robot. *In Proceedings of the 33rd Chinese Control Conference* (pp. 8518-8523). IEEE.

[14] Cohen, B., Chitta, S., & Likhachev, M. (2012, May). Search-based planning for dual-arm manipulation with upright orientation constraints. *In 2012 IEEE International Conference on Robotics and Automation* (pp. 3784-3790). IEEE.

[15] Pan, Z., & Zhang, H. (2008). Robotic machining from programming to process control: a complete solution by force control. *Industrial Robot: An International Journal*, 35(5), 400-409.

[16] Caccavale, F., Chiacchio, P., Marino, A., & Villani, L. (2008). Six-dof impedance control of dual-arm cooperative manipulators. *IEEE/ASME Transactions On Mechatronics*, 13(5), 576-586.

[17] Quintana, G., & Ciurana, J. (2011). Chatter in machining processes: A review. *International Journal of Machine Tools and Manufacture*, 51(5), 363-376.

[18] Nakai, H., Yamataka, M., Kuga, T., Kuge, S., Tadano, H., Nakanishi, H., ... & Ohtsuka, H. (2006, September). Development of dual-arm robot with multi-fingered hands. *In ROMAN 2006-The 15th IEEE International Symposium on Robot and Human Interactive Communication* (pp. 208-213). IEEE.

[19] R. Tinos, M. H. Terra, and J. Y. Ishihara, "Motion and force control of cooperative robotic manipulators with passive joints," *IEEE Trans. Control Syst. Technol*., vol. 14, no. 4, pp. 725–734, Jul. 2006.

[20] D. Kruse, J. T. Wen, and R. J. Radke, "A sensor-based dual-arm tele-robotic system," *IEEE Trans. Autom. Sci. Eng*., vol. 12, no. 1, pp. 4–18, Jan. 2015.

[21] A. Lopes and F. Almeida, "A force-impedance controlled industrial robot using an active robotic auxiliary device," *Robot. Comput.-Integr. Manuf*., vol. 24, no. 3, pp. 299–309, 2008.

[22] A. Stolt, M. Linderoth, A. Robertsson, and R. Johansson, "Detection of contact force transients in robotic assembly," in *Proc. IEEE Int. Conf. Robot. Autom*., 2015, pp. 962–968.

[23] J. Podobnik and M. Munih, "Haptic interaction stability with respect to grasp force," *IEEE Trans. Syst., Man, Cybern. C, Appl. Rev*., vol. 37, no. 6, pp. 1214–1222, Nov. 2007.

[24] X. Zhu, B. Lin, L. Liu, and Y. Luan, "Power transfer performance and cutting force effects of contactless energy transfer system for rotary ultrasonic grinding," *IEEE Trans. Ind. Electron*., vol. 63, no. 5, pp. 2785–2795, May 2016.

[25] X. Zhang, H. Chen, J. Xu, X. Song, J. Wang, and X. Chen, "A novel sound-based belt condition monitoring method for robotic grinding using optimally pruned extreme learning machine," *J. Mater. Process. Technol*., vol. 260, pp. 9-19, Oct. 2018.

[26] F. Chen, H. Zhao, D. Li, L. Chen, C. Tan, and H. Ding, ‘‘Contact force control and vibration suppression in robotic polishing with a smart end effector,’’ *Robot. Comput.-Integr. Manuf.*, vol. 57, pp. 391–403, Jun. 2019.
[27] J. E. Solanes, L. Gracia, P. Muñoz-Benavent, A. Esparza, J. V. Miro, and J. Tornero, ‘‘Adaptive robust control and admittance control for contactdriven robotic surface conditioning,’’ *Robot. Comput.-Integr. Manuf.*, vol. 54, pp. 115–132, Dec. 2018.
[28] T. Olsson, M. Haage, H. Kihlman, R. Johansson, K. Nilsson, A. Robertsson, M. Björkman, R. Isaksson, G. Ossbahr, T. Brogårdh, “Costefficient drilling using industrial robots with high-bandwidth force feedback,” *Robot. Comput.-Integr. Manuf.*, vol. 26, no. 1, pp. 24–38, Feb. 2010.
[29] X. Xu, W. Chen, D. Zhu D, S. Yan, and H. Ding, ‘‘Hybrid active/passive force control strategy for grinding marks suppression and profile accuracy enhancement in robotic belt grinding of turbine blade,*’’ Robot. Comput.-Integr. Manuf.*, vol. 67, Feb. 2021.
[30] D. Zhu, X. Feng, X. Xu, Z. Yang, W. Li, S. Yan, and H. Ding. H, ‘‘Robotic grinding of complex components: A step towards efficient and intelligent machining–challenges, solutions, and applications,’’ *Robot. Comput.-Integr. Manuf.*, vol. 65, Oct. 2020.
[31] C. Gaz, E. Magrini, and A. De Luca, "A model-based residual approach for human-robot collaboration during manual polishing operations," *Mechatronics*, vol. 55, pp. 234-247, Nov. 2018.
[32] B. Yao, Z. Zhou, L. Wang, W. Xu, Q. Liu, and A. Liu, "Sensorless and adaptive admittance control of industrial robot in physical human-robot interaction", Robot. *Comput.-Integr. Manuf.*, vol. 51, pp. 158-168, Jun. 2018.
[33] A. Cherubini, R. Passama, A. Crosnier, A. Lasnier, and P. Fraisse, “Collaborative manufacturing with physical human-robot interaction,” *Robot. Comput-Integr. Manuf.*, vol. 31, pp. 1–13, Aug. 2016.
[34] H. Lo and S. Xie, “Exoskeleton robots for upper-limb rehabilitation: State of the art and future prospects,” V, vol. 34, no. 3, pp. 261–268, Apr. 2012.
[35] W. Meng, Q. Liu, Z. Zhou, Q. Ai, B. Sheng, and S. Xie, “Recent development of mechanisms and control strategies for robot-assisted lower limb rehabilitation,” *Mechatronics*, vol. 31, pp. 132–145, 2015.
[36] L. Han, W. Xu, B. Li, and P. Kang, “Collision Detection and Coordinated Compliance Control for a Dual-Arm Robot Without Force/Torque Sensing Based on Momentum Observer,” *IEEE/ASME Trans. Mechatronics*, vol. 24, no. 5, pp. 2261–2272, 2019.
[37] https://www.nbcnews.com/mach/innovation/robotic-exoskeletons-are-changing-lives-surprising-ways-n722676
[38] Qu, Jiadi, et al. "Human-like coordination motion learning for a redundant dual-arm robot." *Robotics and Computer-Integrated Manufacturing* 57 (2019): 379-390.
[39] M. H. Korayem, A. M. Shafei, and E. Seidi, ‘‘Symbolic derivation of governing equations for dual-arm mobile fengmanipulators used in fruit-picking and the pruning of tall trees,’’ *Comput. Electron. Agricult.*, vol. 105, pp. 95–102, Jul. 2014.
[40] Bae, Jangho, et al. "Optimal configuration and parametric design of an underwater vehicle manipulator system for a valve task." *Mechanism and Machine Theory* 123 (2018): 76-88.
[41] Talasaz, Ali, Ana Luisa Trejos, and Rajni V. Patel. "The role of direct and visual force feedback in suturing using a 7-DOF dual-arm teleoperated system." *IEEE transactions on haptics* 10.2 (2016): 276-287.
[42] Polverini, Matteo Parigi, Andrea Maria Zanchettin, and Paolo Rocco. "A constraint-based programming approach for robotic assembly skills implementation." *Robotics and Computer-Integrated Manufacturing* 59 (2019): 69-81.
[43] Ren, Yi, et al. "Adaptive hybrid position/force control of dual-arm cooperative manipulators with uncertain dynamics and closed-chain kinematics." *Journal of the Franklin Institute* 354.17 (2017): 7767-7793.
[44] Cao F, Li Y, Zhang G, et al. Novel humanoid dual-arm grinding robot[C]//*2016 12th IEEE/ASME International Conference on Mechatronic and Embedded Systems and Applications (MESA)*. IEEE, 2016: 1-6.
[45] https://www.sohu.com/a/476266844_562020
[46] P. Huang, M. Wang, Z. Meng, F. Zhang, Z. Liu, Attitude takeover control for post-capture of target spacecraft using space robot, *Aerosp. Sci. Technol*. 51 (2016) 171–180, https://doi .org /10 .1016 /j .ast .2016 .02 .006
[47] Li K, Zhang Y, Hu Q. Dynamic modelling and control of a tendon-actuated lightweight space manipulator[J]. *Aerospace Science and Technology*, 2019, 84: 1150-1163.
[48] Chen L, Huang P, Cai J, et al. A non-cooperative target grasping position prediction model for tethered space robot[J]. *Aerospace Science and Technology*, 2016, 58: 571-581.
[49] Shan M, Guo J, Gill E. Review and comparison of active space debris capturing and removal methods[J]. *Progress in Aerospace Sciences*, 2016, 80: 18-32.
[50] T. Chen, H. Wen, H. Hu, D. Jin, Output consensus and collision avoidance of a team of flexible spacecraft for on-orbit autonomous assembly, *Acta Astronaut*. 121 (2016) 271–281, https://doi .org /10 .1016 /j .actaastro .2015 .11.004.
[51] Wang B, Meng Z, Jia C, et al. Anti-tangle control of tethered space robots using linear motion of tether offset[J].

Aerospace Science and Technology, 2019, 89: 163-174.
[52] A. Pisculli, L. Felicetti, P. Gasbarri, G.B. Palmerini, M. Sabatini, A reaction-null/Jacobian transpose control strategy with gravity gradient compensation for on-orbit space manipulators, *Aerosp. Sci. Technol*. 38 (2014) 30–40.
[53] Kindracki J, Tur K, Paszkiewicz P, et al. Experimental research on low-cost cold gas propulsion for a space robot platform[J]. *Aerospace science and technology*, 2017, 62: 148-157.
[54] Jia S, Shan J. Continuous integral sliding mode control for space manipulator with actuator uncertainties[J]. *Aerospace Science and Technology*, 2020, 106: 106192.
[55] Shen D, Tang L, Hu Q, et al. Space manipulator trajectory tracking based on recursive decentralized finite-time control[J]. *Aerospace Science and Technology*, 2020, 102: 105870.
[56] https://www.nasa.gov/mission_pages/station/research/news/b4h-3rd/hh-robotic-arms-reach
[57] Kim U, Lee D H, Kim Y B, et al. A novel six-axis force/torque sensor for robotic applications[J]. *IEEE/ASME Transactions on Mechatronics*, 2016, 22(3): 1381-1391.
[58] L. Xiong, Y. Guo, G. Jiang, X. Zhou, L. Jiang and H. Liu, "Six-Dimensional Force/Torque Sensor Based on Fiber Bragg Gratings With Low Coupling," in *IEEE Transactions on Industrial Electronics*, vol. 68, no. 5, pp. 4079-4089, May 2021, doi: 10.1109/TIE.2020.2982107.
[59] D. Lee, U. Kim, H. Jung and H. R. Choi, "A Capacitive-Type Novel Six-Axis Force/Torque Sensor for Robotic Applications," in *IEEE Sensors Journal*, vol. 16, no. 8, pp. 2290-2299, April15, 2016, doi: 10.1109/JSEN.2015.2504267.
[60] O. Al-Mai, M. Ahmadi and J. Albert, "Design, Development and Calibration of a Lightweight, Compliant Six-Axis Optical Force/Torque Sensor," in *IEEE Sensors Journal*, vol. 18, no. 17, pp. 7005-7014, 1 Sept.1, 2018, doi: 10.1109/JSEN.2018.2856098.
[61] J. W. Guggenheim, L. P. Jentoft, Y. Tenzer and R. D. Howe, "Robust and Inexpensive Six-Axis Force–Torque Sensors Using MEMS Barometers," in *IEEE/ASME Transactions on Mechatronics*, vol. 22, no. 2, pp. 838-844, April 2017, doi: 10.1109/TMECH.2017.2654446.
[62] H. S. Oh, U. Kim, G. Kang, J. K. Seo and H. R. Choi, "Multi-Axial Force/Torque Sensor Calibration Method Based on Deep-Learning," in *IEEE Sensors Journal*, vol. 18, no. 13, pp. 5485-5496, 1 July1, 2018, doi: 10.1109/JSEN.2018.2834727.
[63] M. H. Raibert and J. J. Craig, "Hybrid position/force control of manipulators," *J. Dyn. Syst. Meas. Control*, vol. 103, no. 2, pp. 126-133, 1981.
[64] N. Hogan, "Impedance control: An approach to manipulation-part I: theory; part II: implementation; part III: applications," *Trans. ASME J. Dyn. Syst. Meas. Control*, vol. 107, no. 1, pp. 1-24, 1985.
[65] https://www.tekscan.com/support/faqs/what-materialsconditions-could-damage-flexiforce-sensor
[66] https://www.youtube.com/watch?v=wzAmpIrYRRs
[67] https://www.codyco.eu/images/pdf/2013_Humanoids/Haddadin.pdf
[68] K. Ohnishi, M. Shibata, and T. Murakami, “Motion control for advanced mechatronics,” *IEEE/ASME Trans. Mechatronics*, vol. 1, no. 1, pp. 56–67, Mar. 1996.
[69] T. T. Phuong, K. Ohishi, and Y. Yokokura, ‘‘Fine sensorless force control realization based on dither periodic component elimination Kalman filter and wide band disturbance observer,’’ *IEEE Trans. Ind. Electron*., vol. 67, no. 1, pp. 757–767, Jan. 2020.
[70] L. Chan, F. Naghdy, and D. Stirling, "Extended active observer for force estimation and disturbance rejection of robotic manipulators," *Robot. Auton. Syst.*, vol. 61, no. 12, pp. 1277-1287, 2013.
[71] W.-H. Chen, D. J. Ballance, P. J. Gawthrop, and J. O'Reilly, "A nonlinear disturbance observer for robotic manipulators," *IEEE Trans. Ind. Electron.*, vol. 47, no. 4, pp. 932-938, Aug. 2000.
[72] W.-H. Chen, "Disturbance observer based control for nonlinear systems," *IEEE/ASME Trans. Mechatronics*, vol. 9, no. 4, pp. 706-710, Dec. 2004.
[73] A. Mohammadi, M. Tavakoli, H. Marquez, and F. Hashemzadeh, "Nonlinear disturbance observer design for robotic manipulators," *Control Eng. Pract.*, vol. 21, no. 3, pp. 253-267, 2013.
[74] A. Nikoobin and R. Haghighi, "Lyapunov-based nonlinear disturbance observer for serial n-link robot manipulators," *J. Intell. Robot. Syst.*, vol. 55, no. 2/3, pp. 135-153, Jul. 2009.
[75] H. Zhang, S. Ahmad, and G. Liu, "Torque estimation for robotic joint with harmonic drive transmission based on position measurements," *IEEE Trans. Robot.*, vol. 31, no. 2, pp. 322-330, Apr. 2015.
[76] F. Zhou, Y. Li, and G. Liu, "Robust decentralized force/position fault-tolerant control for constrained reconfigurable manipulators without torque sensing," *Nonlinear Dyn*, vol. 89, no. 3, 2017.
[77] B. Dong, F. Zhou, K. Liu, and Y. Li, "Torque sensorless decentralized neuro-optimal control for modular and reconfigurable robots with uncertain environments," *Neurocomputing*, vol. 282, pp. 60-73, 2018.

[78] J. W. Jeong, P. H. Chang, and K. B. Park, "Sensorless and modeless estimation of external force using time delay estimation: Application to impedance control," *J. Mech. Sci. Technol.*, vol. 25, no. 8, pp. 2051-2059, Sep. 2011.
[79] Dehghan S A M, Danesh M, Sheikholeslam F, et al. Adaptive force–environment estimator for manipulators based on adaptive wavelet neural network[J]. *Applied Soft Computing*, 2015, 28: 527-540.
[80] Jhan Z Y, Lee C H. Adaptive impedance force controller design for robot manipulator including actuator dynamics[J]. *International Journal of Fuzzy Systems*, 2017, 19(6): 1739-1749.
[81] A. D. Luca and R. Mattone, "Sensorless robot collision detection and hybrid force/motion control," *in Proc. IEEE Int. Conf. Robot. Autom.*, 2005, pp. 999-1004.
[82] A. D. Luca, A. Albu-Schäffer, S. Haddadin, and G. Hirzinger, "Collision detection and safe reaction with the DLR-III lightweight manipulator arm," in Proc. IEEE/RSJ Int. Conf. Intell. Robots Syst., 2006, pp. 1623-1630.
[83] A. D. Luca and R. Mattone, "Actuator failure detection and isolation using generalized momenta," *in Proc. IEEE Int. Conf. Robot. Autom.*, vol. 1, Sep. 2003, pp. 634-639.
[84] M. Ragaglia, A. M. Zanchettin, L. Bascetta, and P. Rocco, "Accurate sensorless lead-through programming for lightweight robots in structured environments," *Robot. Comput.-Integr. Manuf,*, vol. 39, pp. 9-21, June 2016.
[85] J. Yuan, Y. Qian, Z. Yuan, L. Gao, and W. Wan, "Position based Impedance Force Controller with Sensorless Force Estimation," *Assembly Autom*., vol. 39, no. 3, pp. 489-496, 2019.
[86] S. H. Yen, P. C. Tang, Y. C. Lin, and C. Y. Lin, "Development of a virtual force sensor for a low-cost collaborative robot and applications to safety control, " *Sensors*, 19(11): 2603, 2019.
[87] Z. Qiu, R. Ozawa, and S. Ma, "A force-sensorless approach to collision detection based on virtual powers," *Adv Robot*, vol. 33, no. 23, pp. 1209–1224, 2019.
[88] Y. Tian, Z. Chen, T. Jia, A. Wang, and L. Li, "Sensorless collision detection and contact force estimation for collaborative robots based on torque observer," *in Proc. IEEE Int. Conf. Robot. Biom*., Dec 2016, pp. 946-951.
[89] Z. Liu, F. Yu, L. Zhang, and T. Li, "Real-time estimation of sensorless planar robot contact information," *J. Robot. Mechatron.*, vol. 29, no. 3, pp.557-565 2017.
[90] M. W. Spong, S. Hutchinson, and M. Vidyasagar, "Robot Modeling and Control," New York, NY, USA: Wiley, 2006.
[91] https://www.universal-robots.com/articles/ur/application-installation/dh-parameters-for-calculations-of-kinematics-and-dynamics/
[92] Gueaieb W, Karray F, Al-Sharhan S. A robust hybrid intelligent position/force control scheme for cooperative manipulators[J]. *IEEE/ASME Transactions on Mechatronics*, 2007, 12(2): 109-125.
[93] Mohajerpoor R, Rezaei M, Talebi A, et al. A robust adaptive hybrid force/position control scheme of two planar manipulators handling an unknown object interacting with an environment[J]. *Proceedings of the Institution of Mechanical Engineers, Part I: Journal of Systems and Control Engineering*, 2012, 226(4): 509-522.
[94] Jafari A, Ryu J H. Independent force and position control for cooperating manipulators handling an unknown object and interacting with an unknown environment[J]. *Journal of the Franklin Institute*, 2016, 353(4): 857-875.
[95] H. Jin and X. Rong, "Contact force estimation for robot manipulator using semi-parametric model and disturbance kalman filter," *IEEE Trans. Ind. Electron.*, vol. 65, no. 4, pp. 3365-3375, Apr. 2018.
[96] A. Wahrburg, J. Bös, K. D. Listmann, F. Dai, B. Matthias, and H. Ding, "Motor-current-based estimation of cartesian contact forces and torques for robotic manipulators and its application to force control," *IEEE Trans. Autom. Sci. Eng.*, pp. 1-8, 2017.
[97] P. Axelsson and F. Gustafsson, "Discrete-time solutions to the continuous-time differential Lyapunov equation with applications to Kalman filtering," *IEEE Trans. Autom. Control*, vol. 60, no. 3, pp. 632-643, Mar. 2015.
[98] C. Van Loan, "Computing integrals involving the matrix exponential," *IEEE Trans. Autom. Control*, vol. 23, no. 3, pp. 395–404, Jun. 1978.
[99] J. Jung, J. Lee, and K. Huh, "Robust contact force estimation for robot manipulators in three-dimensional space," in Proc. *Inst. Mech. Eng. C J. Mech. Eng. Sci.*, vol. 220, no. 9, 2006, pp. 1317-1327.
[100] A. U. Pehlivan, D. P. Losey, and M. K. O'Malley, "Minimal assist-as-needed controller for upper limb robotic rehabilitation," *IEEE Trans. Robot*., vol. 32, no. 1, pp. 113-124, Feb. 2016.
[101] J. T. Gravdahl, "Force estimation in robotic manipulators: Modeling, sim-ulation and experiments," M.S thesis, Dept. Eng. Cybern., NTNU., Norway, 2014.
[102] H. Olsson, K. Åström, C. Canudas de Wit, M. Gäfvert and P. Lischinsky, "Friction models and friction compensation," *Eur. J. Control*, vol. 4, no. 3, pp. 176-195, Dec. 1998.
[103] Huang, Yulong, et al. "A novel adaptive Kalman filter with inaccurate process and measurement noise covariance matrices." *IEEE Transactions on Automatic Control* 63.2 (2017): 594-601.
[104] Zhu, Hao, et al. "An adaptive Kalman filter with inaccurate noise covariances in the presence of outliers." *IEEE Transactions on Automatic Control* (2021).

[105]Wang, Jiaolong, et al. "Suboptimal adaptive Kalman filtering based on the proportional control of prior error covariance." *ISA transactions* 100 (2020): 145-154.
[106]Mercorelli, Paolo. "A switching kalman filter for sensorless control of a hybrid hydraulic piezo actuator using mpc for camless internal combustion engines." *2012 IEEE International Conference on Control Applications. IEEE, 2012*.
[107]Schimmack, Manuel, Benedikt Haus, and Paolo Mercorelli. "An extended Kalman filter as an observer in a control structure for health monitoring of a metal–polymer hybrid soft actuator." *IEEE/ASME Transactions on Mechatronics 23.3 (2018)*: 1477-1487.
[108]Haus, Benedikt, Harald Aschemann, and Paolo Mercorelli. "Tracking control of a piezo-hydraulic actuator using input–output linearization and a cascaded extended kalman filter structure." *Journal of the Franklin Institute* 355.18 (2018): 9298-9320.
[109]Zanni, Lorenzo, et al. "A prediction-error covariance estimator for adaptive Kalman filtering in step-varying processes: Application to power-system state estimation." *IEEE Transactions on Control Systems Technology* 25.5 (2016): 1683-1697.
[110]Zhang, Jinghe, et al. "A two-stage Kalman filter approach for robust and real-time power system state estimation." *IEEE Transactions on Sustainable Energy* 5.2 (2013): 629-636.
[111]Chen, Liang, Paolo Mercorelli, and Steven Liu. "A Kalman estimator for detecting repetitive disturbances." *Proceedings of the 2005, American Control Conference*, 2005.. IEEE, 2005.
[112]Gao, Xiangdong, Deyong You, and Seiji Katayama. "Seam tracking monitoring based on adaptive Kalman filter embedded Elman neural network during high-power fiber laser welding." *IEEE Transactions on Industrial Electronics* 59.11 (2012): 4315-4325.
[113]Zhou, Zebo, et al. "Equality constrained robust measurement fusion for adaptive kalman-filter-based heterogeneous multi-sensor navigation." *IEEE Transactions on Aerospace and Electronic Systems* 49.4 (2013): 2146-2157.
[114]Xu, Geng, et al. "A Computationally Efficient Variational Adaptive Kalman Filter for Transfer Alignment." *IEEE Sensors Journal* 20.22 (2020): 13682-13693.
[115]Bisht, Saurabh S., and Mahendra P. Singh. "An adaptive unscented Kalman filter for tracking sudden stiffness changes." *Mechanical Systems and Signal Processing* 49.1-2 (2014): 181-195.
[116]Liu, Yahui, et al. "An innovative information fusion method with adaptive Kalman filter for integrated INS/GPS navigation of autonomous vehicles." *Mechanical Systems and Signal Processing* 100 (2018): 605-616.
[117]Ghaleb, Fuad A., et al. "Improved vehicle positioning algorithm using enhanced innovation-based adaptive Kalman filter." *Pervasive and Mobile Computing* 40 (2017): 139-155.
[118]Hajiyev, Chingiz, and Halil Ersin Soken. "Robust adaptive Kalman filter for estimation of UAV dynamics in the presence of sensor/actuator faults." *Aerospace Science and Technology* 28.1 (2013): 376-383.
[119]Odry, Ákos, et al. "Kalman filter for mobile-robot attitude estimation: Novel optimized and adaptive solutions." *Mechanical systems and signal processing* 110 (2018): 569-589.
[120]Huang, Yulong, et al. "A new adaptive extended Kalman filter for cooperative localization." *IEEE Transactions on Aerospace and Electronic Systems* 54.1 (2017): 353-368.
[121]Li, Minhan, et al. "Model-free control for continuum robots based on an adaptive Kalman filter." *IEEE/ASME Transactions on Mechatronics* 23.1 (2017): 286-297.
[122]Haus, Benedikt, and Paolo Mercorelli. "Polynomial augmented extended kalman filter to estimate the state of charge of lithium-ion batteries." *IEEE Transactions on Vehicular Technology* 69.2 (2019): 1452-1463.
[123]Cao, F., Docherty, P.D. & Chen, X. Contact force estimation for serial manipulator based on weighted moving average with variable span and standard Kalman filter with automatic tuning. *Int J Adv Manuf Technol* (2021). https://doi.org/10.1007/s00170-021-08036-9
[124]Cao F, Docherty P D, Ni S, et al. Contact force and torque sensing for serial manipulator based on an adaptive Kalman filter with variable time period[J]. *Robotics and Computer-Integrated Manufacturing*, 2021, 72: 102210.
[125]Pandilov Z, Dukovski V. COMPARISON OF THE CHARACTERISTICS BETWEEN SERIAL AND PARALLEL ROBOTS[J]. *Acta Technica Corviniensis-Bulletin of Engineering*, 2014, 7(1).